Quadrupole Mode Perturbation in Storage Rings

Weiming Guo

Submitted to the faculty of the University Graduate School
in partial fulfillment of the requirement
for the degree
Doctor of Philosophy
in the Department of Physics,
Indiana University

August 2003

Accepted by the Graduate Faculty, Indiana univeristy, in partial fulfillment of the requirement for the degree of Doctor of Philosophy.

Shyh-Yuan Lee, Ph.D.

Michael Berger, Ph.D.

Doctoral
Committee
August 28th, 2003

Steven Gottlieb, Ph.D.

William Schaich, Ph.D.

Copyright ©2003 by
Weiming Guo
ALL RIGHTS RESERVED

Acknowledgments

I am grateful to my adviser, Professor Shyh-Yuan Lee. By him I am cultivated to a everyday-hard-worker, which I complained in the first two years, but have been enjoying since then. The right direction and the Hamiltonian theory established by him already facilitate my dissertation work. The meeting with him every week was always of help for the difficulties. The most important thing I learned from him is not knowledge, but the way of doing research and the spirit of striving. I feel lucky to have chosen Indiana University to learn accelerator physics.

I could not have finished my Ph. D study without the company of my colleagues, particularly Chungming Chu, Kaman Fung, Sarah Cousineau, Yunkai Zhang, Shaoheng Wang, Yoich Sato, Xiaobiao Huang and Dazhang Huang. Especially Yunkai Zhang, I shared an office with him for three years. His friendship and encouragement was always a relief of the stress.

I would also like to thank Prof. Alex W. Chao, Dr. King Yuen Ng, Dr. Stephen V. Milton, Dr. Dong O Jeon, Dr. Mei Bai and Dr. Andreas Jansson. Their suggestions and help benefit me a lot.

I owe special thanks to Dan Beeker. He read through my dissertation word by word and corrected the grammar.

At last I would like to thank my wife, Tianli Zhang, for her constant support.

Abstract

Weiming Guo

Quadrupole Mode Perturbation in Storage Rings

Quadrupole mode oscillation(QMO) means the second moments of a system oscillating with time, or, the elliptical torus of the Hamiltonian rotating in phase space. We study the QMO in storage rings. In the transverse direction the QMO can be excited by an rf quadrupole. The strength of the rf quadrupole varies with time, and the oscillation frequency ω_m must be close to twice the transverse betatron oscillation frequency ω_y. The perturbation equation is solved with the Hamiltonian method and we found the beam satisfies Boltzmann distribution. Mathieu instability occurs when $2(\omega_y - C_1\omega_0) < \omega_m < 2(\omega_y + C_1\omega_0)$, where C_1 is the effective strength of the rf quadrupole and ω_0 is the revolution frequency. When a nonlinear detuning term is included, the multi-particle system will bifurcate after passing through the thresholds. The QMO can be detected by a Beam Position Monitor(BPM), and the emittance of the beam can be derived from the signal. The other applications of quadrupole mode perturbation include mismatch correction and spin resonance overcoming.

In the longitudinal direction voltage modulation induces QMO. The Hamiltonian has the same form as the transverse nonlinear QMO Hamiltonian, therefore the beam dynamics and the properties are similar. QMO in the longitudinal direction can be used to compress the bunch in storage rings. Our research results show that the bunch can be compressed by a factor of 2$\sim$3 in proton storage rings. This factor is smaller in electron storage rings due to radiation damping and quantum fluctuation. A more effective method, however, is using a harmonic cavity. Both methods are explored in the second part of this dissertation.

Contents

Acceptance **ii**

Acknowledgments **v**

Abstract **vii**

1 Transverse Motion in Storage Rings **1**

1.1 Hill's Equation 1

1.2 Hamilton Dynamics Applying to accelerator physics 4

1.3 Beam Distribution and Emittance 6

2 Problem to Solve **9**

2.1 Time Dependent Perturbation 9

2.2 Landau Damping 10

2.3 Vlasov Equation 11

2.4 Our Solution 13

3 Quadrupole Mode Perturbation to the Transverse Motion **19**

3.1 Introduction 19

3.2 Resonance Strength of RF Quadrupoles 21

3.3 The Properties of the Hamiltonian 23

3.3.1 Linear Mathieu Instability 23
3.3.2 Nonlinear Mathieu instability 24
3.3.3 The value of the nonlinear Hamiltonian 27
3.4 Hamiltonian Properties in Region 1 29
3.5 Beam-splitting in Region 2 32
3.6 Boltzmann Distribution in beam 37
3.6.1 Beam Distribution of the Ring Hamiltonian 37
3.6.2 Beam Distribution for the Nonlinear Ring Hamiltonian 38
3.6.3 Beam Distribution for the Linear Perturbed Hamiltonian . . . 39
3.6.4 Beam Distribution for the Nonlinear Perturbed Hamiltonian . 41

4 Applications of RF Quadrupole 47
4.1 Emittance Measurement 47
4.1.1 Quadrupole Mode Transfer Function 48
4.1.2 Linear Hamiltonian 52
4.1.3 Nonlinear Hamiltonian 55
4.2 Mismatch Compensation 58
4.2.1 Mismatch compensation for linear systems 59
4.2.2 Mismatch compensation employing nonlinear Mathieu instability island 61
4.3 Overcoming spin resonances 66

5 RF Voltage Modulation 71
5.1 Voltage Modulation and Bunch Compression 71
5.2 The Hamilton Dynamics with Voltage Modulation 73
5.3 Bunch Compression Parameters 76
5.3.1 Bunch Compression in Electron Storage Rings 78

6 Using Double RF Cavities to Compress the Bunch 83

6.1 Introduction 83

6.2 Beam Dynamics with a Second RF System 85

6.3 Bunch Compression in Electron Storage Rings 88

6.4 Condition of Increasing Touschek Lifetime 89

6.5 Example and Particle Simulation 91

7 Conclusion 95

Appendix 98

A Canonical Transformations 99

B Boltzmann Distribution for the Nonlinear Perturbed Hamiltonian 103

C Signals from Beam Position Monitor 111

Bibliography 115

Curriculum Vitae 119

List of Tables

3.1 Parameters of RFQM at KEK 20

4.1 Polarization rate for AGS 69

5.1 Parameters for Next Linear Collider Main Damping Ring [29] 80

6.1 Minimum Relative Strength to Increase Beam Lifetime 90

6.2 Parameters of Two RF Systems for NLCMDR 93

List of Figures

2.1 Left: Tori for Hamiltonian $H = \frac{1}{2}x'^2 + \frac{1}{2}\omega_0^2 x^2$, right: Tori for $\frac{1}{2}x'^2 + \frac{1}{2}\omega_0^2 x^2 + Ax\sin\omega t$ in the resonance rotating frame. 15

3.1 The trace of one single particle in the resonance rotating frame for the linear Hamiltonian. Parameters used are $\delta = 0.0013,\ C_1 = 0.001$. . . 25

3.2 Top left: Stable (solid line) and unstable (short dashed line) fixed points vs the effective resonance proximity parameter $\Delta = \delta/\alpha_{yy}$ for the effective resonance strength parameter $c_1 = C_1/\alpha_{yy} = 0.10$ mm. The plots labeled (1), (2), and (3) correspond to the vertical long-dashed lines marked as (1), (2), and (3) respectively. The Hamiltonian is $H = \Delta I - c_1 I\cos 2\psi + \frac{1}{2}I^2$ with $Y = \sqrt{2I}\cos\psi$ and $P = -\sqrt{2I}\sin\psi$. 26

3.3 The traces of one single particle in 3 frequency regions in the resonance rotating frame. Parameters used are Left: $\delta = 0,\ C_1 = 0.001,\ \alpha_{yy} = -500$, Center: $\delta = -0.002,\ C_1 = 0.001,\ \alpha_{yy} = -500$, and Right: $\delta = 0.0013,\ C_1 = 0.001,\ \alpha_{yy} = -1000$. 28

3.4 The orientation of the torus. The parameters used are Left: $\alpha_{yy} = -200,\ \delta = 0.001, C_1 = 0.0005$, Right: $\alpha_{yy} = 200,\ \delta = -0.001, C_1 = 0.0005$. 29

3.5 The Hamiltonian value as function of J for the left plot of Fig. 3.4. The parameters used are $\alpha_{yy} = -200,\ \delta = 0.001, C_1 = 0.0005$. Left plot is for the vertical direction and right plot is for the horizontal direction. 30

3.6 The Hamiltonian value as function of J in the region 2. The parameters used are $\alpha_{yy} = -200,\ \delta = -0.001, C_1 = 0.002$. Left plot is for the vertical direction and right plot is for the horizontal direction. 31

3.7 Left: the area enclosed by the torus of the Hamiltonian H. Right: the tune of the Hamiltonian. Note the tune at $J = 0$ goes back to $\sqrt{\delta^2 - C_1^2}$. Parameters used are $\alpha_{yy} = -200,\ \delta = -0.002,\ C_1 = 0.001$. 32

3.8 The evolution of bunch distribution as the rf quadrupole parameters are adiabatically changed. The beam splits into two beam-lets, and restore back to one. The normalized phase-space in this plot is defined as $Z = \sqrt{2I}\cos\psi$ and $P_Z = -\sqrt{2I}\sin\psi$. Parameters used in the numerical simulations at the bottom-left plot are $\delta = -0.006256$, $C_1 = 0.01$, and $\alpha_{yy} = -200\ \mathrm{m}^{-1}$. The times corresponding to these Poincareé surfaces of section are marked in Fig. 3.9. 33

3.9 . The dashed and solid lines are the resonance proximity δ parameter and the rf quadrupole strength C_1 as functions of time (in revolution turns). The Poincareé surfaces of section plotted in Figs. 3.8 and 3.10 are marked as diamond symbols. The corresponding turn-numbers are: 0, 1600, 1800, 4000, 4540, and 8000. 34

3.10 The evolution of the 1σ ellipse in the beam manipulation where the beam is moved adiabatically through the Mathieu bifurcation point and back. Parameters used in this simulation at the bottom-left plot are $\delta = -0.006256, C_1 = 0.01$, and $\alpha_{yy} = -200.\ \mathrm{m}^{-1}$ 35

3.11 Left: Emittance increment ratio $\epsilon_{\rm f}/\epsilon_{\rm i}$ after moving the beam to $I_{\rm sfp}$ and back for different α_{yy}. Parameters used in this calculation are $C_1 = 0.004$ with $\alpha_{yy} = -400$ m^{-1} ($\triangle$) -600 m^{-1} ($\diamondsuit$), and -1000. m^{-1} ($\bigcirc$) respectively. Right: Emittance increment ratio after moving the beam to $I_{\rm sfp}$ and back for different parameter C_1. Here, we use $\alpha_{yy} = -1000$ m^{-1}, with $C_1 = 0.006$ ($\triangle$), 0.004 ($\diamondsuit$), and 0.002 ($\bigcirc$) respectively. 36

3.12 The beam distribution of the linear Hamiltonian. The circles are obtained from particle simulation, and the solid line is given by Eq. (3.32). The dotted line of Gaussian distribution is also plotted for comparison. The Gaussian distribution is given by $\rho(J) = \frac{1}{\epsilon}e^{-J/\epsilon}$. Parameters used are $\epsilon = 1 \times 10^{-6} m \cdot rad$, $\delta = 0.0013$, $C_1 = 0.001$. There are 10,000 particles in the simulation and the sampling width is 1.132×10^{-7}. . 40

3.13 The particle distribution along Y or P_y in the same particle simulation as of Fig. 3.12. The circles are obtained from simulation and the solid line is Gaussian distribution given by $\rho(x) = 1/\sqrt{2\pi}\sigma_x e^{-x^2/2\sigma_x^2}$. In the simulation, $\sigma_y^2 = \sqrt{\frac{\delta - C_1}{\delta + C_1}}\epsilon = 3.6 \times 10^{-7}$, $\sigma_p^2 = \sqrt{\frac{\delta + C_1}{\delta - C_1}}\epsilon = 2.8 \times 10^{-6}$, where $\epsilon = 1 \times 10^{-6}$m·rad is the initial emittance. Other parameters are $\delta = 0.0013$, $C_1 = 0.001$ and $N = 10,000, dy = 1.9 \times 10^{-5}, dp = 5.3 \times 10^{-5}$. 41

3.14 The beam distribution against Y or P_y for the nonlinear Hamiltonian in the resonance rotating frame. The circles are obtained from particle simulation, and the solid line is Gaussian distribution given by $\rho(x) = \frac{1}{\sqrt{2\pi}\sigma_x}e^{-x^2/2\sigma_x^2}$. σ_Y or σ_{P_y} is given by Eq. (3.37). In the simulation $\epsilon = 1 \times 10^{-6} m \cdot rad$. 44

3.15 The beam distribution against action J_y for the nonlinear Hamiltonian. The circles are obtained from particle simulation, and the solid line is Gaussian distribution given by $\rho(J) = \frac{1}{\epsilon}e^{-J/\epsilon}$. α_{yy} is written in the plots, the other parameters are $\epsilon = 1\times10^{-6} m\cdot rad$, $\delta = -0.0013$, $C_1 = 0.001$. There are 10,000 particles in the simulation and the widths of the sampling slot are around 6×10^{-8}. 45

3.16 The beam distribution against Y or P_y for the nonlinear Hamiltonian in the resonance rotating frame. The circles are obtained from particle simulation, and the solid line is Gaussian distribution given by $\rho(x) = \frac{1}{\sqrt{2\pi}\sigma_x}e^{-x^2/2\sigma_x^2}$. σ_Y or σ_{P_y} is given by Eq. (3.37). α_{yy} is written in the plots, the other parameters are $\epsilon = 1\times10^{-6} m\cdot rad$, $\delta = -0.0013$, $C_1 = 0.001$. 46

4.1 Top: The second moment $(\langle x^2\rangle - \langle x\rangle^2)$ derived from numerical simulation with parameters $\delta = 0.0025$, $C_1 = 0.0005$, $\nu_y = 8.7$ and $\nu_{\rm m} = 0.395$. Bottom: FFT spectrum of the second moment, where we obtain $b_0 = 3.405 \times 10^{-5}$ m^2 and $b_1 = 6.7 \times 10^{-6}$ m^2. Note that b_0 and b_1 are defined as twice of the Fourier amplitude. 54

4.2 δ^2 versus $\frac{1}{b_1^2}$. $\diamond$: $C_1 = 0.001$, $\circ$: $C_1 = 0.0005$. 55

4.3 Data obtained from a Fourier analysis of numerical simulations. The parameter δ^2 is plotted as a function of $\frac{1}{b_1^2}$. The parameters are $C_1 = 0.0005$ with $\alpha_{yy} = 0, -100, -200, -400, -800$, and -1000 m^{-1} respectively in different symbols from the left-most to the right-most. The straight line is shown to guide the eyes. The data is fitted to obtain the beam emittance. The input rms beam emittance of all simulations is 1 π-mm-mrad, and the betatron amplitude function is 16.7 m. . . . 56

4.4 Comparison between the measured emittance (ϵ_o from numerical simulation data) and the initial input emittance (ϵ_i horizontal axis). A total of 150 sets of numerical simulation data with different machine parameters (C_1 ranging from 0.0005 to 0.005, and α_{xx} ranging from 0 to -1000 m^{-1}) and different initial beam distribution functions (Gaussian (circles) and uniform (diamonds)) are included in this plot for comparison. The spread arises essentially from the nonlinear detuning, and the strength of C_1 parameter. 57

4.5 The mismatched beam ellipse with $I = I_0$ at the injection (0th turn) is captured by an rf quadrupole, and the rf quadrupole strength is adiabatically turned off to restore the matched beam condition at the 3000-th turn. The beam ellipse at the 1000-th turn is also shown for reference. 60

4.6 Left: The invariant tori of the nonlinear Mathieu Hamiltonian with parameters: $\delta = 0.02, C_1 = 0.007464, \alpha_{yy} = -100$ m^{-1}. Right: The ratio $\sqrt{I_{\max}/I_{\min}}$ as a function of the phase-space area of invariant tori inside the middle island. 62

4.7 Left plots: The injected beam is mismatched at the top-left plot. Filamentation is clearly shown in the bottom-left plot at 1000-th turn for the mismatched beam. Right plots: Using nonlinear Mathieu resonance to match the injected beam shown in the top-right plot, we find that the beam emittance is preserved at 3000-th turn even in the presence of nonlinear detuning parameter. The solid lines in this graph show the 2σ admittance-ellipse. 64

4.8 The left plot shows that the $\sqrt{10}\,\sigma$ ellipse will evolve with filamentation. The right plot shows the evolution of the 1σ ellipse with an initial phase intentionally set at $\psi = \psi_0 + \pi/2$. We observe a much larger beam filamentation. Because of the Mathieu island is highly nonlinear, the ellipse is tightly wrapped. 66

4.9 The aspect ratio changes as a function of C_1 at the point $I_{\psi=0} = 5.0 \times 10^{-7}$. $\delta = 0.002$, from the inner to the outer $\alpha_{yy} = -1000, -800, -600, -400, -200$ in sequence. The curve ends when the edge of the bucket is reached. . 67

5.1 The tori of the voltage modulation Hamiltonian and the real trace of particles. The parameters are $\alpha = 0.07528$, $C = 4.41 \times 10^{-5}, b = 0.05$, Δ is different for each graph: up left: $\Delta = -1.005C$, up right: $\Delta = 0$, down: $\Delta = 2.0C$. Traces of two particles are plotted in the down graph. 77

5.2 The aspect ratio changes as Δ goes to $-C$. The parameters used are: $b = 0.1$, $C = 8.82 \times 10^{-5}$, $\nu_s = 0.003529$, $\alpha = 0.07528256$, $\epsilon_0 = 5.0 \times 10^{-5}$. The circles and triangles are the aspect ratios obtained from particle simulation, and the curve is the aspect ratio of the torus with the area of $\pi\epsilon_0$. $\langle r_b \rangle$ saturates at 4.54 for this set of parameters. The triangles are for the simulation with quantum fluctuation and damping, but they are set to zero for those circles. The emittance is preserved provided $\nu_s > \nu_{bif+}$. 79

5.3 In all plots, circles are obtained from particle simulation, solid line is Gaussian distribution with the nominal deviation. Upper left: Particle distribution along $\phi - \phi_s$ direction,$\sigma_\phi = 0.053$ Radian. Upper right: Particle distribution along δ direction, $\sigma_\delta = 0.091\%$. Lower left: Particle distribution along the action J, the Gaussian distribution is given by $\rho(J) = \frac{1}{\epsilon_0} e^{-J/\epsilon_0}$. Lower right: The longitudinal damping process of NLCMDR in the first 10ms after injection. The injection parameters are $\sigma_\phi = 0.15$, $\sigma_\delta = 0.5\%$, the nominal equilibrium parameters are $\sigma_\phi = 0.053$ and $\sigma_\delta = 0.091\%$. 81

5.4 Bunch length and emittance changes while the voltage modulation strength ramps up. The strength increases adiabatically from turn 1,000 to turn 6,000. The solid line has damping and quantum fluctuation on and the dotted line doesn't. Parameters are $b = 0.05, \alpha = 0.07528$, $\Delta = -1.05 \times C$, $C = 4.41 \times 10^{-5}$. Left: Bunch length oscillation. At the minimum bunch length point, $\sigma_\phi = 0.0435, 0.0330$ and $\sigma_\delta = 1.21 \times 10^{-3}, 1.56 \times 10^{-3}$ respectively. Right: The change of emittance. In the presence of damping and quantum fluctuation, the equilibrium emittance is 4.82×10^{-5}. The emittance increases about ten percent when damping and quantum fluctuation are included, but very little when they are set to zero. 82

6.1 The potential change due to the second harmonic cavity. The dotted line is the original potential $V_o(\phi) = \cos\phi - \cos\phi_s + (\phi - \phi_s)\sin\phi_s$. The long dashed line is the potential due to the second rf system, $V_2(\phi) = \frac{r}{m}(\cos(m\phi + \phi_r) - \cos(m\phi_s + \phi_r)) + (\phi - \phi_s)r\sin(m\phi_s + \phi_r)$. The bold line is the combined potential $V_c(\phi) = V_o(\phi) + V_2(\phi)$. The left plot is for bunch lengthening, the parameters are $\phi_s = 2.3288$ Radian, $\phi_r = -5.1436$ Radian, $r = 0.38875$, $m = 2$. The right plot is for bunch compression, and $\phi_s = 2.3288$ Radian, $\phi_r = -m\phi_s - \pi$, $r = 4$, $m = 4$. 84

6.2 Left:Bucket width as a function of r and m. $r = 1, 2, 3, 4, 5$ are calculated but the value of width almost overlap for different r. Right: Bucket height for different r and m. From down to up, $r = 1, 2, 3, 4, 5, 6, 7$ respectively. The lines are plotted to guide the eyes. 87

6.3 Lifetime increasing rate for different r and m. The only parameter $\phi_s = 2.329$ Radian. 90

6.4 The tori for the longitudinal Hamiltonian of NLCMDR. Top: original Hamiltonian. Bottom: with a 4th harmonic rf system. Note the increase of the bucket height. 92

6.5 $r = 4, m = 4$ for the second RF system. Equilibrium parameters are $\sigma_{\delta e} = 0.091\%$, $\sigma_{\phi e} = 0.011$Radian, or $\sigma_{ze} = 0.735$mm, $\epsilon_e = 1.0 \times 10^{-5}$. Right plot details the first 3,000 turns. Note the quadrupole mode oscillation at the beginning due to mismatch. 94

B.1 Solid line is the value of $e^{u^2} erfc(u)$, the circles is the first two term approximation, i.e. calculated by $f(u) = \frac{1}{\sqrt{\pi}u}(1 - \frac{1}{2u^2} + \frac{1 \cdot 3}{(2u^2)^2})$. Therefore u must be greater than 2 to keep accuracy. More terms won't help. . 105

B.2 The comparison of the results of b_1. The parameters used are $C_1 = 1.e-3$, $\alpha_{yy} = 50(\triangle), 100(\bigcirc), 200(\square)$. The solid lines are the result from equation (B.20) and the symbols are from the simulation. Note the third solid line is supposed to fit the squares. 108

C.1 Charge density on the surface of a cylinder. 111

Chapter 1

Transverse Motion in Storage Rings

1.1 Hill's Equation

Particle motion in accelerators must be stable in three dimensions. In the transverse direction this is realized by deploying focusing instruments along the path of the beam. The focusing instruments include electric or magnetic quadrupoles and solenoids etc.

The transverse motion in a storage ring is given by Hill's equation, namely

$$y'' + K_y(s)y = 0, \tag{1.1}$$

where the double prime means the second derivative with respect to s, the path length along the accelerator, y can be either the horizontal (x) or vertical(z) coordinate, $K_x(s) = 1/\rho^2 - B_1(s)/B\rho$, $K_z(s) = B_1(s)/B\rho$, $B_1(s) = \partial B_z/\partial x$, and $B\rho$ is the magnetic rigidity (momentum over charge) of the particle. In order to keep the motion stable, $K_y(s)$ is presumed to be greater than zero, however, $K_y(s)$ with alternative signs can also focus the beam.

The solution of Hill's equation with constant K_y is given by

$$y(s) = \begin{cases} A\cos(\sqrt{K}s + \phi) & K > 0 \\ As + B & K = 0 \\ A\cosh(\sqrt{-K}s + \phi) & K < 0 \end{cases}, \tag{1.2}$$

where A, B, ϕ are integration constants to be determined by the initial conditions. Take a focusing quadrupole as an example, i.e., $K > 0$, and assume the phase space coordinate at the entrance of the quadrupole is (y_0, y_0'), then at the exit

$$\begin{cases} y = y_0 \cos\sqrt{K}l + y_0'/\sqrt{K}\sin\sqrt{K}l \\ y' = -y_0\sqrt{K}\sin\sqrt{K}l + y_0'\cos\sqrt{K}l \end{cases}, \tag{1.3}$$

This is clearer in the matrix presentation

$$\begin{pmatrix} y \\ y' \end{pmatrix} = \begin{pmatrix} \cos\sqrt{K}l & 1/\sqrt{K}\sin\sqrt{K}l \\ -\sqrt{K}\sin\sqrt{K}l & \cos\sqrt{K}l \end{pmatrix} \times \begin{pmatrix} y_0 \\ y_0' \end{pmatrix} \tag{1.4}$$

One can easily verify that the determinant of the matrix is 1. Therefore the area in phase space is preserved during this transformation. In storage rings, Hill's equation has periodic boundary condition, i.e.,

$$K(s + L) = K(s), \tag{1.5}$$

where L is either the length of the ring or the length of the repetitive modules in the ring. According to Floquet's theorem, Hill's equation has solutions of the following form

$$y(s) = A\omega(s)\cos(\psi(s) + \psi_0), \tag{1.6}$$

where $\omega(s + L) = \omega(s)$, $\psi(s + L) = \psi(s) + \psi_0$, ψ_0 is a constant phase advance.

Substituting into Hill's equation, one obtains

$$\begin{cases} 2\omega(s)'\psi(s)' + \omega(s)\psi'' & = & 0 \\ \omega(s)'' + K(s)\omega(s) - \omega(s)(\psi(s)')^2 & = & 0 \end{cases}. \tag{1.7}$$

The first equation of (1.7) can be rewritten as $(\omega^2(s)\psi')' = 0$, or, $\psi'\omega^2(s) = constant$. The solution is not changed if we multiply $\omega(s)$ by a constant. Therefore we can define $\psi' = 1/\omega^2(s)$, and the second equation of (1.7) becomes

$$\omega(s)'' + K(s)\omega(s) - 1/\omega(s)^3 = 0. \tag{1.8}$$

Although we still don't know $\omega(s)$ for any particular $K(s)$, we obtain the important relation between the oscillation amplitude $\omega(s)$ and the phase changing rate ψ', so we know how to describe the motion in storage rings. Defining the Courant-Snyder parameters α, β, γ as

$$\begin{cases} \beta &= \omega^2 \\ \alpha &= -\beta'/2 \\ \gamma &= \frac{1+\alpha^2}{\beta} \end{cases}, \tag{1.9}$$

one gets the general solution of Hill's equation

$$y(s) = A\sqrt{\beta_y(s)}\cos(\psi_y(s) + \xi_y), \tag{1.10}$$

where $\psi_y(s) = \int_0^s \frac{ds}{\beta_y(s)}$, and β satisfies

$$\frac{1}{2}\beta'' + K\beta - \frac{1}{\beta}[1 + (\frac{\beta'}{2})^2] = 0, \text{or } \alpha' = K\beta - \frac{1}{\beta}(1+\alpha^2). \tag{1.11}$$

Again if we assume the initial condition at position s_1 is (y_1, y_1'), then at position s_2

$$\begin{pmatrix} y_2 \\ y_2' \end{pmatrix} = \begin{pmatrix} \sqrt{\frac{\beta_2}{\beta_1}}(\cos\psi + \alpha_1\sin\psi) & \sqrt{\beta_1\beta_2}\sin\psi \\ -\frac{1+\alpha_1\alpha_2}{\sqrt{\beta_1\beta_2}}\sin\psi + \frac{\alpha_1-\alpha_2}{\sqrt{\beta_1\beta_2}}\cos\psi & \sqrt{\frac{\beta_1}{\beta_2}}(\cos\psi - \alpha_2\sin\psi) \end{pmatrix} \begin{pmatrix} y_1 \\ y_1' \end{pmatrix}, \tag{1.12}$$

where $\psi = \psi(s_2) - \psi(s_1)$ is the phase advance. According to Floquet's theorem, after a periodic length L $\omega(s+L) = \omega(s)$, $\alpha_1, \beta_1, \gamma_1$ equals $\alpha_2, \beta_2, \gamma_2$ respectively. If we denote these functions by α, β, γ and denote Φ as the phase advance, the transfer matrix can be written as

$$M(s_1 + L|s_1) = \begin{pmatrix} \cos\Phi + \alpha\sin\Phi & \beta\sin\Phi \\ -\gamma\sin\Phi & \cos\Phi - \alpha\sin\Phi \end{pmatrix}. \tag{1.13}$$

Notice that the transfer matrix in Eq. (1.12) can be written as

$$M(s_2|s_1) = \begin{pmatrix} \sqrt{\beta_2} & 0 \\ -\frac{\alpha_2}{\sqrt{\beta_2}} & \frac{1}{\sqrt{\beta_2}} \end{pmatrix} \begin{pmatrix} \cos\psi & \sin\psi \\ -\sin\psi & \cos\psi \end{pmatrix} \begin{pmatrix} \frac{1}{\sqrt{\beta_1}} & 0 \\ \frac{\alpha_1}{\sqrt{\beta_1}} & \sqrt{\beta_1} \end{pmatrix}, \tag{1.14}$$

which suggests if we transfer the phase space coordinates (y, y') into some normalized phase space coordinates, then the particle motion in phase space is just coordinate rotation. And this is what we are going to do in the next section. The basics of canonical transformation can be found in Appendix A.

1.2 Hamilton Dynamics Applying to accelerator physics

The Hill's equation can be derived from the following Hamiltonian

$$H = \frac{1}{2}y'^2 + \frac{1}{2}K(s)y^2 \tag{1.15}$$

From Eq. (1.10) one obtains

$$y' = \frac{\beta'}{2\beta}A\sqrt{\beta}\cos\psi - \frac{1}{\beta}A\sqrt{\beta}\sin\psi = -\frac{y}{\beta}(\tan\psi - \frac{\beta'}{2}). \tag{1.16}$$

This suggests a generating function

$$F_1(y,\psi) = \int_0^y y'dy = -\frac{y^2}{2\beta}(\tan\psi - \frac{\beta'}{2}), \tag{1.17}$$

hence the conjugate action variable is

$$J = -\frac{\partial F_1}{\partial\psi} = \frac{y^2}{2\beta}\sec^2\psi = \frac{1}{2\beta}[y^2 + (\beta y' + \alpha y)^2], \tag{1.18}$$

and the new Hamiltonian is given by

$$\tilde{H} = H + \frac{\partial F_1}{\partial s}. \tag{1.19}$$

However,

$$\frac{\partial F_1}{\partial s} = \frac{y^2}{2\beta^2}\beta'(\tan\psi - \beta'/2) + \frac{\beta''}{4\beta}y^2, \tag{1.20}$$

and notice that

$$\frac{1}{2}y'^2 = \frac{y^2}{2\beta^2}(\sec^2\psi - 1 - \beta'\tan\psi + \frac{\beta'^2}{4}). \tag{1.21}$$

Therefore

$$H + \frac{\partial F_1}{\partial s} = \frac{y^2}{2\beta^2}(K\beta^2 + \frac{1}{2}\beta\beta'' + \sec^2\psi - 1 - \frac{\beta'^2}{4}). \tag{1.22}$$

From Eq. (1.11), we know

$$K\beta^2 + \frac{1}{2}\beta\beta'' - \frac{\beta'^2}{4} - 1 = 0. \tag{1.23}$$

Hence finally one obtains

$$\tilde{H} = \frac{y^2}{2\beta^2}\sec^2\psi = \frac{J}{\beta}. \tag{1.24}$$

We have now transformed the Hamiltonian from (y, y') phase space to action-angle phase space. The Hamilton Equations are

$$\begin{cases} \psi' &= \frac{\partial \tilde{H}}{\partial J} &= \frac{1}{\beta(s)} \\ J' &= -\frac{\partial \tilde{H}}{\partial \psi} &= 0 \end{cases}. \tag{1.25}$$

Therefore J is an invariant. Note $\tilde{H}$ still depends on s because $\beta(s)$ is not constant. Sometimes it is useful to have a constant Hamiltonian. With the generating function

$$F_2(\psi, I) = (\psi - \int_0^s \frac{ds}{\beta} + \nu_y\theta)I, \tag{1.26}$$

where $\nu_y = \frac{1}{2\pi}\int_s^{s+C}\frac{ds}{\beta_y(s)}$ is the tune of the storage ring, and C is the circumference of the ring. The new conjugate coordinates (Φ, I) are

$$\Phi = \psi - \int_0^s \frac{ds}{\beta} + \nu_y\theta, \qquad I = J, \tag{1.27}$$

and the new Hamiltonian becomes $\hat{H} = \nu_y I/R$. Changing the time coordinate from s to θ, the new Hamiltonian is re-scaled and becomes

$$\hat{H} = \nu_y I. \tag{1.28}$$

From Eq. (1.18), we find

$$y = \sqrt{2\beta J}\cos\psi, \qquad y' = -\sqrt{\frac{2J}{\beta}}(\sin\psi + \alpha\cos\psi), \tag{1.29}$$

where $\alpha = -\beta'/2$. Sometimes it is more convenient to define the normalized conjugate phase-space coordinate (Y, P_y) as

$$Y = \sqrt{2\beta J}\cos\psi, \qquad P_y = -\sqrt{2\beta J}\sin\psi, \tag{1.30}$$

A particle trajectory in (Y, P_y) phase space is a circle with radius $\sqrt{2\beta J}$. Now that β is a constant at one location, J has the meaning of the square of the radius divided by 2β. Expressing J in terms of y and y', one gets

$$C(y, y') = \frac{1}{\beta}[y^2 + (\alpha y + \beta y')^2] = \gamma y^2 + 2\alpha y y' + \beta y'^2 = 2J. \tag{1.31}$$

This indicates the trajectory of particle motion with initial condition (y_0, y_0') follows an ellipse described by $C(y, y') = 2J$. And the phase space enclosed by the ellipse is equal to $2\pi J$, which is a constant independent of location s. From this we are going to derive the concept of emittance in the next section.

1.3 Beam Distribution and Emittance

Usually there are a large number of particles in one bunch. For example, A 1.6 mA bunch with the revolution frequency of $1MHz$ has 10^{10} unit charge particles. The particles are distributed in phase space. The quality of the beam depends on particle distribution. On the other hand the particle distribution also affects the collective

motion of the beam. As we stated in the first section, the phase space area enclosed by the trace of one particle is preserved in case of linear motion. We use emittance to describe the quality of the beam. The physical meaning of emittance is the average area of all particles in phase space. For example, the emittance of a bunch with a normalized distribution function $\rho(J,\psi)$ is given by

$$\epsilon = \int_0^{2\pi} d\psi \int_0^{\infty} dJ J \rho(J,\psi). \tag{1.32}$$

If the distribution is Gaussian, namely

$$\rho(J,\psi) = \frac{1}{2\pi\epsilon_0} e^{-J/\epsilon_0}, \tag{1.33}$$

then the area enclosed by one particle is $2\pi J$, and the integral in Eq. (1.32) is ϵ_0. Therefore the emittance equals 2π times the average of the action. Statistically there is another way to calculate the emittance, i.e., by calculating the moments of the beam. In (y, y') phase space with a normalized distribution function $\rho(y, y')$, the first and second moments of the beam are given by

$$\begin{aligned}
\langle y \rangle &= \textstyle\int_{-\infty}^{\infty} dy \int_{-\infty}^{\infty} dy' y \rho(y,y'), \\
\langle y' \rangle &= \textstyle\int_{-\infty}^{\infty} dy \int_{-\infty}^{\infty} dy' y' \rho(y,y'), \\
\sigma_y^2 &= \textstyle\int_{-\infty}^{\infty} dy \int_{-\infty}^{\infty} dy' (y - \langle y \rangle)^2, \\
\sigma_{y'}^2 &= \textstyle\int_{-\infty}^{\infty} dy \int_{-\infty}^{\infty} dy' (y' - \langle y' \rangle)^2, \\
\sigma_{yy'} &= \textstyle\int_{-\infty}^{\infty} dy \int_{-\infty}^{\infty} dy' (y - \langle y \rangle)(y' - \langle y' \rangle) \quad = \quad r\sigma_y\sigma_{y'},
\end{aligned} \tag{1.34}$$

where σ_y is the rms beam width, $\sigma_{y'}$ is the rms beam height in phase space, $\sigma_{yy'}$ is the correlation between them and r the correlation coefficient. The rms emittance is then calculated by

$$\epsilon_{rms} = \pi\sqrt{\sigma_y^2\sigma_{y'}^2 - \sigma_{yy'}^2} = \pi\sigma_y\sigma_{y'}\sqrt{1-r^2}. \tag{1.35}$$

Note the emittance calculated by Eq. (1.35) is only equivalent to that by Eq. (1.32) in case of linear motion.

Chapter 2

Problem to Solve

2.1 Time Dependent Perturbation

In chapter one we showed the transverse motion of particles in storage rings is governed by the Hill's equation. The solution is a quasi-harmonic oscillator and can be described by the Courant-Snyder parameters. However, in some cases, when we model wake field, space charge effect or small disturbances caused by noise, we have to solve the perturbed equation

$$y'' + K_y(s)y = A(y)\sin\omega t. \tag{2.1}$$

The particular forms for different situations might be different, but they all share the same feature, i.e., the quasi-harmonic equation is perturbed by a time-dependent term $A(y)\sin\omega t$. If $A(y)$ is a constant, it is called dipole mode perturbation. For example, the betatron motion under the excitation of an rf dipole is described by such an equation with $A = -\frac{B_m(s)}{B\rho}$, where $B_m(s)$ is the amplitude of the rf dipole field, and $B\rho$ is the magnetic rigidity of the particle. This dipole mode perturbation is well understood and has been successfully applied to overcoming spin resonance, which, actually stimulated the original idea of this dissertation [2]. If $A(y) = cy$, where c is

a constant, then we call the term at RHS quadrupole mode perturbation. Note this perturbation term is both a function of oscillation amplitude y and time t, therefore it can not be generated by an ordinary quadrupole. Since the strength oscillates with time, it must be a time-dependent quadrupole. As is shown later, the effect of this term is negligible unless ω/ω_0 is close to twice of the tune ν_y, where ω_0 is the angular revolution frequency. If K_y is a constant, then the quadrupole mode perturbation equation is just the Mathieu Equation. We are going to find out the solution to this equation with $K_y(s)$ as a function of s to understand the physics of quadrupole mode oscillation. We then apply the solution to several aspects of accelerator physics.

Note we are not dealing with a single particle, therefore the perturbation must be understood in an ensemble picture and the particle distribution will be involved. We are concerned more with the final equilibrium state than the transient states, hence Landau Damping is also included in our scope.

Instead of solving the differential equation directly, the classical Hamiltonian method will be used throughout this thesis. We use the Hamiltonian method to solve for the asymptotic solution. Before describing our method, I would like to discuss the basic concepts as well as how this kind of problem is currently handled.

2.2 Landau Damping

Let's take as an example the simplest form of Eq. (2.1)

$$x'' + \omega_0^2 x = A\sin(\omega t + \phi_0). \tag{2.2}$$

It has analytic solution

$$\begin{aligned} x &= x_0 \cos\omega_0 t + \frac{x_0'}{\omega_0}\sin\omega_0 t \\ &+ \frac{A}{\omega_0^2 - \omega^2}(\sin(\omega t + \phi_0) - \sin\phi_0 \cos\omega_0 t - \frac{\omega}{\omega_0}\cos\phi_0 \sin\omega_0 t), \end{aligned} \tag{2.3}$$

with x_0 and x_0' as initial values. For simplicity, let $\phi_0 = \pi/2$. For a large number of particles with a normalized distribution $\rho(\omega_0)$, the displacement of the centroid is given by

$$\langle x(t)\rangle = \int_{-\infty}^{+\infty} d\omega_0 \frac{A\rho(\omega_0)}{\omega_0^2 - \omega^2}[\cos\omega t - \cos\omega_0 t]. \tag{2.4}$$

In order to drive the system, the driving frequency ω must be close to ω_0. Expanding Eq. (2.4) around ω_0 and keeping the first order term, one obtains

$$\begin{aligned}\langle x(t)\rangle = \frac{A}{2\omega_0}\Big[\cos\omega t \int_{-\infty}^{+\infty} d\omega_0 \rho(\omega_0)\frac{1-\cos(\omega_0-\omega)t}{\omega_0-\omega} \\ + \sin\omega t \int_{-\infty}^{+\infty} d\omega_0 \rho(\omega_0)\frac{\sin(\omega_0-\omega)t}{\omega_0-\omega}\Big].\end{aligned} \tag{2.5}$$

With the well-known mathematics trick,

$$\lim_{t\to\infty}\frac{1-\cos(\omega_0-\omega)t}{\omega_0-\omega} = \mathcal{P}\frac{1}{\omega_0-\omega} \quad \text{and} \quad \lim_{t\to\infty}\frac{\sin(\omega_0-\omega)t}{\omega_0-\omega} = \pi\delta(\omega_0-\omega), \tag{2.6}$$

where $\mathcal{P}$ stands for the principal value, one gets

$$\langle x(t)\rangle = \frac{A}{2\omega_0}\Big[\cos\omega t\ \mathcal{P}\int_{-\infty}^{+\infty} d\omega_0 \frac{\rho(\omega_0)}{\omega_0-\omega} + \pi\rho(\omega)\sin\omega t\Big]. \tag{2.7}$$

Therefore the displacement is distribution related. Only those particles with the frequency $\omega_0 \sim \omega$ can get energy from the driving force. Particles with ω_0 far from ω will gain energy first, then give it back to the system. This is the basic physical picture of Landau Damping. As we shall see later, Eq. (2.7) is not so accurate.

2.3 Vlasov Equation

Vlasov Equation can be derived from the continuity equation in phase space

$$\frac{\partial\rho}{\partial t} + \vec{\nabla}\cdot(\rho\vec{V}) = 0, \tag{2.8}$$

where $\vec{\nabla}$ is the divergence in phase space and $\vec{V}$ is the velocity vector in phase space. In one dimensional phase space $\vec{\nabla} = (\frac{\partial}{\partial x}, \frac{\partial}{\partial \dot{x}})$ and $\vec{V} = (\frac{dx}{dt}, \frac{d\dot{x}}{dt})$. One can easily verify $\vec{\nabla} \cdot \vec{V} = 0$ with Hamilton's Equations, therefore in one dimensional phase space Eq. (2.8) becomes

$$\frac{\partial \rho}{\partial t} + \frac{dx}{dt}\frac{\partial \rho}{\partial x} + \frac{d\dot{x}}{dt}\frac{\partial \rho}{\partial \dot{x}} = 0. \tag{2.9}$$

Combining with the Hamilton's Equations, one obtains

$$\frac{\partial \rho}{\partial t} + \frac{\partial H}{\partial \dot{x}}\frac{\partial \rho}{\partial x} - \frac{\partial H}{\partial x}\frac{\partial \rho}{\partial \dot{x}} = 0. \tag{2.10}$$

It has a similar form in action-angle phase space

$$\frac{\partial \rho}{\partial t} + \frac{\partial H}{\partial J}\frac{\partial \rho}{\partial \Phi} - \frac{\partial H}{\partial \Phi}\frac{\partial \rho}{\partial J} = 0. \tag{2.11}$$

Eq. (2.2) can be derived from the following action-angle phase space Hamiltonian assuming perturbation force $Ae^{-i\omega t}$ [3]

$$H = \omega_0 J + A\sqrt{\frac{2J}{\omega_0}}\cos\Phi e^{-i\omega t}, \tag{2.12}$$

therefore

$$\begin{cases} \dot{J} &= -A\sqrt{\frac{2J}{\omega_0}}\sin\Phi e^{-i\omega t} \\ \dot{\Phi} &= \omega_0 + \frac{A}{2J\omega_0}\cos\Phi e^{-i\omega t} \end{cases}.$$

Let $\rho(J,\Phi,t) = \rho_0(J) + \rho_1(J,\Phi,t) = \rho_0(J) + g(J)e^{i(\Phi-\omega t)}$, substituting into Eq. (2.11) and keeping only the first order term(assuming A and ρ_1 are small), one gets

$$\frac{\partial \rho_1}{\partial t} + \omega_0\frac{\partial \rho_1}{\partial \Phi} - A\sqrt{\frac{2J}{\omega_0}}\sin\Phi e^{-i\omega t}\frac{\partial \rho_0}{\partial J} = 0, \tag{2.13}$$

or

$$-i\omega g(J) + i\omega_0 g(J) - A\sqrt{\frac{2J}{\omega_0}}\frac{1-e^{-2i\Phi}}{2i}\frac{\partial \rho_0}{\partial J} = 0. \tag{2.14}$$

Averaging over Φ yields

$$g(J) = \frac{1}{\omega - \omega_0}\frac{A}{2}\sqrt{\frac{2J}{\omega_0}}\frac{\partial \rho_0}{\partial J}. \tag{2.15}$$

Therefore the distribution under perturbation becomes

$$\rho(J, \Phi, t) = \rho_0(J) + \frac{1}{\omega - \omega_0}\frac{A}{2}\sqrt{\frac{2J}{\omega_0}}\frac{\partial \rho_0}{\partial J}e^{i(\Phi - \omega t)}, \tag{2.16}$$

namely, the distribution function has a small fractional time dependent term. However, in most cases, especially in dipole mode perturbation, ρ_1 (or $g(J)$) is not small. Therefore, this method has the limitation that it works only in some particular cases. In the next section the Hamiltonian method will be discussed and our approach to the particle distribution will also be introduced.

2.4 Our Solution

Equation (2.2) can be derived from the following Hamiltonian

$$H = \frac{1}{2}x'^2 + \frac{1}{2}\omega_0^2 x^2 - Ax\sin(\omega t + \phi_0) \tag{2.17}$$

With the generating function $F_1(x, \Psi) = -\frac{1}{2}\omega_0 x^2 \tan\Psi$, i.e., letting

$$\begin{cases} x &= \sqrt{\frac{2J}{\omega_0}}\cos\Psi \\ x' &= -\sqrt{2J\omega_0}\sin\Psi \end{cases},$$

one obtains the new Hamiltonian in action angle phase space

$$\begin{aligned} \hat{H} &= \omega_0 J - A\sqrt{\frac{2J}{\omega_0}}\cos\Psi\sin(\omega t + \phi_0) \\ &= \omega_0 J - \frac{A}{2}\sqrt{\frac{2J}{\omega_0}}[\sin(\Psi + \omega t + \phi_0) - \sin(\Psi - \omega t - \phi_0)]. \end{aligned}$$

When $\omega \sim \omega_0$, ignoring the fast oscillation term, one gets

$$\hat{H} \approx \omega_0 J + \frac{A}{2}\sqrt{\frac{2J}{\omega_0}}\sin(\Psi - \omega t - \phi_0). \tag{2.18}$$

Note the fast oscillation term doesn't affect the final equilibrium distribution. Furthermore, the system can't get energy from this term because it is incoherent. Essentially this is due to Landau Damping.

With the generating function

$$F_2(\Psi, I) = (\Psi - \omega t - \phi_0)I, \tag{2.19}$$

the Hamiltonian is again transformed to the resonance rotating frame as

$$\bar{H} = \delta I + \frac{A}{2}\sqrt{\frac{2I}{\omega_0}}\sin\Phi, \tag{2.20}$$

where $\delta = \omega_0 - \omega$. The fixed points are given by

$$\dot{I} = -\frac{\partial \bar{H}}{\partial \Phi} = 0, \quad \text{and} \quad \dot{\Phi} = \frac{\partial \bar{H}}{\partial I} = 0, \tag{2.21}$$

or $\Phi_{FP} = \frac{\pi}{2}$ and $I_{FP} = \frac{A^2}{8\delta^2\omega_0}$, which is the only fixed point and is stable.

Note the Hamiltonian in Eq. (2.20) is time-independent. It describes a harmonic oscillator, which is obvious if we let

$$\begin{cases} Y &= \sqrt{\frac{2I}{\delta}}\cos\Phi \\ P &= -\sqrt{2I\delta}\sin\Phi \end{cases},$$

note the above relation can also be derived from the generating function

$$F_1(Y, \Phi) = -\frac{1}{2}\delta Y^2 \tan\Phi. \tag{2.22}$$

The Hamiltonian becomes

$$\begin{aligned} \tilde{H} &= \frac{1}{2}P^2 + \frac{1}{2}\delta^2 Y^2 - \frac{A}{2}\sqrt{\frac{1}{\delta\omega_0}}P \\ &= \frac{1}{2}(P - \frac{A}{2}\sqrt{\frac{1}{\delta\omega_0}})^2 - \frac{A^2}{8\delta\omega_0} + \frac{1}{2}\delta^2 Y^2. \end{aligned}$$

Again using the generating function $F_3(P, \Phi) = \frac{1}{2\delta}(P - \frac{A}{2}\sqrt{\frac{1}{\delta\omega_0}})^2 \cot\Phi$, one gets the familiar form of the Hamiltonian

$$\check{H} = \delta\bar{I}. \tag{2.23}$$

Note the constant term has been thrown out. Although it has the same form as the unperturbed Hamiltonian, however, this Hamiltonian is in the transferred resonance rotating frame, therefore the physics is much different.

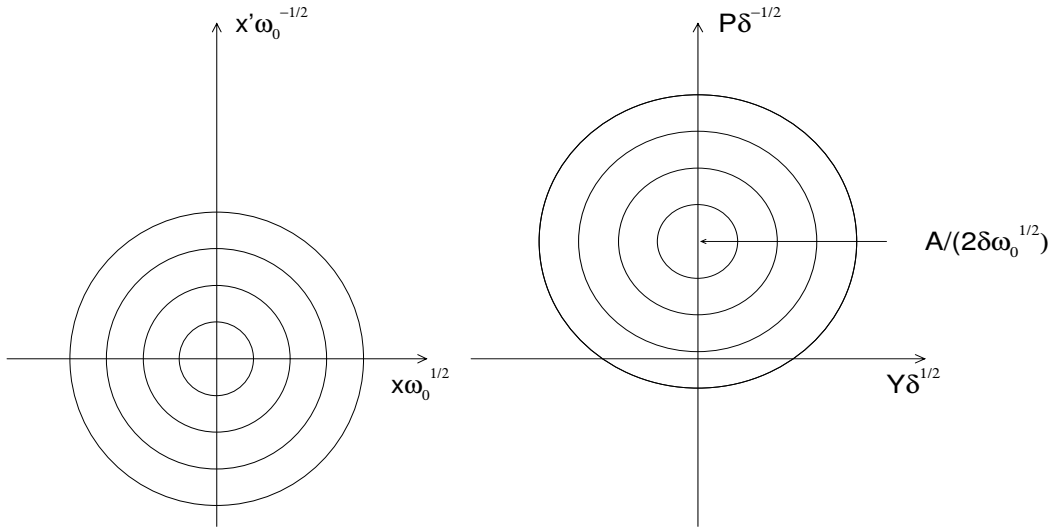

Figure 2.1: Left: Tori for Hamiltonian $H = \frac{1}{2}x'^2 + \frac{1}{2}\omega_0^2 x^2$, right: Tori for $\frac{1}{2}x'^2 + \frac{1}{2}\omega_0^2 x^2 + Ax\sin\omega t$ in the resonance rotating frame.

Fig. 2.1 shows the tori for the original and the perturbed Hamiltonian. The effect of the perturbation is giving the center of mass a displacement in phase space, in the mean time rotating the centroid of the system at angular speed of ω, the driving frequency. This is the physical picture of dipole mode oscillation.

If we assume the system has very narrow frequency spread, i.e., $\rho(\omega) = \delta(\omega - \omega_0)$, then the displacement of the center of mass is

$$\langle x(t)\rangle = \frac{A}{2\delta\omega_0}\sin(\omega t + \phi_0). \tag{2.24}$$

One can compare Eq. (2.7) with Eq. (2.24). Remember both results have included Landau Damping.

Note in Fig. 2.1 all the tori are circles. Therefore, if the phase space is preserved during the turning-on of the driving force, the beam distribution around the centroid should be the same. This is true only for the dipole mode oscillation. For the other modes, we have to go back to the Vlasov Equation.

In the resonance rotating frame, the Hamiltonian is time-independent, therefore we expect the equilibrium particle distribution to be independent of time. The Vlasov Equation becomes

$$\frac{\partial H}{\partial P}\frac{\partial \rho}{\partial Y} - \frac{\partial H}{\partial Y}\frac{\partial \rho}{\partial P} = 0, \tag{2.25}$$

where (Y, P) are phase space coordinates as defined in Eq. (2.22). Eq. (2.25) means the distribution function doesn't change along the torus of the Hamiltonian, or, the distribution is a function of H, the Hamiltonian. The particular form of the solution is determined by the initial condition. Note Boltzmann distribution $\rho = Ne^{-\frac{H}{k_B T}}$ automatically satisfies Eq. 2.25, where N is the normalization factor, H is the Hamiltonian, k_B is Boltzmann constant and T is the temperature. For linear cases, $k_B T = \Omega\epsilon_0$, where Ω is the tune of the Hamiltonian and ϵ_0 is the emittance of the initial system. In order for the system to satisfy the Boltzmann distribution, the initial distribution before the turning-on of the driving force must be Gaussian. Actually Gaussian distribution is another form of Boltzmann distribution in our linear system. If we substitute the initial Hamiltonian $H = \nu J$ into Boltzmann distribution, we get $\rho(J) = \frac{1}{2\pi\epsilon_0}e^{J/\epsilon_0}$, which is the Gaussian distribution. Fortunately for many systems the initial states are in Gaussian distribution, therefore Boltzmann distribution in the resonance rotating frame has general significance.

Back to our problem. If the initial distribution is Gaussian, then the distribution function for the Hamiltonian (2.23) is

$$\rho(\bar{I}) = \frac{1}{2\pi\epsilon_0}e^{-\frac{\delta\bar{I}}{\delta\epsilon_0}} = \frac{1}{2\pi\epsilon_0}e^{-\frac{\bar{I}}{\epsilon_0}}, \tag{2.26}$$

which is the same as the initial distribution except this is in the transferred resonance rotating frame. The distribution in the lab frame can be found by rotation and transformation. Note in the lab frame the distribution is a function of time due to the rotation. Therefore all the problems are solved and this is our method. In this dissertation we are going to solve Eq. (2.1) with quadrupole mode perturbation, and discuss the applications.

Chapter 3

Quadrupole Mode Perturbation to the Transverse Motion

3.1 Introduction

One similar structure to rf quadrupole is the RFQ (Radio Frequency Quadrupole) accelerator. The idea was put forward by I.M.Kapchinskij and V.A.Teplyahov [4] in 1970. They created a novel linac structure which can both accelerate and focus low energy beam with an alternating electromagnetic field. However, what we will study is a quadrupole magnet with radio frequency power supply. It is used for focusing or defocusing of high energy beam in storage rings. If the quadrupole strength for such a quadrupole is $K_{rf} = B_1/B\rho$, where $B_1 = \partial B_Z/\partial x$, and $B\rho$ is the magnetic rigidity of the particle, then the equation of motion in the rf quadrupole is

$$y'' + K_{rf} \cos \omega_{rf} t \; y = 0, \tag{3.1}$$

where ω_{rf} is the working frequency of the rf quadrupole and the double prime means the second derivative with respect to the path length $s = v_0 t$. Therefore the focusing

or defocusing force varies periodically with time. In storage rings, this means the phase advance contributed by the rf quadrupole changes periodically.

At first physicists realized that the tune spread for individual bunches brought by rf quadrupole could be used to suppress the coupled bunch instability [5]. In 1991 an 'RFQM' was built and installed in the 2.5 GeV positron storage ring, the Photon Factory at KEK, Japan [6]. In order to have the idea of their implementation, the parameters of this RFQ Magnet is listed in Table 3.1. It has a one turn coil and

Table 3.1: Parameters of RFQM at KEK

Maximum field gradient(peak value)	0.0173 T/m
Maximum peak current	43 A
Excitation frequency	1.6029MHZ
Bore diameter	120 mm
Core Length	0.34 m
Effective magnetic length	0.38 m
Self inductance	2.1 μ H
Maximum output power of RF amplifier	2 kW
Maximum horizontal tune shift (peak value)	1.23×10^{-3}
Maximum vertical tune shift (peak value)	6.8×10^{-4}

a ferrite yoke. The RFQM works at revolution frequency and the measured tune change for different bunch is a sinusoidal curve along the longitudinal path, which is as expected. Then they tuned one cavity to generate a higher-order-mode (HOM) frequency $f = (n - \nu_x) f_0$, where n is an integer, ν_x is the horizontal tune and f_0 is the revolution frequency. When this HOM existed, the threshold current dropped from 28mA to 9mA, however, if the RFQM was turned on and the tune spread of 2.5×10^{-4}

was introduced into different bunches then the threshold current stayed almost the same! The experimental results indicated that the RFQM was effective in suppressing the instability caused by the HOM oscillation. Unfortunately the RFQM almost had no effect on the vertical intensity related instability in their positron ring, which was their initial motive. Until recently there was still interesting discussion about increasing the transverse mode coupling instability threshold by an RF quadrupole [7].

Another RF quadrupole was later built at HIMAC, Japan [8]. In the beginning they wanted to use it for slow extraction. Similar to the third harmonic resonance slow extraction, the rf quadrupole was intended to be a second harmonic driving device. The particles were expected to move away from the center slowly under the driving force of the rf quadrupole. In 2002 it was reported that the RF quadrupole was used in their space-charge experiment [9].

During all those explorations there is an unsolved mathematical difficulty, i.e., the Mathieu instability. As we discussed in Chapter two, one way to solve this problem is to use the Hamiltonian method. In this chapter we will give an analytic solution to this problem, discuss the properties of the final Hamiltonian and verify it with particle simulation.

3.2 Resonance Strength of RF Quadrupoles

The transverse equation of motion in storage rings in the presence of rf quadrupoles is given by

$$y'' + K(s)y = \frac{B_1(s)}{2B\rho} y \cos(\omega_{\mathrm{m}} t + \chi), \tag{3.2}$$

where s is the longitudinal coordinate along the accelerator, $B_1(s)$ is the rf quadrupole field strength, ω_{m} is the modulation angular frequency, and χ is the phase of the rf

quadrupole.

We consider N rf quadrupoles distributed in a storage ring. Note each time the particle passes through the rf quadrupole, it experiences a different quadrupole field strength. Therefore the Hamiltonian for particle motion is

$$H(y,y') = \frac{1}{2}y'^2 + \frac{1}{2}K_y(s)y^2 + \sum_{i=1}^{N}\sum_{n=-\infty}^{\infty}\frac{B_1(s_i)\ell_i}{2B\rho}\delta(s-s_i-nC)y^2\cos(\omega_{\rm m}t+\chi_i).$$

Transforming to the action-angle coordinates with the generating function

$$F_1(y,\phi_y) = -\frac{y^2}{2\beta_y}(\tan\phi_y - \frac{\beta_y'}{2}),$$

one obtains

$$\begin{aligned} H(J_y,\phi_y) &= \nu_y J_y + J_y\sum_{i=1}^{N}\sum_{n=-\infty}^{\infty}\frac{B_1(s_i)\ell_i\beta_y(s_i)}{2\pi B\rho}e^{jn(s-s_i)/R} \\ &\quad\times\cos^2(\phi_y+\mu_y(s_i)-\nu_y\frac{s_i}{R})\ \cos(\omega_{\rm m}t+\chi_i), \end{aligned} \tag{3.3}$$

where (J_y,ϕ_y) are conjugate action-angle coordinates, R is the average radius of the accelerator, ν_y is the tune of the betatron motion, and the following identity has been used

$$\sum_{n=-\infty}^{\infty}\delta(s-s_i-nC) = \frac{1}{C}\sum_{n=-\infty}^{\infty}e^{jn(s-s_i)/R}. \tag{3.4}$$

Expanding the Hamiltonian in revolution harmonics, one gets

$$\begin{aligned} H(J_y,\phi_y) &= \nu_y J_y + \frac{J_y}{2}\sum_{n=-\infty}^{\infty}\{A_{n,+,+}e^{j(2\phi_y+n\theta+\omega_{\rm m}t)} + A_{n,-,-}e^{j(-2\phi_y+n\theta-\omega_{\rm m}t)} + \\ &\quad A_{n,+,-}e^{j(2\phi_y+n\theta-\omega_{\rm m}t)} + A_{n,-,+}e^{j(-2\phi_y+n\theta+\omega_{\rm m}t)}\} + h(J_y,t), \end{aligned} \tag{3.5}$$

where $\theta = s/R$ is the orbiting angle around the accelerator, and $h(J_y,t)$ depends only on the time t and J_y, which is a fast oscillating term. This term can be ignored since

it doesn't affect the beam distribution, and

$$\begin{aligned} A_{n,\pm,\pm} &= \sum_{n=1}^{N} \frac{\beta_i B_1(s_i)\ell_i}{8\pi B\rho} e^{-jns_i/R \pm j(2\mu_y(s_i) - 2\nu_y s_i/R \pm \chi_i)} \\ &= \oint ds \frac{\beta(s)B_1(s)}{8\pi B\rho} e^{-jns/R \pm j(2\mu_y(s) - 2\nu_y s/R \pm \chi(s))}. \end{aligned} \tag{3.6}$$

Note that $d\phi_y/d\theta = \nu_y$. When the modulation tune $\nu_{\mathrm{m}} = \omega_{\mathrm{m}}/\omega_0$ is near a half integer betatron sideband, e.g. $\nu_{\mathrm{m}} \approx 2\nu_y - n$, the stationary phase term in the Hamiltonian dominates the dynamics, and the Hamiltonian can be approximated by

$$H(J_y, \phi_y) \approx \nu_y J_y + C_1 J_y \cos(2\phi_y - n\theta - \omega_{\mathrm{m}} t + \chi), \tag{3.7}$$

where we identify the Fourier amplitude as $A_{n,-,+} = C_1 e^{-j\chi}$. Here we define C_1 positive.

3.3 The Properties of the Hamiltonian

3.3.1 Linear Mathieu Instability

We transform the Hamiltonian (3.7) into a *resonance rotating frame* by using the generating function $F_2 = (\phi_y - \frac{1}{2}n\theta - \frac{1}{2}\nu_{\mathrm{m}}\theta + \chi)J$ to obtain a new Hamiltonian:

$$H(\psi, I) = \delta I + C_1 I \cos 2\psi, \tag{3.8}$$

where $I = J$, $\psi = \phi_y - \frac{1}{2}n\theta - \frac{1}{2}\nu_{\mathrm{m}}\theta + \chi$, and $\delta = |\nu_y - \frac{1}{2}n| - \frac{1}{2}\nu_m$ is called the *resonance proximity parameter*. Since the Hamiltonian (3.8) is time (θ) independent, the Hamiltonian is a constant of motion. It is equivalent to take the Poincaré surface of section at every $1/\nu_{\mathrm{m}}$ turns.

In the region of $-C_1 \leq \delta \leq +C_1$, the beam encounters the linear Mathieu instability driven by the rf quadrupole. The Hamiltonian (3.8) is stable when $|\delta| > C_1$.

Introducing the normalized coordinates: $Y = \sqrt{2I}\cos\psi$ and $P = -\sqrt{2I}\sin\psi$, the Hamiltonian is transformed to

$$H = \frac{1}{2}(\delta + C_1)Y^2 + \frac{1}{2}(\delta - C_1)P^2. \tag{3.9}$$

A torus associated with a constant Hamiltonian value is elliptical, and the stable fixed point is located at the origin with $I_{\text{sfp}} = 0$, or $X_{\text{sfp}} = P_{\text{sfp}} = 0$. The aspect ratio of the ellipse is $\sqrt{|(\delta + C_1)/(\delta - C_1)|}$. Adjusting the δ or C_1 parameters, one can adjust the shape of the admittance ellipse, and thus the rf quadrupole can be used to compensate injection mismatch.

Fig. 3.1 shows the trace of one single particle in the resonance rotating frame. Basically the particle just follows the torus of the Hamiltonian, however, note the small oscillation due to the incoherent terms in Eq. (3.5).

3.3.2 Nonlinear Mathieu instability

When a detuning term is included, e.g. in the presence of octupole magnets, the Hamiltonian becomes

$$H = \delta I + C_1 I \cos 2\psi + \frac{1}{2}\alpha_{yy} I^2, \tag{3.10}$$

where we neglect effects of higher order nonlinear resonances. The nonlinear detuning parameter α_{yy} may arise from the space charge force, the concatenating effects of sextupoles, and other higher order multi-poles. For example, the detuning parameter due to an octupole is $\alpha_{yy} = \frac{1}{16\pi}\oint \frac{B_3}{B\rho}\beta_y^2 ds$, where $B_3 = \partial^3 B_z/\partial x^3$ is the octupole field strength.

Actually the vector potential due to an octupole is $A_s = \frac{B_3}{24}(x^4 - 6x^2z^2)$, this adds into the Hamiltonain an additional term $\frac{B_3}{B\rho}\frac{R}{24}(x^4 - 6x^2z^2)$. Note the R factor is from

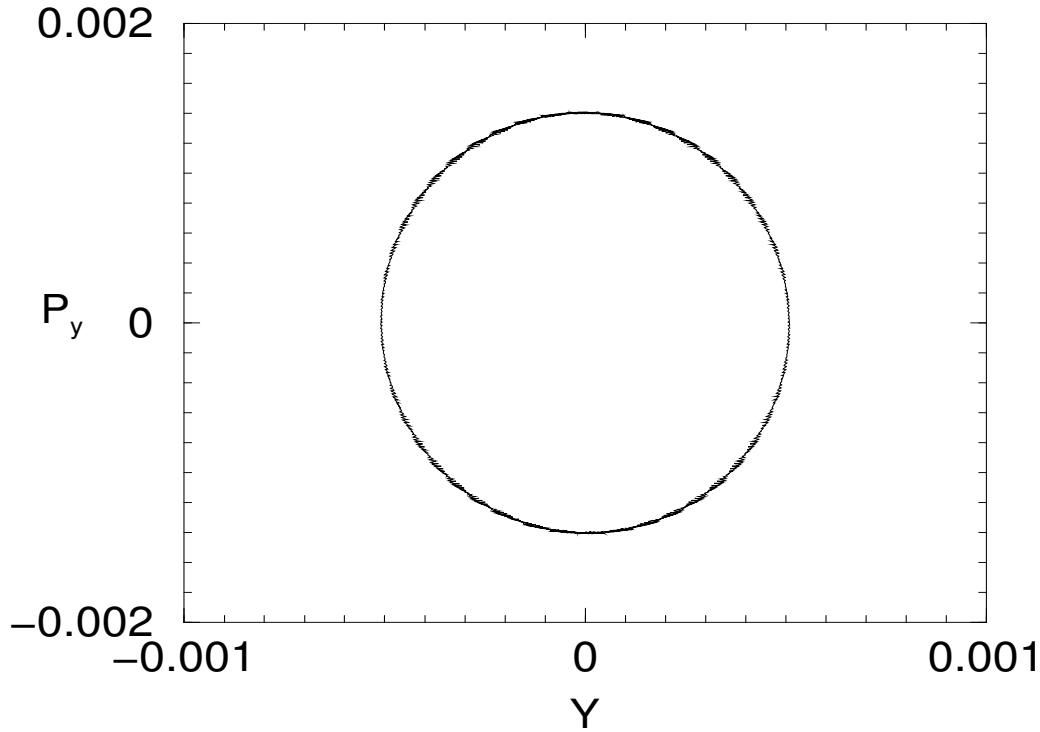

Figure 3.1: The trace of one single particle in the resonance rotating frame for the linear Hamiltonian. Parameters used are $\delta = 0.0013,\ C_1 = 0.001$.

the change of time from θ to s. Averaging over one turn, one gets

$$\begin{aligned}
& \frac{1}{2\pi}\oint d\theta \frac{R}{24}\frac{B_3}{B\rho}(x^4 - 6x^2z^2) \\
= & \frac{1}{2\pi}\oint ds \frac{1}{6}\frac{B_3}{B\rho}\beta^2 J^2 \cos^4\psi(s) \\
= & \frac{1}{2\pi}\oint ds \frac{1}{6}\frac{B_3}{B\rho}\beta^2 J^2 (\frac{3}{8} + \frac{1}{2}\cos 2\psi(s) + \frac{1}{8}\cos 4\psi(s)) \\
= & \frac{1}{2} \quad \frac{1}{16\pi}\oint \frac{B_3}{B\rho}\beta_y^2 ds \quad J^2
\end{aligned} \tag{3.11}$$

In the derivation, the x^2z^2 term is dropped because it does't attribute to the J^2 term. And the integral of any *cos* terms is zero on average.

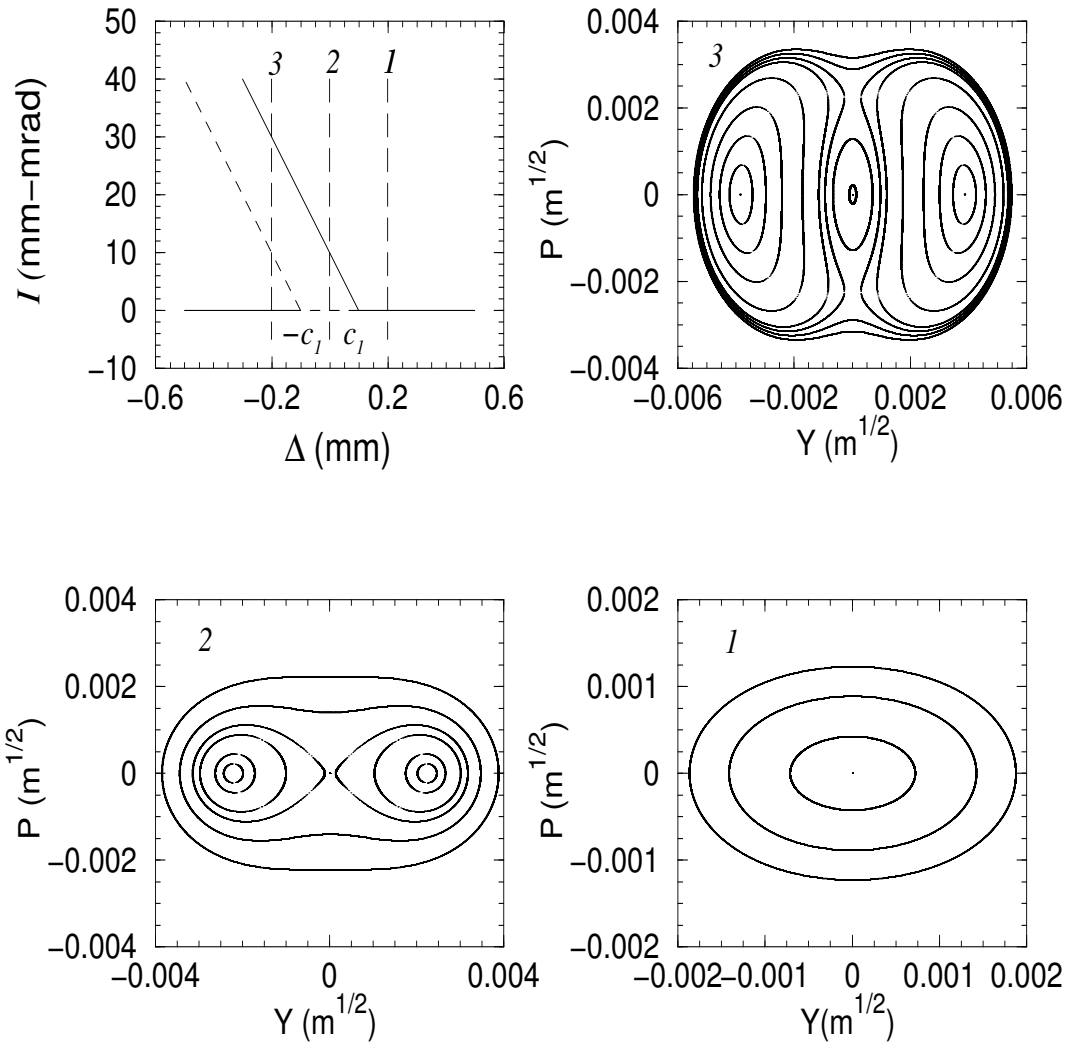

Figure 3.2: Top left: Stable (solid line) and unstable (short dashed line) fixed points vs the effective resonance proximity parameter $\Delta = \delta/\alpha_{yy}$ for the effective resonance strength parameter $c_1 = C_1/\alpha_{yy} = 0.10$ mm. The plots labeled (1), (2), and (3) correspond to the vertical long-dashed lines marked as (1), (2), and (3) respectively. The Hamiltonian is $H = \Delta I - c_1 I \cos 2\psi + \frac{1}{2}I^2$ with $Y = \sqrt{2I}\cos\psi$ and $P = -\sqrt{2I}\sin\psi$.

Fixed points can be obtained from Hamilton's equations: $\dot{I} = 0$ and $\dot{\psi} = 0$, where the over-dot represents the time(θ) derivative. The property of the Hamiltonian (3.10) depends on the signs of δ and α_{yy}. For example, if $\alpha_{yy} < 0$ and $C_1 > 0$, the stable fixed points are given by

$$I_{\text{sfp}} = \begin{cases} -\frac{1}{\alpha_{yy}}(\delta + C_1) & \text{if} \quad \delta > -C_1 \\ 0 & \text{if} \quad \delta > C_1 \text{ and } \delta < -C_1 \end{cases} \tag{3.12}$$

with $\psi_{\text{sfp}} = 0$ and π. The Hamiltonian value of the fixed point is $H_{\text{sfp}} = -\frac{1}{2}\alpha_{yy} I_{\text{sfp}}^2$. The corresponding unstable fixed points are located at

$$I_{\text{ufp}} = \begin{cases} -\frac{1}{\alpha_{yy}}(\delta - C_1) & \text{if} \quad \delta > C_1 \\ 0 & \text{if} \quad -C_1 < \delta < C_1 \end{cases} \tag{3.13}$$

with $\psi_{\text{ufp}} = \pi/2$ and $3\pi/2$. The Hamiltonian value of the separatrix torus is $H_{\text{ufp}} = -\frac{1}{2}\alpha_{yy} I_{\text{ufp}}^2$. The minimum action of the separatrix orbit is $I_{\text{sx,min}} = (\sqrt{-\delta} - \sqrt{C_1})^2/\alpha_{yy}$.

The top left plot of Fig. 3.2 shows the action of the fixed points vs the parameter δ/α_{yy} for a parameter $C_1/\alpha_{yy} = 0.10$ mm. Note that region (1) is below the bifurcation threshold and the phase-space is bifurcated into 2 islands in region (2) and is triplicated into 3 islands in region (3).

Fig. 3.3 shows the traces of a single particle in three different frequency regions in the resonance rotating phase space. Again one can see that the particle follows the Hamiltonian torus with a very small oscillation due to those dropped terms in Eq. (3.5).

3.3.3 The value of the nonlinear Hamiltonian

For the nonlinear Hamiltonian $H = \delta I + C_1 I \cos 2\psi + \frac{1}{2}\alpha_{yy} I^2$, the orientation is different between different signs of α_{yy}, as is reflected in the fixed points. The example of region 3 is shown in Fig. 3.4. Note the signs of δ are also changed correspondingly.

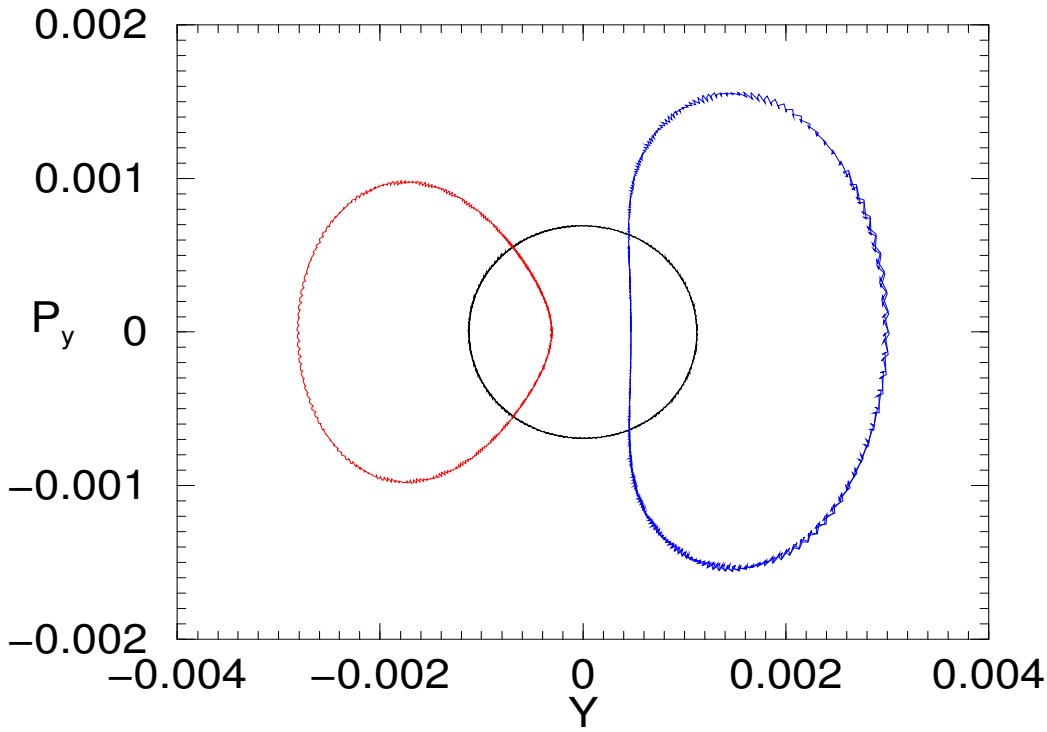

Figure 3.3: The traces of one single particle in 3 frequency regions in the resonance rotating frame. Parameters used are Left: $\delta = 0$, $C_1 = 0.001$, $\alpha_{yy} = -500$, Center: $\delta = -0.002$, $C_1 = 0.001$, $\alpha_{yy} = -500$, and Right: $\delta = 0.0013$, $C_1 = 0.001$, $\alpha_{yy} = -1000$.

Remember this is in the resonance rotating frame, the torus rotates if observed in the lab frame, therefore the different orientation doesn't change the physics except a phase difference. This phase difference will be taken into account in the mismatch application.

Since the other properties are the same for both cases, in the rest of this section we shall take $\alpha_{yy} < 0$ as an example. The Hamiltonian value plotted as function of J in horizontal and vertical directions are plotted in Fig. 3.5. In the horizontal direction,

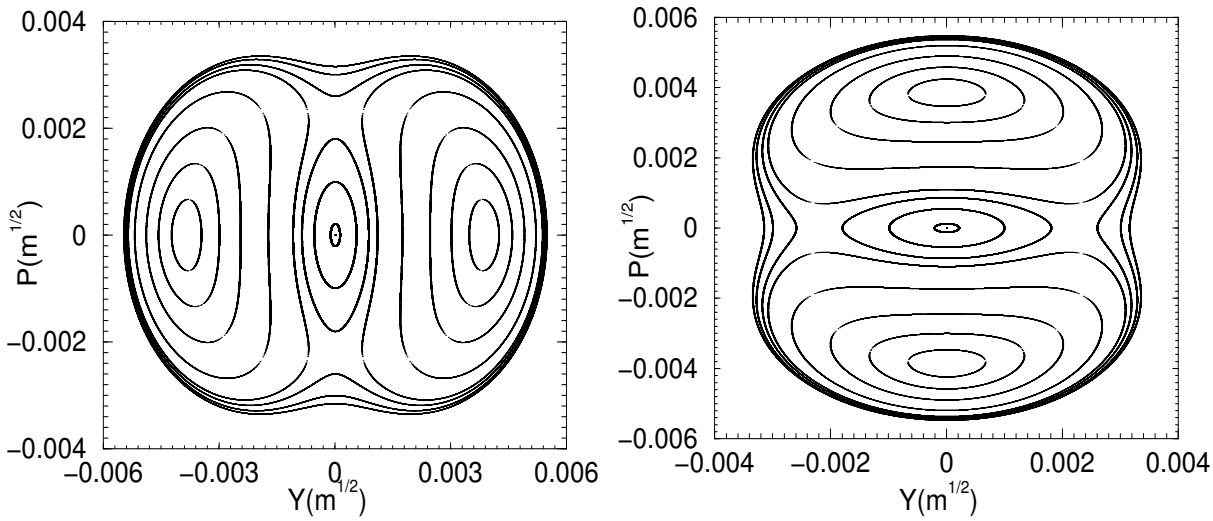

Figure 3.4: The orientation of the torus. The parameters used are Left: $\alpha_{yy} = -200$, $\delta = 0.001, C_1 = 0.0005$, Right: $\alpha_{yy} = 200$, $\delta = -0.001, C_1 = 0.0005$.

the origin and the maximum points correspond to the stable fixed points, however, in the vertical direction, the maximum points represent the unstable fixed points. The Hamiltonian value in the region 2 is plotted in Fig. 3.6. In this region, there are no fixed points in the vertical direction, therefore the value of the Hamiltonian increases or decreases monotonically in either side.

3.4 Hamiltonian Properties in Region 1

In this region the torus has the simplest form. The deformed torus is still alike to the original linear elliptical torus. However, we want to understand the beam properties in this region in detail because the emittance measurement will be applied in this region. It is also the basis to understand the properties in the other two regions.

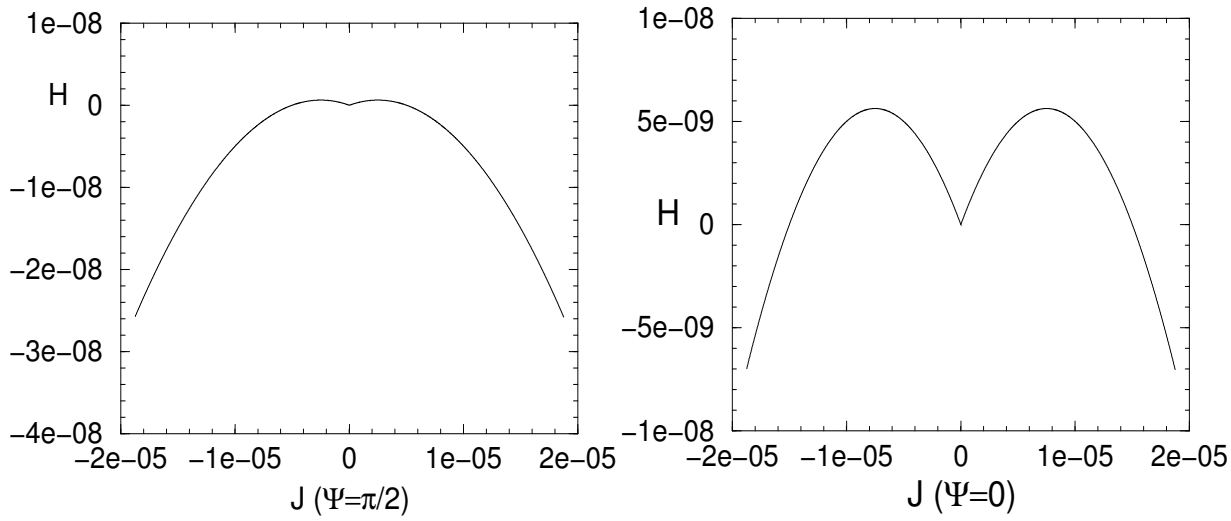

Figure 3.5: The Hamiltonian value as function of J for the left plot of Fig. 3.4. The parameters used are $\alpha_{yy} = -200,\ \delta = 0.001, C_1 = 0.0005$. Left plot is for the vertical direction and right plot is for the horizontal direction.

We again take $\delta < -C_1$ and $\alpha_{yy} < 0$ as an example. For a given Hamiltonian, the action is given by

$$J = \frac{1}{\alpha_{yy}}\Big[-(\delta + C_1\cos 2\psi) - \sqrt{(\delta + C_1\cos 2\psi)^2 + 2\alpha_{yy}H}\Big]. \tag{3.14}$$

Note the Hamiltonian is always less than zero.

The area enclosed by the torus can be calculated as

$$\begin{aligned} A(H) &= \oint J d\psi \\ &= \oint_0^{2\pi} d\psi \frac{1}{\alpha_{yy}}\Big[-(\delta + C_1\cos 2\psi) - \sqrt{(\delta + C_1\cos 2\psi)^2 + 2\alpha_{yy}H}\Big]. \end{aligned} \tag{3.15}$$

In the left frame of Fig. 3.7 the area is plotted against the Hamiltonian. Since the area in phase space represents energy, one would expect a linear relation between area and the corresponding Hamiltonian. However, the calculation result shows the relation is not simply linear.

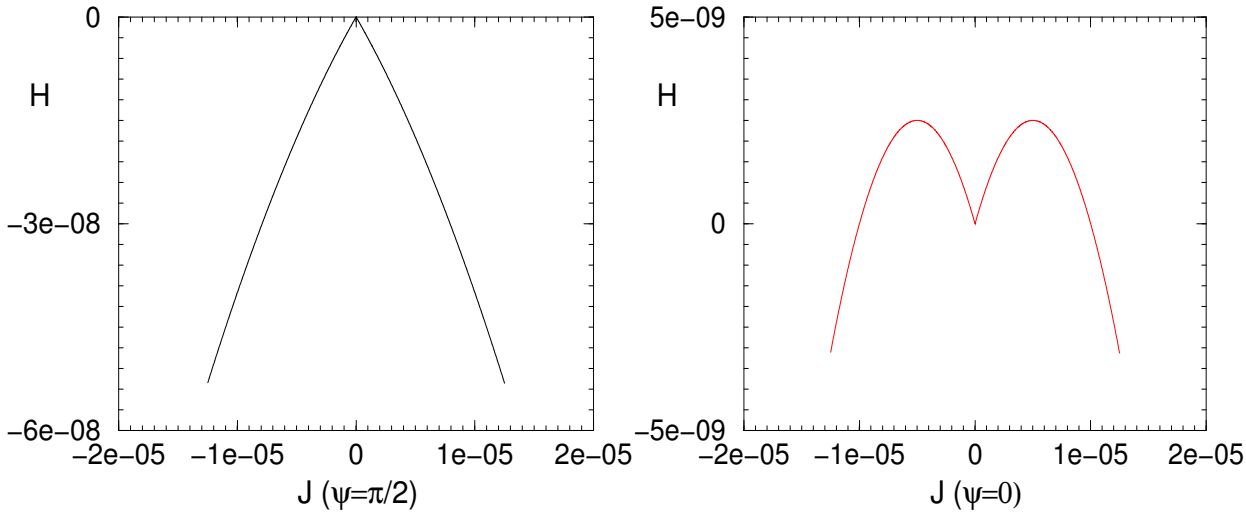

Figure 3.6: The Hamiltonian value as function of J in the region 2. The parameters used are $\alpha_{yy} = -200$, $\delta = -0.001, C_1 = 0.002$. Left plot is for the vertical direction and right plot is for the horizontal direction.

Although the torus is not elliptical, we can still define the aspect ratio as

$$R(H) = \frac{\sqrt{2J_{\psi=0}}}{\sqrt{2J_{\psi=\pi/2}}} = \frac{\sqrt{\delta + C_1 + \sqrt{(\delta + C_1)^2 + 2\alpha_{yy}H}}}{\sqrt{\delta - C_1 + \sqrt{(\delta - C_1)^2 + 2\alpha_{yy}H}}}. \tag{3.16}$$

According to the Hamilton's equations, we know

$$\dot{\psi} = \delta + C_1 \cos 2\psi + \frac{1}{2}\alpha_{yy}J = -\sqrt{(\delta + C_1 \cos 2\psi)^2 + 2\alpha_{yy}H}. \tag{3.17}$$

The minus sign means the particle moves clockwise in (J, ψ) phase space. And the period is given by

$$T(H) = \oint \frac{d\psi}{|\dot{\psi}|} = \oint_0^{2\pi} \frac{d\psi}{\sqrt{(\delta + C_1 \cos 2\psi)^2 + 2\alpha_{yy}H}}. \tag{3.18}$$

Therefore one can calculate the tune by $\Omega(H) = 2\pi/T(H)$. The tune versus the

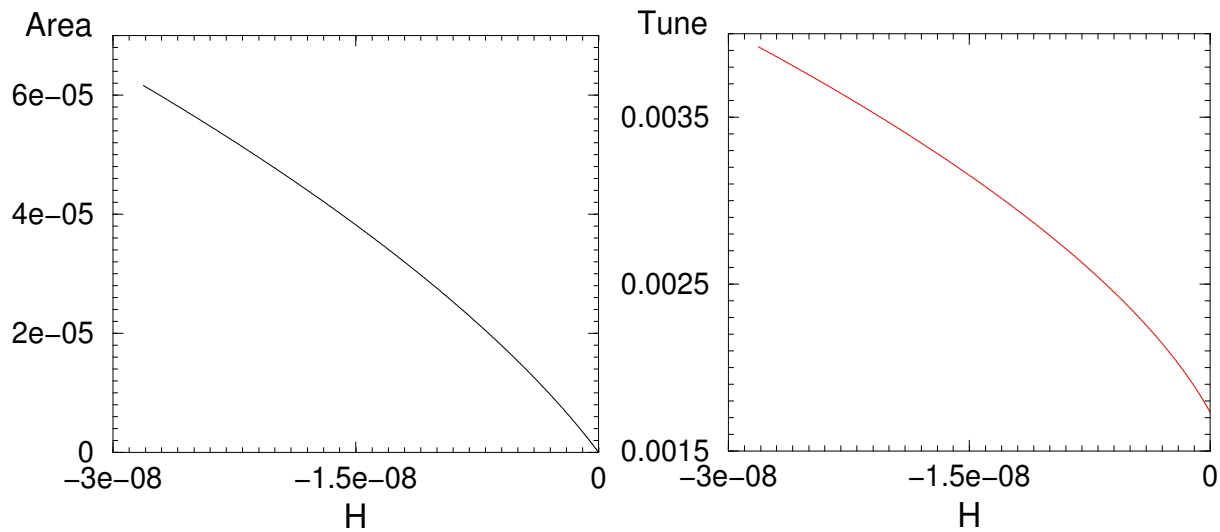

Figure 3.7: Left: the area enclosed by the torus of the Hamiltonian H. Right: the tune of the Hamiltonian. Note the tune at $J = 0$ goes back to $\sqrt{\delta^2 - C_1^2}$. Parameters used are $\alpha_{yy} = -200,\ \delta = -0.002,\ C_1 = 0.001$.

Hamiltonian is also plotted in Fig. 3.7. Note if $\alpha = 0$, we have

$$T(H_{linear}) = \oint_0^{2\pi} \frac{d\psi}{|\delta + C_1 \cos 2\psi|} = \frac{2\pi}{\sqrt{\delta^2 - C_1^2}}, \tag{3.19}$$

which agrees with the result of the linear Hamiltonian.

3.5 Beam-splitting in Region 2

Below the bifurcation threshold the emittance is fully preserved when we adiabatically change the parameters of the rf quadrupole. What happens at the bifurcation point? Particle simulation was done to study the beam properties at the bifurcation point.

As is shown in Fig. 3.9, the beam manipulation procedure goes as follows in the particle simulation. The rf quadrupole is initially adiabatically turned on to a preset

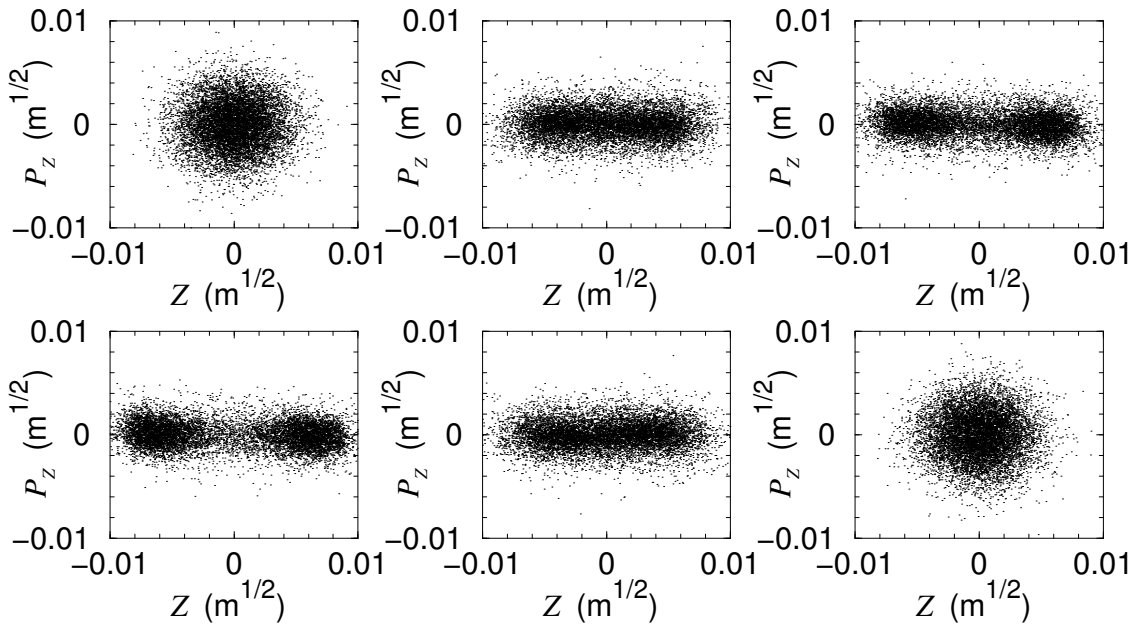

Figure 3.8: The evolution of bunch distribution as the rf quadrupole parameters are adiabatically changed. The beam splits into two beam-lets, and restore back to one. The normalized phase-space in this plot is defined as $Z = \sqrt{2I}\cos\psi$ and $P_Z = -\sqrt{2I}\sin\psi$. Parameters used in the numerical simulations at the bottom-left plot are $\delta = -0.006256$, $C_1 = 0.01$, and $\alpha_{yy} = -200$ m^{-1}. The times corresponding to these Poincareé surfaces of section are marked in Fig. 3.9.

value in a single fixed point region with $|\delta| > |C_1|$, then the modulation tune $\nu_{\rm m}$ is adiabatically changed to the condition $|\delta| \leq |C_1|$, where the stable fixed point is bifurcated into two stable fixed points. In this region, the unstable fixed point is located at $I_{\rm ufp} = 0$.

If the parameters of the rf quadrupole are changed adiabatically, particles are supposed to follow the Hamiltonian tori. Fig. 3.8 shows particles move into nonlinear

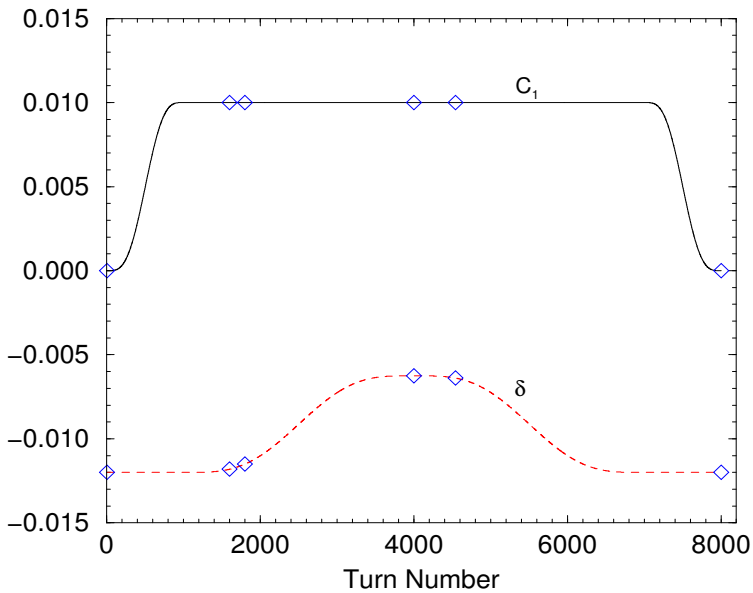

Figure 3.9: . The dashed and solid lines are the resonance proximity δ parameter and the rf quadrupole strength C_1 as functions of time (in revolution turns). The Poincareé surfaces of section plotted in Figs. 3.8 and 3.10 are marked as diamond symbols. The corresponding turn-numbers are: 0, 1600, 1800, 4000, 4540, and 8000.

Mathieu islands, where the times for the Poincareé surface of section (snapshot in the phase-space) are marked as diamond symbols in Fig. 3.9 with the corresponding machine parameters used in the multi-particle simulation.

The snapshots of the Poincareé surfaces-of-section are taken in the time-sequence from the top-left plot in the first row to the bottom-right plot of the second row. It seems that there is little emittance increase if the procedure is carried out properly.

However, if we inspect the physics more closely, the procedure is intrinsically non-adiabatic, and emittance increase is un-avoidable. Figure 3.10 shows the evolution of the 1σ-ellipse of the corresponding multi-particle simulation shown in Fig. 3.8 at

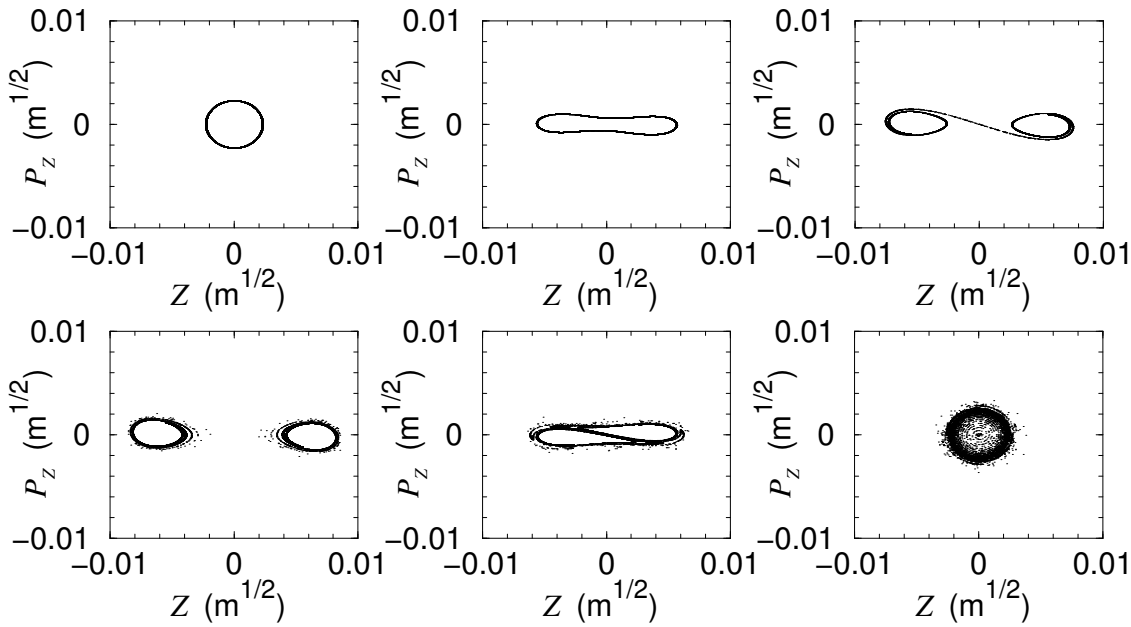

Figure 3.10: The evolution of the 1σ ellipse in the beam manipulation where the beam is moved adiabatically through the Mathieu bifurcation point and back. Parameters used in this simulation at the bottom-left plot are $\delta = -0.006256, C_1 = 0.01$, and $\alpha_{yy} = -200.\ \mathrm{m}^{-1}$

the exact times as shown in Fig. 3.9. As the phase-space is divided into two islands, the 1σ ellipse is wound into two islands. When the procedure is reversed, these two disjoint ellipses can not be restored into the original one, and the emittance can not be preserved during this process. In most applications, the increase of beam emittance is however reasonably small. The left plot of Fig. 3.11 shows the rms emittance increment ratio for $\alpha_{yy} = -400\ \mathrm{m}^{-1}$ ($\triangle$), $-600\ \mathrm{m}^{-1}$ ($\Diamond$), and $-1000\ \mathrm{m}^{-1}$ ($\bigcirc$) as a function of the I_{sfp} by changing the δ parameter at a constant $C_1 = 0.0004$.

Note that the emittance growth does not depend much on the α_{yy} parameter, but is a sensitive function of I_{sfp}. The emittance growth would be much larger if

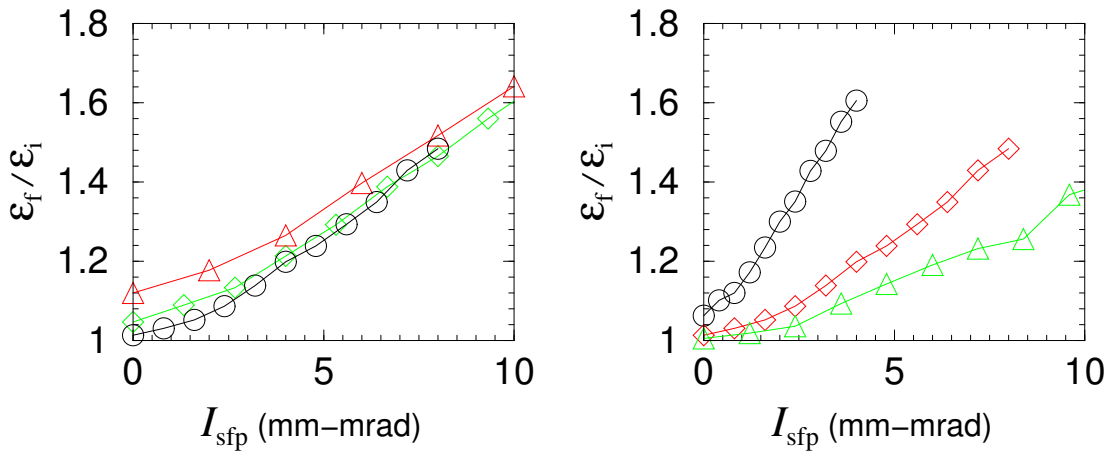

Figure 3.11: Left: Emittance increment ratio ϵ_f/ϵ_i after moving the beam to I_{sfp} and back for different α_{yy}. Parameters used in this calculation are $C_1 = 0.004$ with $\alpha_{yy} = -400$ m^{-1} ($\triangle$) -600 m^{-1} ($\diamondsuit$), and -1000. m^{-1} ($\bigcirc$) respectively. Right: Emittance increment ratio after moving the beam to I_{sfp} and back for different parameter C_1. Here, we use $\alpha_{yy} = -1000$ m^{-1}, with $C_1 = 0.006$ ($\triangle$), 0.004 ($\diamondsuit$), and 0.002 ($\bigcirc$) respectively.

the I_{sfp} goes beyond the second bifurcation region. The right plot of Fig. 3.11 shows the emittance growth factor as a function of I_{sfp} for a given α_{yy} with different C_1 parameter. For a smaller C_1 parameter, one has to set the δ parameter near the bifurcation of 3-island region to get the desired action I_{sfp}. The resulting emittance dilution becomes very large, because some particles are squeezed out of a bucket into another bucket. The adiabatically condition is not fulfilled, and the emittance dilution is inevitable.

3.6 Boltzmann Distribution in beam

3.6.1 Beam Distribution of the Ring Hamiltonian

As was discussed in Chapter Two, if a system is governed by a time-independent Hamiltonian, according to the Vlasov Equation, the equilibrium particle distribution must be a function of the Hamiltonian. The Boltzmann distribution is one of such distributions. In this section, we are going to discuss the conditions which lead to the Boltzmann distribution and deduce the explicit forms of the Boltzmann distribution for different Hamiltonians.

The Boltzmann distribution is given by

$$\rho_B(H) = \frac{1}{N} e^{-\frac{H}{E_t}}, \tag{3.20}$$

where N is the normalization factor and E_t is the thermal energy of the beam governed by the Hamiltonian H. Consider a beam with Gaussian distribution, namely,

$$\rho_G(J_y, \psi_y) = \frac{1}{2\pi\epsilon_0} e^{-\frac{J_y}{\epsilon_0}}, \tag{3.21}$$

where ϵ_0 is the rms emittance of the beam. The ring Hamiltonian in normalized phase space is given by

$$H = \nu_y J_y. \tag{3.22}$$

Comparing Eq. (3.20) with Eq. (3.21) and Eq. (3.22), one obtains

$$E_t = \Omega\epsilon_0, \tag{3.23}$$

and

$$\rho_B(H) = \frac{1}{2\pi\epsilon_0} e^{-\frac{H}{\Omega\epsilon_0}}, \tag{3.24}$$

where Ω is the tune of the Hamiltonian. Area in phase space represents 'energy', and this 'energy' is perserved in adiabatic beam manipulations. Therefore essentially the area of the torus of the Hamiltonian should be used as the distribution invariant. Notice $\frac{H}{\Omega}$ represents area in (H, t) phase space in case of the linear Hamiltonian. As we shall see later, Eq. (3.24) is only an approximation for the nonlinear Hamiltonian.

3.6.2 Beam Distribution for the Nonlinear Ring Hamiltonian

When a nonlinear detuning term is included, the Hamiltonian becomes $H(\psi, J_y) = \nu_y J_y + \frac{1}{2}\alpha_{yy} J_y^2$, and the Boltzmann distribution becomes

$$\rho_B(J_y, \psi_y) = \mathcal{N} e^{-\frac{\nu_y J + \frac{1}{2}\alpha_{yy} J^2}{E_t}}, \tag{3.25}$$

where we assume $\alpha_{yy} > 0$. The normalization constant $\mathcal{N}$ and the thermal energy are determined by the conditions:

$$\begin{cases} \int_0^\infty dJ_y \int_0^{2\pi} d\psi_y \rho_B(J_y, \psi_y) & = & 1 \\ \sqrt{\langle Y^2 \rangle \langle P_y^2 \rangle - \langle Y P_y \rangle^2} & = & \epsilon_0 \end{cases}, \tag{3.26}$$

where the average of a function f is defined by

$$\langle f \rangle = \int_0^\infty dJ_y \int_0^{2\pi} d\psi_y f \rho_B(J_y, \psi_y). \tag{3.27}$$

Note the first equation of Eq. (3.26) is the normalization equation of the distribution function, and the second equation is just the definition of the emittance.

From these conditions, we find

$$E_t = \nu_y \epsilon_0 \frac{\mathrm{erfcr}(u)}{2u^2(1 - \mathrm{erfcr}(u))} \tag{3.28}$$

$$\mathcal{N} = \frac{1}{2\pi\epsilon_0} \frac{2u^2(1 - \mathrm{erfcr}(u))}{(\mathrm{erfcr}(u))^2}, \tag{3.29}$$

where the reduced complementary error-function is

$$\mathrm{erfcr}(u) \equiv \sqrt{\pi}\, u e^{u^2} \mathrm{erfc}(u) = 1 - \frac{1}{2u^2} + \frac{1 \cdot 3}{(2u^2)^2} - \frac{1 \cdot 3 \cdot 5}{(2u^2)^3} + \ldots \tag{3.30}$$

with the complementary error-function defined as $\mathrm{erfc}(u) = \frac{2}{\sqrt{\pi}}\int_u^\infty e^{-y^2}dy$, and the parameter u is given by $u = \nu_y/\sqrt{2E_\mathrm{t}\alpha_{yy}}$. Since the parameter u depends on E_t, the thermal energy should be solved self-consistently from Eq. (3.28). In practice ν_y is much larger than $\sqrt{2E_\mathrm{t}\epsilon_0}$, we find $E_\mathrm{t} \approx \nu_y\epsilon_0$ and $\mathcal{N} \approx 1/(2\pi\epsilon_0)$. This is the unperturbed Gaussian distribution shown in Eq. (3.21), i.e. the nonlinear detuning does not substantially change the beam distribution.

In the case of $\alpha_{yy} < 0$, the Boltzmann distribution for the Hamiltonian $H(\psi, J_y) = \nu_y J_y + \frac{1}{2}\alpha_{yy}J_y^2$ still has the similar form. However, the distribution function has a minimum at $J_{turn} = -\nu_y/\alpha_{yy}$. Beyond this point, the value of the distribution function starts to increase. In fact that point is a fixed point of the Hamiltonian. However the Hamiltonian is not applicable when the action J_y is very large. More higher order terms must be considered to study the beam dynamics at that point. Note in practice J_y is usually less than $10^{-4} m \cdot rad$, and J_{turn} is of order of 10^2 to 10^3 $m \cdot rad$.

3.6.3 Beam Distribution for the Linear Perturbed Hamiltonian

For the Hamilton $H(J_y, \psi_y) = \delta J_y + C_1 J_y \cos 2\psi_y$, the tune can be calculated explicitly, hence the Boltzmann distribution is given by

$$\rho_B(J_y, \psi_y) = \frac{1}{2\pi\epsilon_0} e^{-\frac{\delta J_y + C_1 J_y \cos 2\psi_y}{\sqrt{\delta^2 - C_1^2}\epsilon_0}}. \tag{3.31}$$

Integrating over ψ, one obtains the distribution along the action J

$$\rho_B(J_y) = \frac{1}{2\pi\epsilon_0}\oint_0^{2\pi} d\psi e^{-\frac{\delta J_y + C_1 J_y \cos 2\psi_y}{\sqrt{\delta^2 - C_1^2}\epsilon_0}} = \frac{1}{\epsilon_0} I_0\left(\frac{C_1 J_y}{\sqrt{\delta^2 - C_1^2}\epsilon_0}\right) e^{-\frac{\delta J_y}{\sqrt{\delta^2 - C_1^2}\epsilon_0}}, \tag{3.32}$$

where I_0 is the zeroth order of the modified Bessel function of the first kind. Therefore one would expect a longer tail due to the Bessel function. Using the normalized

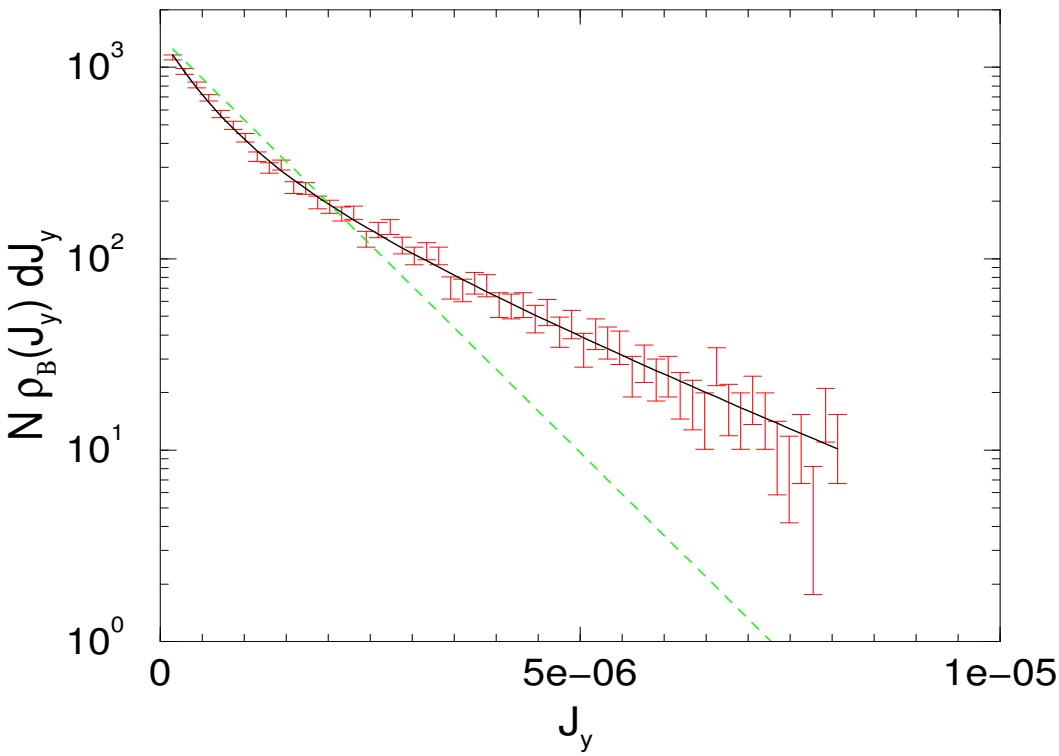

Figure 3.12: The beam distribution of the linear Hamiltonian. The circles are obtained from particle simulation, and the solid line is given by Eq. (3.32). The dotted line of Gaussian distribution is also plotted for comparison. The Gaussian distribution is given by $\rho(J) = \frac{1}{\epsilon}e^{-J/\epsilon}$. Parameters used are $\epsilon = 1 \times 10^{-6} m \cdot rad$, $\delta = 0.0013$, $C_1 = 0.001$. There are 10,000 particles in the simulation and the sampling width is 1.132×10^{-7}.

coordinates $Y = \sqrt{2J_y}\cos\psi$, $P_y = -\sqrt{2J_y}\sin\psi$, the distribution function becomes

$$\rho_B(Y, P_y) = \frac{1}{2\pi\epsilon_0} e^{-\frac{(\delta+C_1)Y^2}{2\sqrt{\delta^2-C_1^2}\epsilon_0}} e^{-\frac{(\delta-C_1)P_y^2}{2\sqrt{\delta^2-C_1^2}\epsilon_0}}, \tag{3.33}$$

which is a bi-Gaussian.

Fig. 3.12 shows the particle distribution as function of the action J. Fig. 3.13

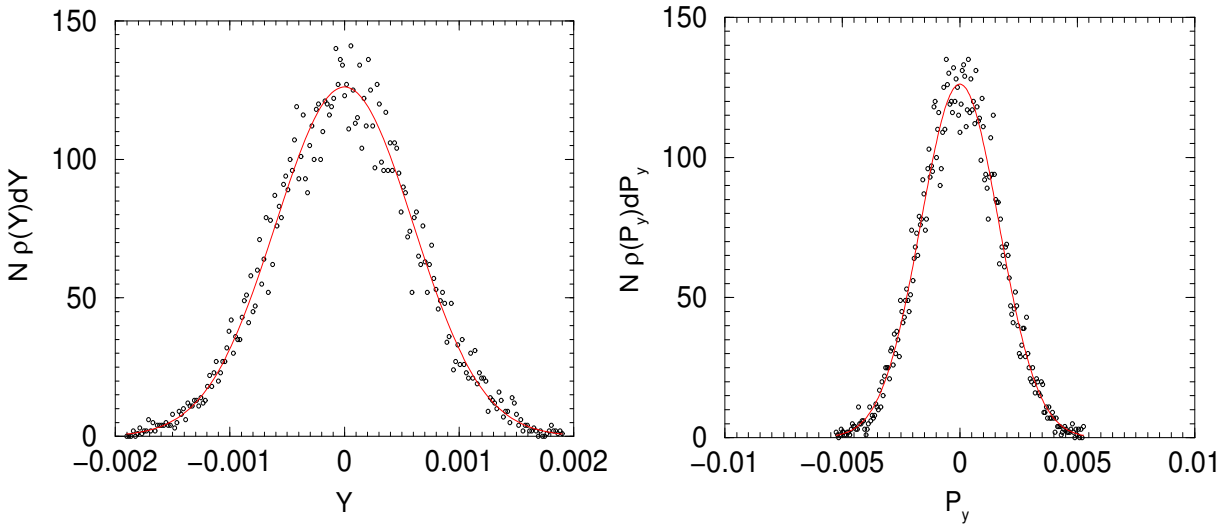

Figure 3.13: The particle distribution along Y or P_y in the same particle simulation as of Fig. 3.12. The circles are obtained from simulation and the solid line is Gaussian distribution given by $\rho(x) = 1/\sqrt{2\pi}\sigma_x e^{-x^2/2\sigma_x^2}$. In the simulation, $\sigma_y^2 = \sqrt{\frac{\delta - C_1}{\delta + C_1}}\epsilon = 3.6 \times 10^{-7}$, $\sigma_p^2 = \sqrt{\frac{\delta + C_1}{\delta - C_1}}\epsilon = 2.8 \times 10^{-6}$, where $\epsilon = 1 \times 10^{-6}$m·rad is the initial emittance. Other parameters are $\delta = 0.0013$, $C_1 = 0.001$ and $N = 10,000, dy = 1.9 \times 10^{-5}, dp = 5.3 \times 10^{-5}$.

shows the particle distribution along Y or P_y direction. From the above figures, one can see that the particle distribution obtained from particle simulation agrees very well with the Boltzmann distribution.

3.6.4 Beam Distribution for the Nonlinear Perturbed Hamiltonian

For the nonlinear Hamiltonian $H(J_y, \psi_y) = \delta J_y + J_y C_1 \cos 2\psi_y + \frac{1}{2}\alpha_{yy} J_y^2$, the tune is not a constant, consequently the distribution is much more complicated. Here

we are concerned only with the distribution in region 1. According to our previous discussion, the phase space area is preserved during the beam manipulation, therefore the distribution should have the following form

$$\rho(H) = \frac{1}{N} e^{-\frac{Area(H)}{2\pi\epsilon}}. \tag{3.34}$$

Unfortunately, we find in Fig. 3.7 that the relation between the Area and the value of the Hamiltonian is not linear. Therefore in this case the Boltzmann distribution is only a first order approximation.

If we write the Boltzmann distribution as

$$\rho_B(J_y, \psi_y) = \frac{1}{N} e^{-\frac{\delta J_y + C_1 J_y \cos 2\psi_y + \frac{1}{2}\alpha_{yy} J_y^2}{E_t}}, \tag{3.35}$$

then normalization factor N and the thermal energy E_t can again be solved from Eq. (3.26). Detailed discussion of solving these equations can be found in Appendix B.

In practice, however, one can use a bi-Gaussian distribution function similar to that of the linear Hamiltonian as following

$$\rho(Y, P_y) = \frac{1}{2\pi\epsilon_0} e^{-\frac{Y^2}{2\sigma_y^2}} e^{-\frac{P_y^2}{2\sigma_{P_y}^2}} \tag{3.36}$$

with

$$\begin{cases} \sigma_y^2 & = & \sqrt{\frac{\delta_e - C_1}{\delta_e + C_1}}\epsilon_0 \\ \sigma_{P_y}^2 & = & \sqrt{\frac{\delta_e + C_1}{\delta_e - C_1}}\epsilon_0 \end{cases}, \tag{3.37}$$

and the effective proximity parameter δ_e is given by

$$\delta_e = \delta + F\alpha_{yy}\epsilon_0, \tag{3.38}$$

and the factor $F \approx 2.5 \pm 0.2$ is obtained from particle simulation. Note δ always has the same sign as α_{yy} in region 1.

Fig. 3.14 shows the beam distribution results obtained from particle simulation. The particle distribution in (Y, P_y) phase space is well approximated by a bi-Gaussian distribution in very large ranges of the parameters, except that the real distribution seems to have a broader or sharper top. One can understand this by comparing the torus of the Hamiltonian with an ellipse. The torus looks like a swelled ellipse which causes the difference of the distribution.

The beam distribution along J is more complicated. When the detuning parameter α_{yy} is small, the distribution looks like the distribution of the linear Hamiltonian. One can compare the top-left plot in Fig. 3.15 with Fig. 3.12. While α_{yy} is large, the distribution tends to a Gaussian distribution! The corresponding distribution in (Y, P_y) phase space is shown in Fig. 3.16. Note the distribution is still bi-Gaussian, even for a huge α_{yy} parameter. Although one can understand the detuning term $\frac{1}{2}\alpha_{yy}J^2$ suppresses the long tail, the agreement with Gaussian in the lower-right plot of Fig. 3.15 is still a surprise.

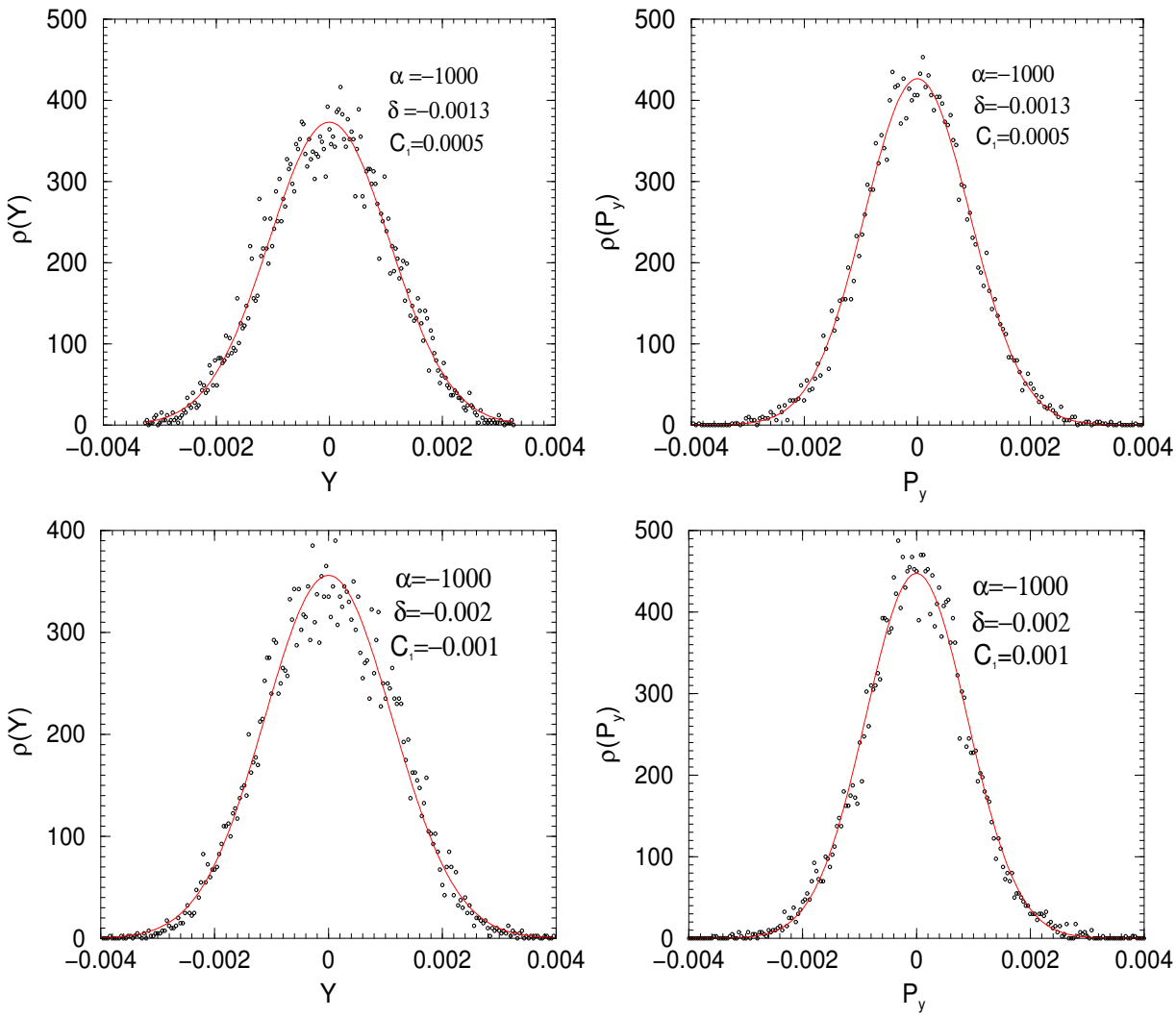

Figure 3.14: The beam distribution against Y or P_y for the nonlinear Hamiltonian in the resonance rotating frame. The circles are obtained from particle simulation, and the solid line is Gaussian distribution given by $\rho(x) = \frac{1}{\sqrt{2\pi}\sigma_x} e^{-x^2/2\sigma_x^2}$. σ_Y or σ_{P_y} is given by Eq. (3.37). In the simulation $\epsilon = 1 \times 10^{-6} m \cdot rad$.

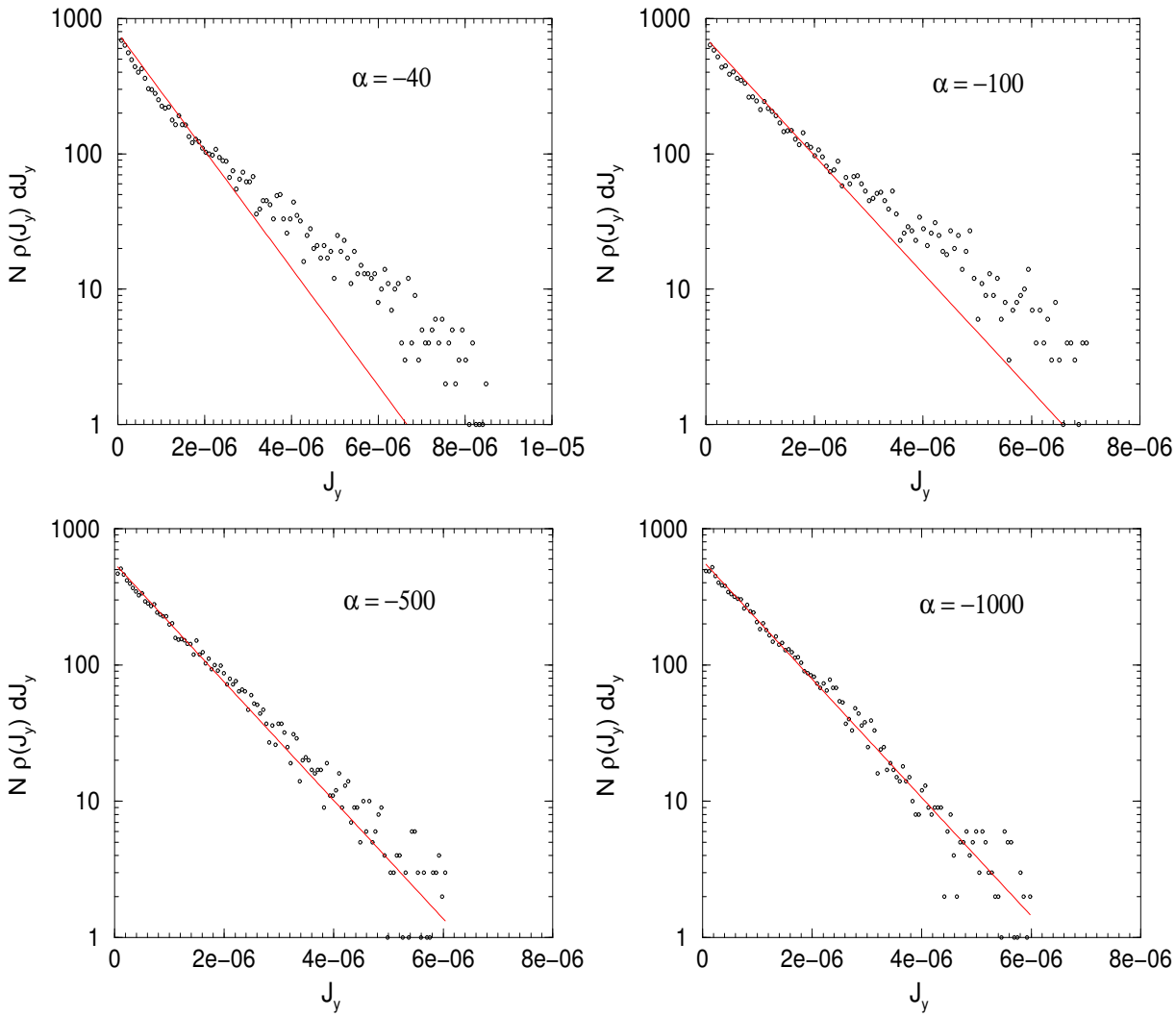

Figure 3.15: The beam distribution against action J_y for the nonlinear Hamiltonian. The circles are obtained from particle simulation, and the solid line is Gaussian distribution given by $\rho(J) = \frac{1}{\epsilon}e^{-J/\epsilon}$. α_{yy} is written in the plots, the other parameters are $\epsilon = 1\times10^{-6} m\cdot rad$, $\delta = -0.0013$, $C_1 = 0.001$. There are 10,000 particles in the simulation and the widths of the sampling slot are around 6×10^{-8}.

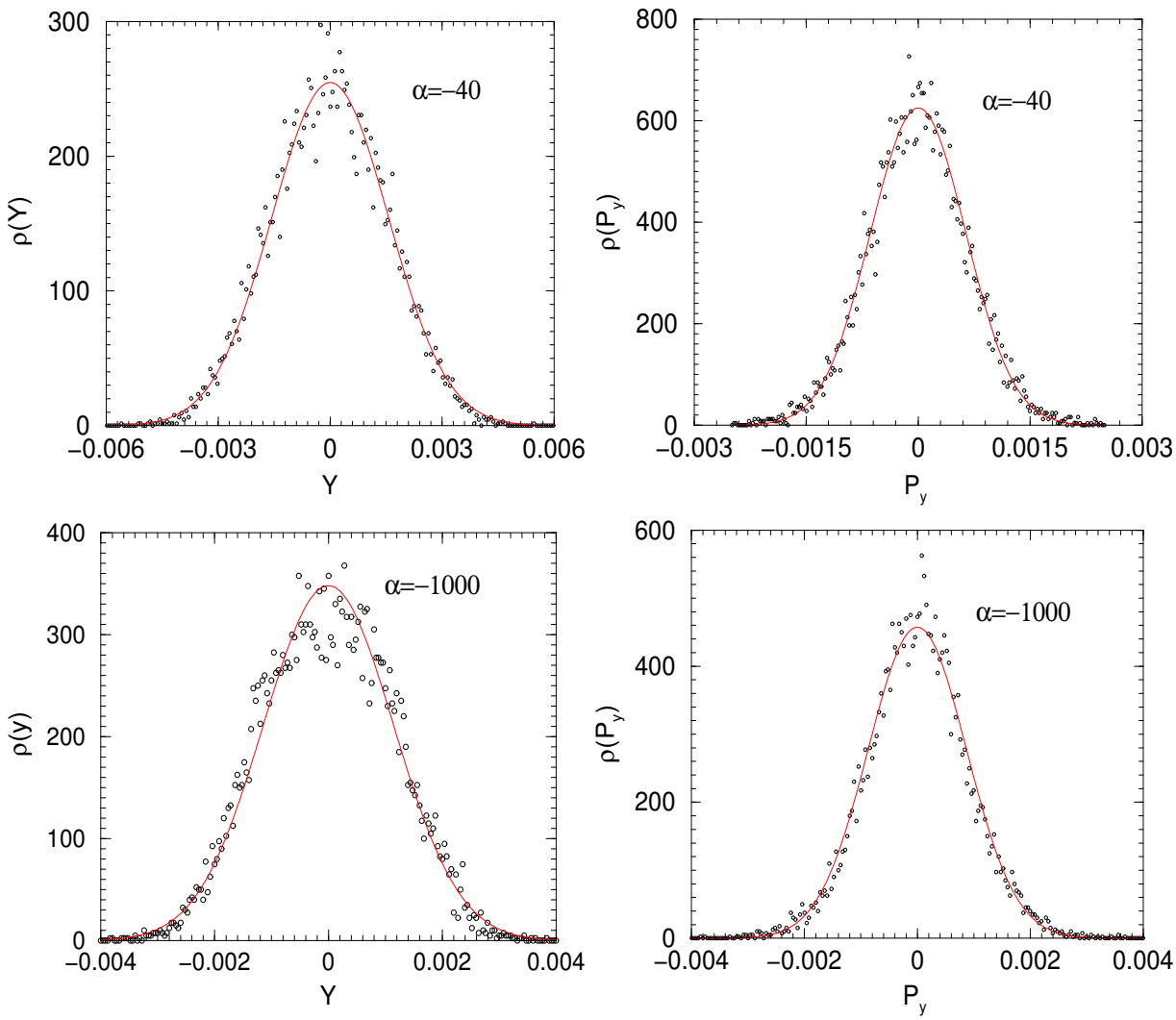

Figure 3.16: The beam distribution against Y or P_y for the nonlinear Hamiltonian in the resonance rotating frame. The circles are obtained from particle simulation, and the solid line is Gaussian distribution given by $\rho(x) = \frac{1}{\sqrt{2\pi}\sigma_x} e^{-x^2/2\sigma_x^2}$. σ_Y or σ_{P_y} is given by Eq. (3.37). α_{yy} is written in the plots, the other parameters are $\epsilon = 1 \times 10^{-6} m \cdot rad$, $\delta = -0.0013$, $C_1 = 0.001$.

Chapter 4

Applications of RF Quadrupole

4.1 Emittance Measurement

Using a Beam Position Monitor(BPM) to measure beam moments dates back to the 1960's [10]. However, the method was not widely used until R. H. Miller presented it at the 12th International Conference on High- Energy Accelerators in 1983 [11] although he actually was not aware of Gol'din 's paper [12]. Recently several laboratories have applied this method to their machines.

As is pointed out by Miller, four devices can be used to measure the quadrupole moment including

1. a strip line position monitor,
2. a cylindrical microwave cavity resonant in the $TM_{2,1,0}$ mode at the rf frequency of the beam,
3. a resistively loaded insulated gap in the beam pipe with voltage monitors at four points around the gap, and
4. four magnetic pickup loops located at 90° intervals around the beam pipe.

All of these devices depend on the beam having a short time structure. Each devices measures the $\cos 2\theta$ component of the image currents. For a long beam pulse the $TM_{2,1,0}$ microwave cavity is probably the most sensitive transducer, while for the very short pulses the strip-line position monitors are ideal.

The principle of BPM can be found in appendix B. For a linear accelerator or beam transport line the emittance measurement with BPM is straightforward. This is because the beam width can be changed by the quadrupoles upstream of the BPM. One can even calibrate the BPM with a dipole kick to the beam [13]. Because this method doesn't require prior knowledge of the beam distribution, it can be applied to non-Gaussian beam, e.g., a sub-picosecond beam from photo-injector [14]. Later interests were turned to mismatch correction with BPM in the ring accelerator [15]. The idea is to minimize the quadrupole mode oscillation to obtain the best match. Emittance measurement in storage rings with BPM has not been fully successful because the rms signal derived from a BPM is weak and the rms beam-width can not easily be modified by a quadrupole [16].

As we described in Chapter Three, the rf quadrupole modulates the beam width. Therefore we can get an AC quadratic signal from BPM, and the amplitude can be precisely obtained by Fourier transformation. Furthermore, the amplitude of the oscillation is controlled by rf quadrupole. Consequently the emittance can be derived from the fitting between rf quadrupole parameters and the BPM signal.

4.1.1 Quadrupole Mode Transfer Function

The induced surface charge density on a conducting cylinder by an infinitely long line charge is

$$\sigma(r, \phi, a, \Theta) = \frac{\lambda}{2\pi a} \frac{a^2 - r^2}{a^2 + r^2 - 2ar\cos(\Theta - \phi)}, \tag{4.1}$$

where $\lambda = N_B e/(\sqrt{2\pi}\sigma_s)$ is the line charge density, e is the charge of the orbiting particle, N_B is the number of particles in a bunch, σ_s is the rms bunch length, (r, ϕ) is the location of the line charge in cylindrical coordinate system, (a, Θ) is the position on the conducting cylinder with radius a. Usually the radius r of the charge particle is much smaller than the BPM chamber radius a. Hence one can expand the charge density in power series of r/a

$$\begin{aligned}
&\sigma(r, \phi, a, \Theta) \\
&= \frac{\lambda}{2\pi a}[1 + 2\sum_{k=1}^{\infty}(\frac{r}{a})^k \cos k(\Theta - \phi)] \\
&= \frac{\lambda}{2\pi a}\{1 + 2[\frac{x}{a}\cos\Theta + \frac{z}{a}\sin\Theta] \\
&\quad +2[\frac{x^2 - z^2}{a^2}\cos 2\Theta + 2\frac{xz}{a^2}\sin 2\Theta] \\
&\quad +\text{higher order terms}\},
\end{aligned} \tag{4.2}$$

where $x = r\cos\phi, z = r\sin\phi$ are the coordinates for the line charge.

Now consider a beam with normalized distribution function $\rho(x, x', z, z')$, where (x, x') and (z, z') are the transverse phase-space coordinates of betatron motion, then the total charge density on the BPM is given by

$$\begin{aligned}
\sigma(a, \Theta) &= \int dxdx'dzdz'\sigma(r, \phi, a, \Theta)\rho(x, x', z, z') \\
&= \frac{\lambda}{2\pi a}\{1 + 2[\frac{x_0}{a}\cos\Theta + \frac{z_0}{a}\sin\Theta] \\
&\quad +2[\frac{\langle x^2\rangle - \langle z^2\rangle}{a^2}\cos 2\Theta + 2\frac{x_0 z_0}{a^2}\sin 2\Theta] \\
&\quad +\text{higher order terms}\},
\end{aligned} \tag{4.3}$$

where $x_0 = \int dxdx'dzdz'\, x\, \rho(x, x', z, z')$, $z_0 = \int dxdx'dzdz'\, z\, \rho(x, x', z, z')$ are the coordinates of the beam centroid.

When the rf quadrupole is turned on, the deformed tori of the Hamiltonian rotate in normalized phase space at a tune of $\frac{1}{2}\nu_m$. Therefore the beam distribution changes

with time according to

$$\rho(J,\psi(t)) = \rho(J,\psi + \frac{1}{2}\nu_m\omega_0 t), \tag{4.4}$$

where ω_0 is the particle revolution angular frequency.

If we set the modulation frequency $\nu_m \sim 2\nu_x$, and make it work in the one stable fixed point side, i.e., region 1 in the plot of Fig. 3.2, then the rf quadrupole affects the horizontal phase space only. This is because usually ν_x and ν_z are apart by at least 10^{-1}, and the effective range of rf quadrupole is $2(\nu_{x\,\mathrm{or}\,z} \pm 10^{-2})$, therefore rf quadrupole only perturbs one plane.

Considering the integral $\int dxdx'\, x_r^2\, \rho(x,x')$ in normalized phase space, where $x_r = x - x_0$, one gets

$$\begin{aligned}
&\int dxdx' x_r^2 \rho(x,x') \\
&= \int dJd\psi(t) 2\beta_x J \cos^2\psi(t)\rho(J,\psi(t)) \\
&= \int dJd\psi(t)\ 2\beta_x J\cos^2\psi(t)\ \rho(J,\psi + \frac{1}{2}\nu_m\omega_0 t) \\
&= \int dJd\psi\ 2\beta_x J\cos^2(\psi - \frac{1}{2}\nu_m\omega_0 t)\ \rho(J,\psi).
\end{aligned} \tag{4.5}$$

Note although $dxdx' = \beta_x dJd\psi$, $\rho(x,x')dxdx' = \rho(J,\psi)dJd\psi$, namely, the possibility of the particle staying in the same phase space range must be the same. Now integrating in the resonance rotating frame,

$$\begin{aligned}
&\int dxdx' x_r^2 \rho(x,x') \\
&= \int dJd\psi(t)\ 2\beta_x J\ \rho(J,\psi(t)) \\
&\quad \times(\cos^2\psi(t)\cos^2\frac{1}{2}\nu_m\omega_0 t + \sin^2\psi(t)\sin^2\frac{1}{2}\nu_m\omega_0 t + \cos\psi(t)\sin\psi(t)\sin\nu_m\omega_0 t) \\
&= \beta_x\langle X^2\rangle\cos^2\frac{1}{2}\nu_m\omega_0 t + \beta_x\langle P_x^2\rangle\sin^2\frac{1}{2}\nu_m\omega_0 t - \beta_x\langle XP_x\rangle\sin\nu_m\omega_0 t \\
&= \frac{1}{2}\beta_x(\langle X^2\rangle + \langle P_x^2\rangle) + \frac{1}{2}\beta_x(\langle X^2\rangle - \langle P_x^2\rangle)\cos\nu_m\omega_0 t,
\end{aligned} \tag{4.6}$$

where $X = \sqrt{2J}\cos\psi$, $P_x = -\sqrt{2J}\sin\psi$ are the normalized coordinates, $\langle X^2\rangle = \int X^2\rho(J,\psi)dJd\psi$. Here $\rho(J,\psi)$ is the Boltzmann distribution as we described in Chapter Three. The $\langle XP_x\rangle$ term is dropped due to the symmetry of Boltzmann distribution.

When the frequency of the rf quadrupole is close to $2\nu_x$, the quadratic signal picked up by the BPM is given by

$$\begin{aligned} q_2 &= \frac{\sigma(a,0)+\sigma(a,\pi)-\sigma(a,\frac{\pi}{2})-\sigma(a,\frac{3\pi}{2})}{\sigma(a,0)+\sigma(a,\pi)+\sigma(a,\frac{\pi}{2})+\sigma(a,\frac{3\pi}{2})} \\ &= \frac{2}{a^2}\big[x_0^2 - z_0^2 - \langle z_r^2\rangle + \frac{1}{2}\beta_x(\langle X^2\rangle + \langle P_x^2\rangle) \\ &\quad + \frac{1}{2}\beta_x(\langle X^2\rangle - \langle P_x^2\rangle)\cos\nu_m\omega_0 t\big] \\ &= \frac{1}{a^2}(b_0 + b_1\cos\nu_m\omega_0 t), \end{aligned} \tag{4.7}$$

where

$$b_0 = 2(x_0^2 - z_0^2 - \langle z_r^2\rangle) + \beta_x\langle X^2\rangle + \beta_x\langle P_x^2\rangle \tag{4.8}$$

$$b_1 = \beta_x(\langle X^2\rangle - \langle P_x^2\rangle), \tag{4.9}$$

and $\sqrt{\langle z_r^2\rangle}$ is the unperturbed half beam width in z direction. Although the DC component b_0 of the quadrupole moments q_2 is much larger than the modulation b_1, the coefficient b_1 can, however, be accurately determined by a Fourier transformation of the quadrupole pickup signal. Here the coefficient b_1 is called the quadrupole-mode transfer function now that the amplitude of b_1 changes with the working frequency of the rf quadrupole.

4.1.2 Linear Hamiltonian

Now let's calculate$\langle X^2\rangle$ and $\langle P_x^2\rangle$ in the resonance rotating frame. First consider the linear case, i.e., $\alpha_{xx} = 0$. The Hamiltonian is given by

$$\begin{aligned} H &= \delta J + JC_1 \cos 2\psi \\ &= \frac{1}{2}(\delta + C_1)X^2 + \frac{1}{2}(\delta - C_1)P_x^2. \end{aligned} \tag{4.10}$$

The stable condition for this linear Hamiltonian is $|\delta| > C_1$.

The Boltzmann distribution is expressed as

$$\rho(H) = \frac{1}{N} \exp \frac{H}{\Omega\epsilon_0}, \tag{4.11}$$

where $\Omega = \sqrt{\delta^2 - C_1^2}$ is the tune of the Hamiltonian, ϵ_0 is the rms emittance of the beam and $N = 2\pi\epsilon_0$ is the normalization factor. One can easily obtain

$$\langle X^2\rangle = \sqrt{\frac{\delta + C_1}{\delta - C_1}}\epsilon_0, \tag{4.12}$$

$$\langle P_x^2\rangle = \sqrt{\frac{\delta - C_1}{\delta + C_1}}\epsilon_0. \tag{4.13}$$

Therefore

$$b_1 = \beta_x(\langle X^2\rangle - \langle P_x^2\rangle) = \frac{2\beta_x C_1\ \epsilon_0}{\sqrt{\delta^2 - C_1^2}}, \tag{4.14}$$

or

$$\delta^2 = 4C_1^2\ \beta_x^2\epsilon_0^2\frac{1}{b_1^2} + C_1^2, \tag{4.15}$$

where β_x is the betatron amplitude function at the location of the Beam Position Monitor. Therefore measuring the b_1 coefficient versus the machine parameter $\delta = |\ \nu_x - \frac{1}{2}n\ | - \frac{1}{2}\nu_m$(by varying ν_m) can be used to determine the emittance ϵ_0. This provides an experimental method to measure the beam emittance. In this method, two aspects help improve the precision, namely

1. the coefficient b_1 is calculated from Fourier transformation, and

2. the emittance is obtained by a linear fitting.

In order to increase the amplitude of b_1, one can tune ν_m such that δ is close to C_1. In other words, make rf quadrupole work at the frequency close to the resonance frequency. It is also worth pointing out that δ must be much less than $\nu_z - \nu_x$, thus the operation in one plane won't affect the particle motion in the other plane. The rf quadrupole must be adiabatically turned on and off to ensure the emittance preservation during this process.

Particle simulation was done to test this method. 10,000 particles were initiated in Gaussian distribution, each turn the particles passed through a one turn map matrix and an rf quadrupole matrix. In the first 1000 turns, the strength of the rf quadrupole increased adiabatically, while the modulation tune was maintained at a constant value. During 1001 to 2000 turn, rf quadrupole ran at fixed amplitude and frequency so the particle distribution reached equilibrium. From 2001 to 4000 turn, $< x^2 > - < x >^2$ was calculated turn by turn. After Fourier transformation the parameters b_0 and b_1 were obtained. Fig. 4.1 shows the quadrupole moment as a function of revolution turns and the FFT spectrum. Figure 4.2 shows the parameter δ^2 versus the derived Fourier amplitude $1/b_1^2$ from data of multi-particle simulations with an initial emittance 1.0 π-mm-mrad. Using Eq. (4.14), one can deduce emittance from the slope with the error of less than 3%. We note that, indeed, the curve is linear for the linear betatron system, and the slope can be used to derive the emittance quite accurately. The intercept of the line with the vertical axis at $\delta = C_1$ can be used to determine the betatron tune.

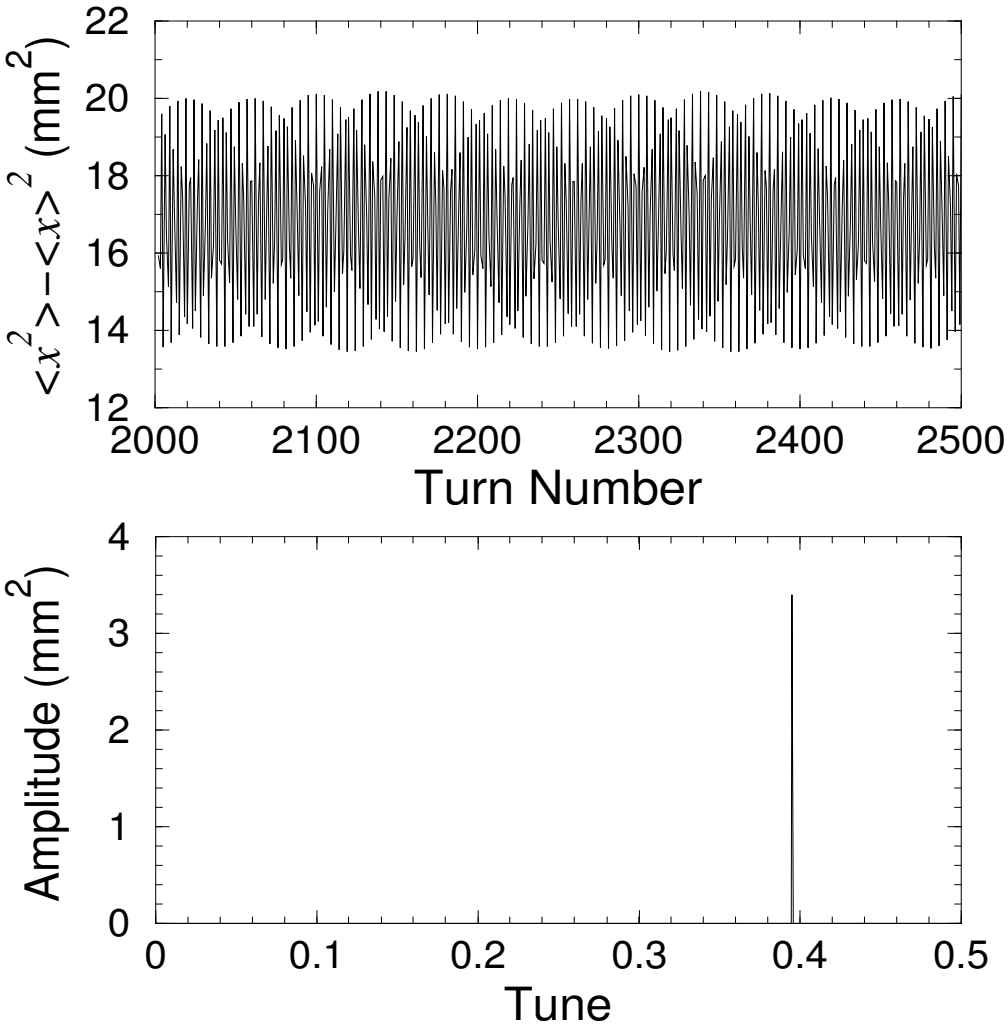

Figure 4.1: Top: The second moment ($\langle x^2 \rangle - \langle x \rangle^2$) derived from numerical simulation with parameters $\delta = 0.0025$, $C_1 = 0.0005$, $\nu_y = 8.7$ and $\nu_{\mathrm{m}} = 0.395$. Bottom: FFT spectrum of the second moment, where we obtain $b_0 = 3.405 \times 10^{-5}$ m^2 and $b_1 = 6.7 \times 10^{-6}$ m^2. Note that b_0 and b_1 are defined as twice of the Fourier amplitude.

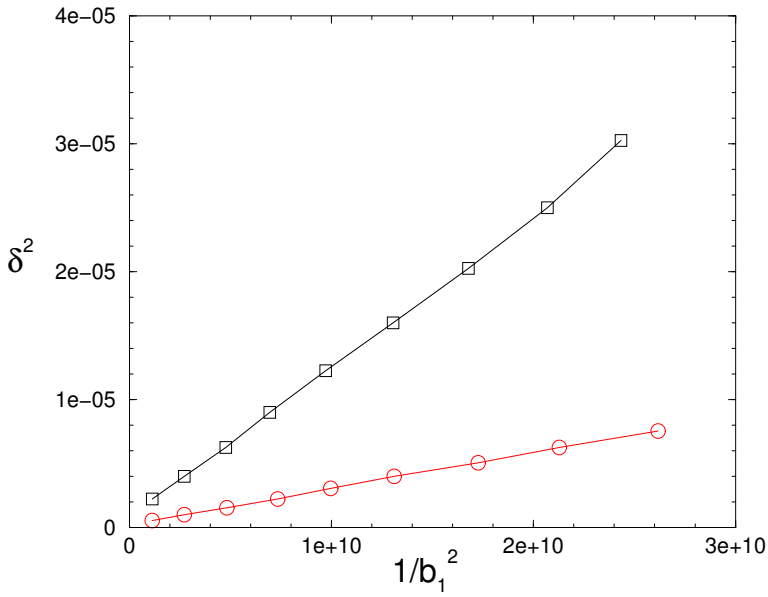

Figure 4.2: δ^2 versus $\frac{1}{b_1^2}$. $\diamond$: $C_1 = 0.001$, $\circ$: $C_1 = 0.0005$.

4.1.3 Nonlinear Hamiltonian

As we discussed in Chapter Three, the nonlinearity always exists in a real machine. Boltzmann distribution is only a first order approximation in the presence of nonlinearity, and we don't have an explicit form for the quadrupole transfer function. Fig. 4.3 shows that δ^2 vs $1/b_1^2$ derived from numerical simulations for non-zero detuning parameter follows a family of nearly linear curves. The slope is reduced even for the same initial emittance. Nevertheless, we can also derive the beam emittance and the tune of the dynamical system by using a phenomenological formula:

$$b_1 = \frac{2C_1\beta_x\epsilon_0}{\sqrt{(\delta + F\alpha_{xx}\epsilon_0)^2 - C_1^2}}, \tag{4.16}$$

where the nonlinear detuning coefficient α_{xx} can be accurately measured by using the method proposed in Ref. [17]. The derived emittance agrees well with the input emittance as shown in Fig. 4.4 with $F \approx 2.5 \pm 0.2$.

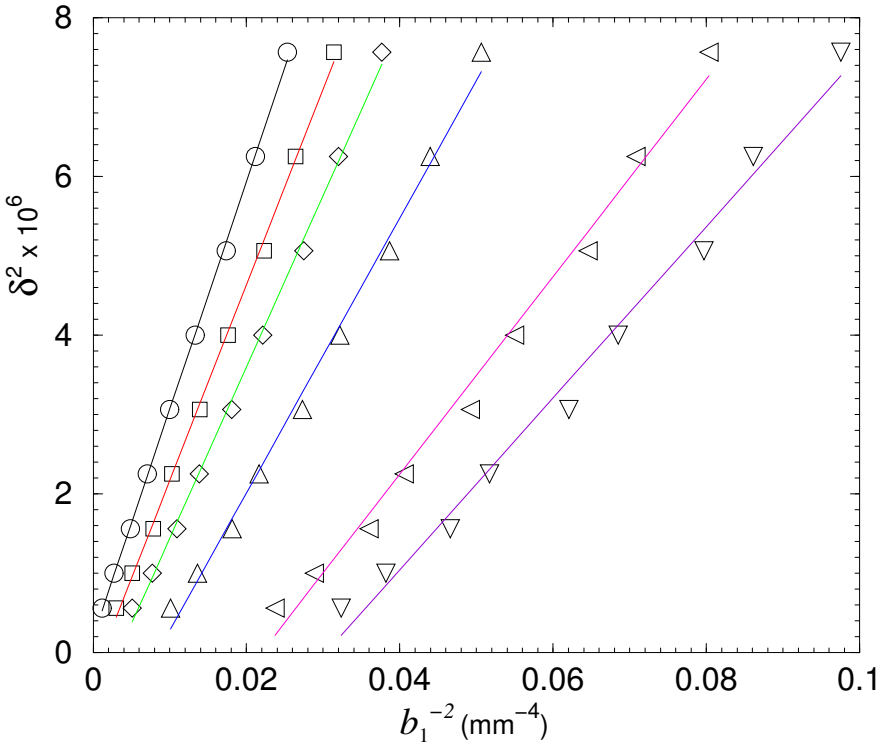

Figure 4.3: Data obtained from a Fourier analysis of numerical simulations. The parameter δ^2 is plotted as a function of $\frac{1}{b_1^2}$. The parameters are $C_1 = 0.0005$ with $\alpha_{yy} = 0, -100, -200, -400, -800$, and -1000 m^{-1} respectively in different symbols from the left-most to the right-most. The straight line is shown to guide the eyes. The data is fitted to obtain the beam emittance. The input rms beam emittance of all simulations is 1 π-mm-mrad, and the betatron amplitude function is 16.7 m.

For an actual beam-emittance measurement, the machine operation condition should be set such that it stays away from the nonlinear Mathieu bifurcation region and the procedure to measure beam emittance in a storage ring goes as follows:

1. Minimize the linear coupling, and measure the nonlinear detuning parameter

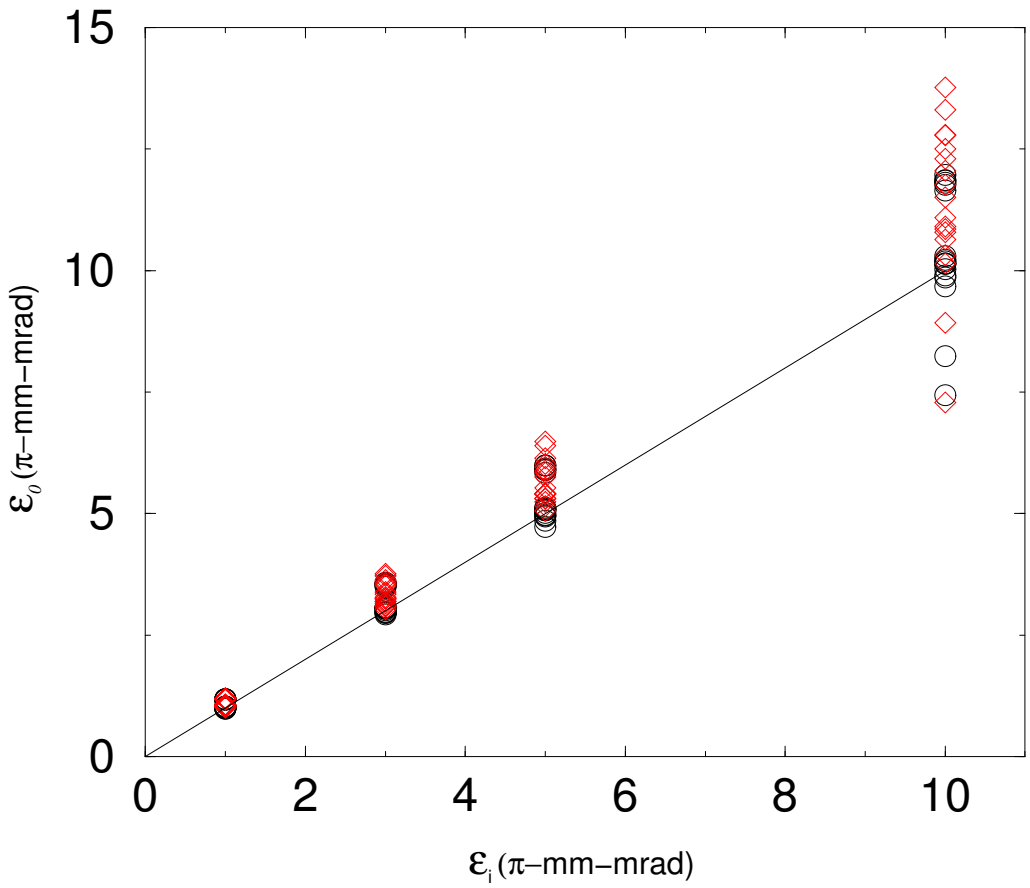

Figure 4.4: Comparison between the measured emittance (ϵ_o from numerical simulation data) and the initial input emittance (ϵ_i horizontal axis). A total of 150 sets of numerical simulation data with different machine parameters (C_1 ranging from 0.0005 to 0.005, and α_{xx} ranging from 0 to -1000 m^{-1}) and different initial beam distribution functions (Gaussian (circles) and uniform (diamonds)) are included in this plot for comparison. The spread arises essentially from the nonlinear detuning, and the strength of C_1 parameter.

α_{xx};

2. Determine the rf quadrupole strength C_1 as we discussed in Chapter Three;

3. Measure the quadrupole transfer function b_1 as a function of the modulation tune ν_{m} (or the resonance proximity parameter δ);

4. Use the measured data of b_1 vs δ to determine the emittance. The parameter C_1 depends on the strength of the rf quadrupole field and the value of the betatron amplitude function. It should not be so large as to cause large beta function perturbation.

4.2 Mismatch Compensation

The particles of the beam are distributed in phase space with width and height that are called the beam ellipse. The transportation elements are characterized by Courant-Snyder parameters. At any location they form an admittance ellipse. The beam and admittance ellipses must match to preserve emittance. Mismatch means the admittance ellipse doesn't fit the beam ellipse, and this can cause emittance dilution. Let the acceptance ellipse at the injection point of a synchrotron be

$$\gamma y^2 + 2\alpha y y' + \beta y'^2 = \epsilon_0, \tag{4.17}$$

where α, β, γ are the Courant-Snyder parameters of a synchrotron. The injection ellipse is

$$\gamma_1 y^2 + 2\alpha_1 y y' + \beta_1 y'^2 = \epsilon_0 \tag{4.18}$$

for a mis-matched injection optics, where $\alpha_1, \beta_1, \gamma_1$ are the Courant-Snyder parameters from the injection line. Transforming the injection ellipse into the normalized phase-space of the ring optics with $Y = \frac{1}{\sqrt{\beta}} y$ and $P = \frac{1}{\sqrt{\beta}}(\beta y' + \alpha y)$, we find

$$a_1 Y^2 + a_2 Y P + a_3 P^2 = \epsilon_0, \tag{4.19}$$

where $a_1 = \frac{\beta}{\beta_1} + \frac{(\alpha_1\beta-\beta_1\alpha)^2}{\beta\beta_1}$, $a_2 = 2\frac{\alpha_1\beta-\alpha\beta_1}{\beta}$, and $a_3 = \frac{\beta_1}{\beta}$. The major and minor axes of the ellipse are given by $F_+ = \sqrt{F_{\rm mm} + \sqrt{F_{\rm mm}^2 - 1}}$ and $F_- = \sqrt{F_{\rm mm} - \sqrt{F_{\rm mm}^2 - 1}}$, where the mismatch factor $F_{\rm mm}$ is

$$F_{\rm mm} = \frac{1}{2}(\gamma_1\beta + \beta_1\gamma - 2\alpha_1\alpha). \tag{4.20}$$

The mismatch-angle between the major axis and Y axis is

$$\psi_{\rm mm} = \frac{1}{2}\arctan(\frac{a_2}{a_3 - a_1}). \tag{4.21}$$

The ellipse of the mismatched injection-beam will rotate because of the betatron motion. If the betatron motion were linear, the injection ellipse would rotate forever without emittance dilution. In the presence of nonlinear detuning, the bunch will filament and fill an area of πF_+^2. The rms emittance of this diluted beam depends on the particle distribution, and the rms emittance dilution factor is approximately $F_{\rm mm}$.

4.2.1 Mismatch compensation for linear systems

Since the invariant torus is naturally elliptical when the rf quadrupole is modulating at $\nu_{\rm m} \approx |2\nu_y - n|$, the torus can be used to compensate the mismatch. In other words, the admittance ellipse can be adjusted by an rf quadrupole such that it matches the injected beam. Note that if the injected beam is off-center, additional dipole is needed to compensate the closed-orbit, *i.e.* the rf quadrupole can only modify the Courant-Snyder parameters.

To match the ellipses, we need to adjust the shape and orientation of the acceptance ellipse. When the rf quadrupole is located at the injection point, the match conditions are

$$\frac{C_1}{\delta} = \frac{F_+^2 - F_-^2}{F_+^2 + F_-^2}, \tag{4.22}$$

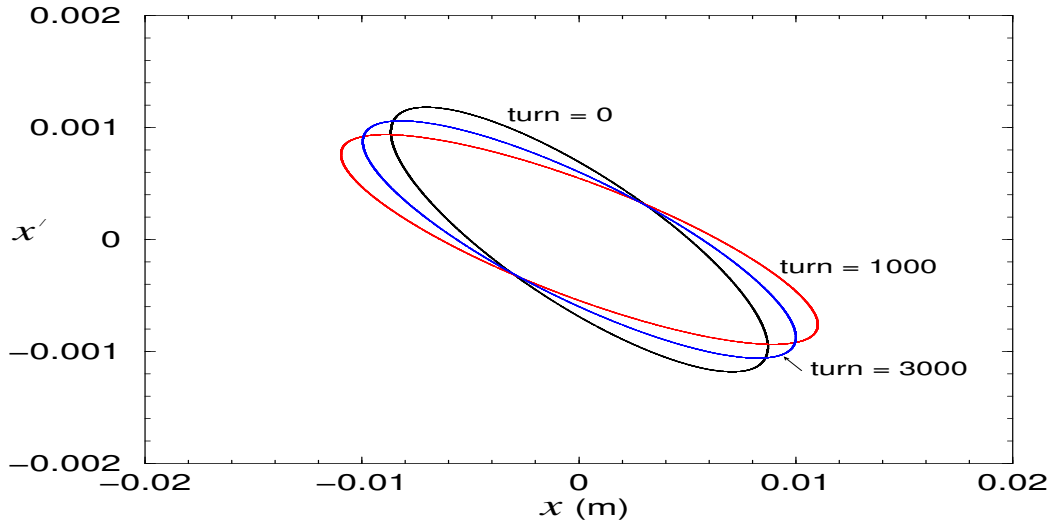

Figure 4.5: The mismatched beam ellipse with $I = I_0$ at the injection (0th turn) is captured by an rf quadrupole, and the rf quadrupole strength is adiabatically turned off to restore the matched beam condition at the 3000-th turn. The beam ellipse at the 1000-th turn is also shown for reference.

and

$$\theta_0 = \{ \begin{array}{ll} (\pi - 2\psi_{\rm mm})/\nu_m & \text{for } \delta > 0 \\ 2\psi_{\rm mm}/\nu_m & \text{for } \delta < 0 \end{array} , \tag{4.23}$$

where $\psi_{\rm mm}$, F_+, and F_- are mismatch phase and factors, and θ_0 is the rf quadrupole initial phase-angle. If the rf quadrupole is not located at the injection point, the phase difference between the rf quadrupole and the injection point should be added to or subtracted from $\psi_{\rm mm}$. After the beam injection, we can adiabatically turn off the rf quadrupole. Figure 4.5 shows the evolution of an injection ellipse in a numerical simulation where the betatron functions for the acceptance ellipse are $\alpha = 1.5$, $\beta = 16.692$ m, and $\gamma = 0.1947$ m^{-1}, and the betatron amplitude functions of the injection ellipse are $\alpha_1 = 1.4$, $\beta_1 = 12.6$ m, $\gamma_1 = 0.235$ m^{-1}. The corresponding mismatch

factors are $F_{\rm mm} = 1.08728$, $F_+ = 1.2305$, and $F_- = 0.81268$. The mismatched ellipse at the first-turn is modified by an additional rf quadrupole, where the parameters for the rf quadrupole are $\delta = 0.01$, $C_1 = 0.0038087$, and $\theta_0 = 1.05649$. The rf quadrupole is adiabatically turned off from 2000 to 3000 turns. The ellipses at injection (0th turn), at 1000-turn, and 3000-turn are shown in Fig. 4.5. The beam ellipses can be perfectly matched by an rf quadrupole in case of linear betatron motion.

4.2.2 Mismatch compensation employing nonlinear Mathieu instability island

In many accelerators, the nonlinear betatron detuning terms are un-avoidable. The method discussed in the previous section can still be applied in the parametric region (1) of Fig. 3.2. However, we can also use the nonlinear Mathieu instability island in region (3) of Fig. 3.2 to compensate mismatch. Figure 4.6 shows an example of the phase-space ellipse for a nonlinear Mathieu Hamiltonian (3.10) with parameters $\delta = 0.02$, $C_1 = 0.007464$, and $\alpha_{yy} = -100$ m^{-1}. The Hamiltonian values of these tori are $H_1 = 8.27 \times 10^{-8}$ m and $H_{\rm sfp} = 7.86 \times 10^{-7}$ m. The invariant torus rotates in the phase-space at a tune of $\nu_m/2$.

To achieve mismatch compensation, the phase-space area of an ellipse enclosed by the separatrix torus must be larger than the rms phase-space area of the injected beam, and the aspect ratio must be equal. The action I of a given torus at a constant H is

$$I = \frac{1}{\alpha_{yy}}[-(\delta + C_1 \cos 2\psi) + \sqrt{(\delta + C_1 \cos 2\psi)^2 + 2\alpha_{yy} H}] \tag{4.24}$$

for the inner island (see the left plot of Fig. 4.6). The aspect ratio of a torus is

$$\sqrt{\frac{I_{\psi=\frac{\pi}{2}}}{I_{\psi=0}}} = \sqrt{\frac{-(\delta - C_1) + \sqrt{(\delta - C_1)^2 + 2\alpha_{yy} H}}{-(\delta + C_1) + \sqrt{(\delta + C_1)^2 + 2\alpha_{yy} H}}}, \tag{4.25}$$

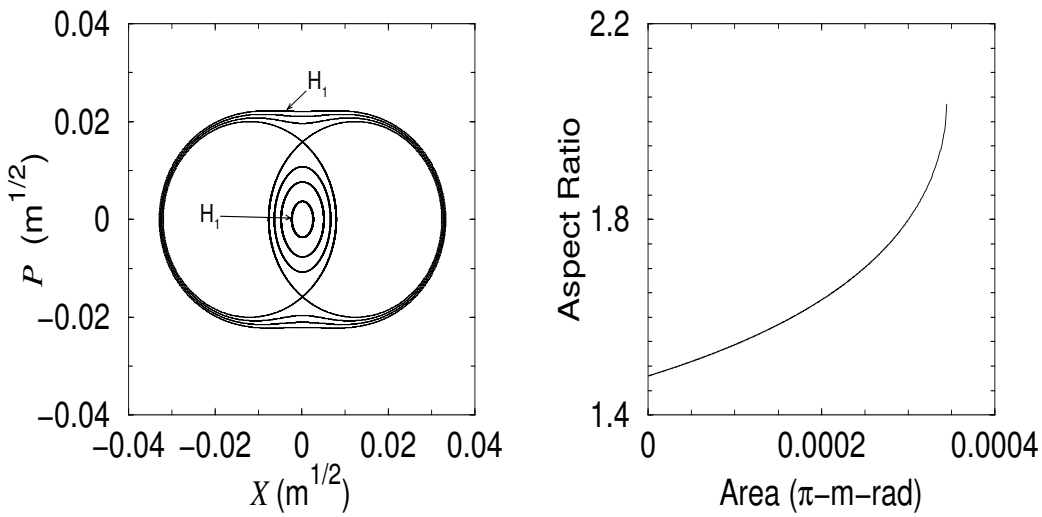

Figure 4.6: Left: The invariant tori of the nonlinear Mathieu Hamiltonian with parameters: $\delta = 0.02, C_1 = 0.007464, \alpha_{yy} = -100\ \mathrm{m}^{-1}$. Right: The ratio $\sqrt{I_{\max}/I_{\min}}$ as a function of the phase-space area of invariant tori inside the middle island.

and the phase-space area is $\oint I d\psi$. The right plot of Fig. 4.6 shows the aspect ratio as a function of the available phase area in π-m-rad. The formula for the bucket size is complicated. However, one can use the condition that the minimum action $I_{\mathrm{sx,min}}$ of the separatrix torus must be larger than $6\epsilon_0$ of the injected beam to ensure enough phase-space area for the injected beam, *i.e.*

$$I_{\mathrm{sx,min}} = -\frac{\delta}{\alpha_{yy}}\left(1 - \sqrt{\frac{C_1}{\delta}}\right)^2 > 6\epsilon_0. \tag{4.26}$$

In summary, the procedure of mismatch compensation with rf quadrupole is as follows

1. Adjust C_1/δ to shape the aspect ratio of the rms admittance torus. We choose the torus with phase space area of $\pi\epsilon_0$, and make the aspect ratio $\sqrt{I_{\max}/I_{\min}} =$

F_+/F_-;

2. Change δ/α_{yy} to provide enough bucket area for the injection beam, the criterion is Eq. 4.26;

3. Adjust the the phase of the rf quadrupole to match the orientation of the ellipses: $\theta_0 = (\pi - 2\psi_{\rm mm})/\nu_{\rm m}$.

Where $\psi_{\rm mm}$, F_+, and F_- are mismatch phase and factors. Here the π in the θ_0 matching condition arises from the fact that the major axis of the ellipse is in the $\psi = \frac{\pi}{2}$ direction.

We should note that the shape of the tori is not exactly elliptical. The aspect ratio depends on the phase-space area (see Fig. 4.6), and hence one can't fully compensate mismatch with rf quadrupole in case of non-linear detuning. In realistic applications, the ratio between the major and minor axes of a weakly mismatched injection-ellipse in normalized phase-space is close to 1, hence we can choose $|\delta| \gg |C_1|$, where the aspect ratio is close to a constant if the beam emittance is small. Although the aspect ratio increases rapidly with phase space area in Fig. 4.6, the beam actually stays in very small region close to the origin. Note the abscissa scale of Fig. 4.6 is 10^{-4}, and the beam emittance is usually $10^{-7} \sim 10^{-5}$.

Our simulations show that the final emittance can be well preserved by this simplified matching condition.

In our multi-particle simulations, we use the identical mismatch parameters as we have used in the previous section, i.e. the admittance ellipse parameters are $\alpha = 1.5, \beta = 16.692$ m, $\gamma = 0.1947$ m^{-1}, and the injection ellipse is defined by $\alpha_1 = 1.4, \beta_1 = 12.6$ m, and $\gamma_1 = 0.235$ m^{-1}. The mismatch factors are $F_{\rm mm} = 1.08728$, $F_+ = 1.2305$, and $F_- = 0.81268$. Multi-particle simulations are carried out with 10000 particles in a Gaussian distribution at an initial rms emittance of 6.0 π-mm-mrad. All particles are tracked for 3000 turns, and the rf quadrupole is adiabatically

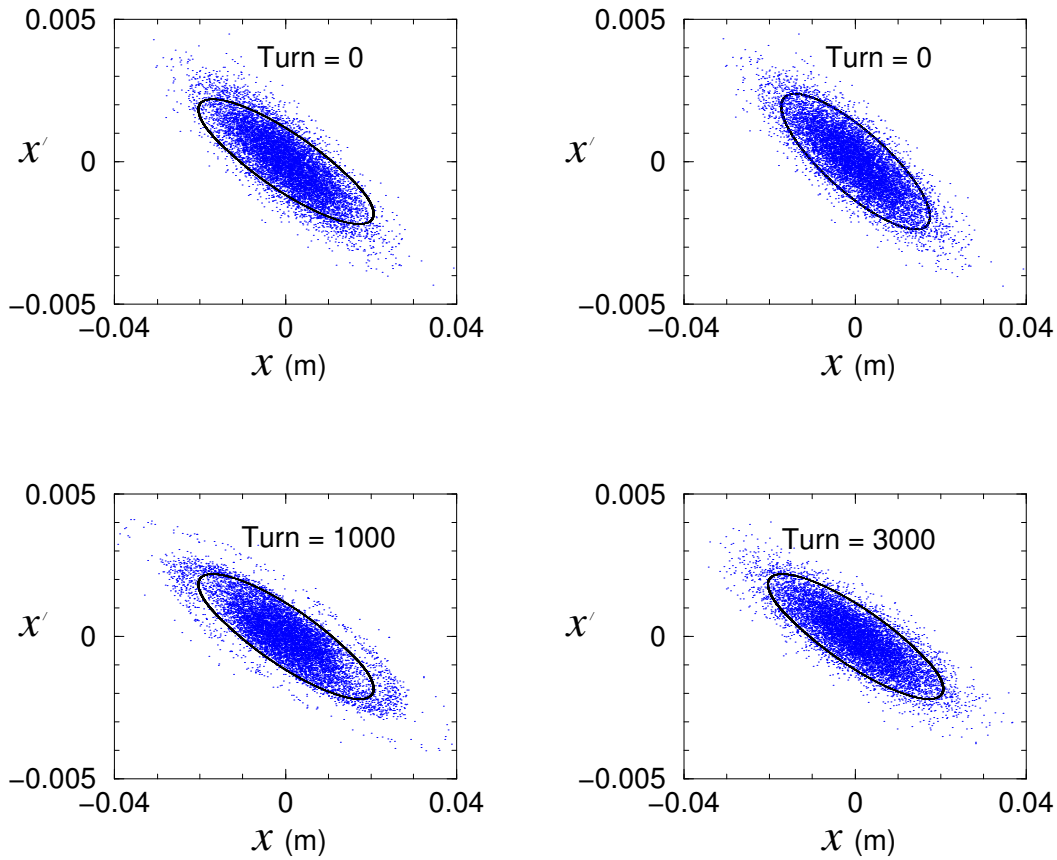

Figure 4.7: Left plots: The injected beam is mismatched at the top-left plot. Filamentation is clearly shown in the bottom-left plot at 1000-th turn for the mismatched beam. Right plots: Using nonlinear Mathieu resonance to match the injected beam shown in the top-right plot, we find that the beam emittance is preserved at 3000-th turn even in the presence of nonlinear detuning parameter. The solid lines in this graph show the 2σ admittance-ellipse.

turned off from 2001 to 3000 turns. Based on our discussion above, the parameters for the rf quadrupole and the octupole are set at $\delta = 0.02$, $\alpha_{yy} = -100$ m^{-1}, and $C_1 = 0.007464$ with a mismatch angle $\theta_0 = 1.0594$. The octupole was treated as a localized kick element, the kick is given by

$$\begin{pmatrix} y \\ y' \end{pmatrix} = \begin{pmatrix} y_0 \\ y_0' \end{pmatrix} + \begin{pmatrix} 0 \\ -r_k y_0^3 \end{pmatrix}, \tag{4.27}$$

where $r_k = \frac{8\pi}{3\beta_y^2}\alpha_{yy}$ is the kick strength parameter. The top-left plot in Fig. 4.7 shows the initial mismatched beam injected into an accelerator, where the 2σ phase-space admittance ellipse is also shown. The left-bottom plot of Fig. 4.7 shows particle distribution in the phase-space at 1000 turn, where one observes filamentation of particle distribution. If the rf quadrupole is properly implemented, the matched ellipse as shown in the top-right plot of Fig. 4.7, the resulting emittance is preserved as shown in the bottom-right plot of Fig. 4.7. The rms emittance measured at 3000 turn is about 6.48 π-mm-mrad without mismatch compensation vs 6.01 π-mm-mrad with mismatch compensation. For nonlinear Mathieu resonance islands, the invariant tori is not perfectly elliptical. A slight increase of emittance arises from mismatch compensation using nonlinear Mathieu islands arises from torus deformation. The left plot of Fig. 4.8 shows the $\sqrt{10}\,\sigma$-ellipse at injection and the filamented ellipse at 3000 turn. On the other hand, if the ellipse is mismatched in the phase coordinate, the resulting phase-space dilution will be large as shown in the right plot of Fig. 4.8 for the $1\,\sigma$-ellipse, where the initial phase mismatch is 90°. Results of numerical simulations also show that the emittance is not very sensitive to the aspect ratio, but more sensitive to the phase matching condition. Since the island tune of the Mathieu resonance island is highly nonlinear, the resulting emittance increase is limited. Clearly the mismatch compensation with nonlinear Mathieu island is not as good as that using the linear Mathieu phase-space distortion. The existence of octupole component can

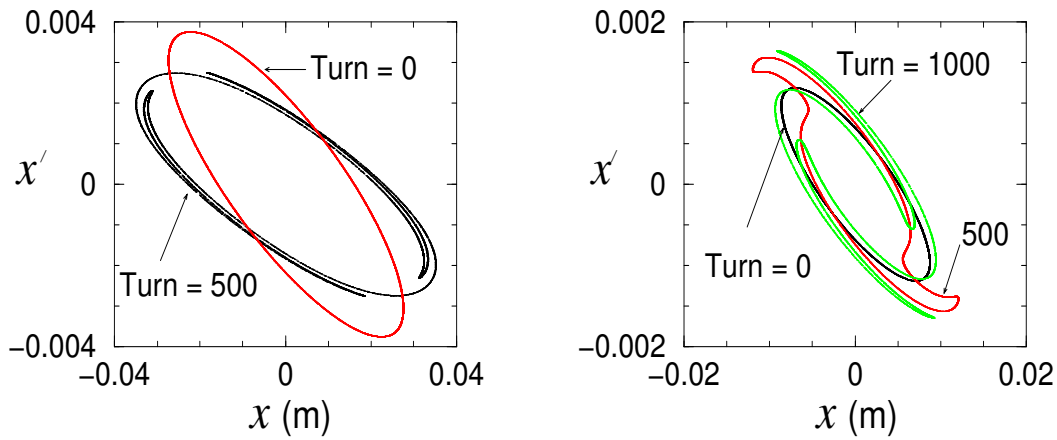

Figure 4.8: The left plot shows that the $\sqrt{10}\,\sigma$ ellipse will evolve with filamentation. The right plot shows the evolution of the 1σ ellipse with an initial phase intentionally set at $\psi = \psi_0 + \pi/2$. We observe a much larger beam filamentation. Because of the Mathieu island is highly nonlinear, the ellipse is tightly wrapped.

change the aspect ratio and limit the bucket size. Fig. 4.9 shows the aspect ratio as a function of C_1 for different nonlinear detuning parameter α_{yy}.

4.3 Overcoming spin resonances

The spin motion in electromagnetic field is governed by the Thomas-BMT equation [18, 19]

$$\frac{d\vec{S}}{dt} = \frac{e}{\gamma m}\vec{S} \times \left[(1+G\gamma)\vec{B_\perp} + (1+G)\vec{B_\parallel} + (G\gamma + \frac{\gamma}{\gamma+1})\frac{\vec{E}\times\vec{\beta}}{c}\right], \tag{4.28}$$

where $\vec{S}$ is the spin vector of a particle in the particle rest frame, $\vec{B_\perp}$ and $\vec{B_\parallel}$ are the transverse and longitudinal components of the magnetic fields in the laboratory frame with respect to $\vec{\beta}c$, the velocity of the particle, $\vec{E}$ stands for the electric field,

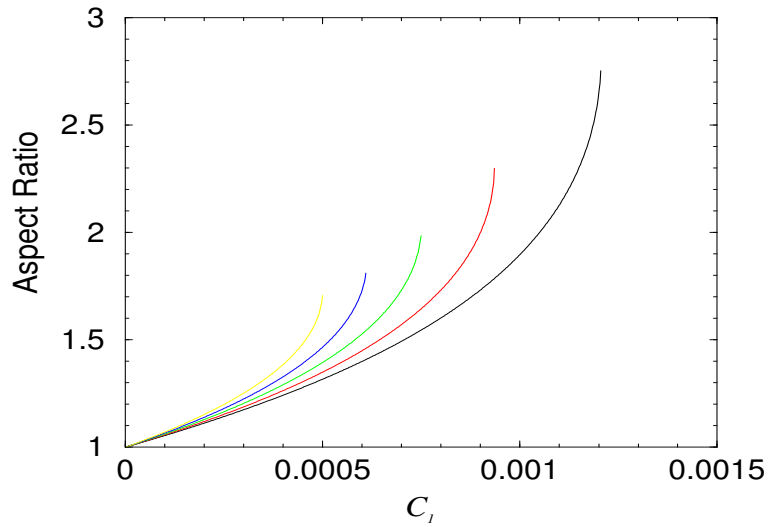

Figure 4.9: The aspect ratio changes as a function of C_1 at the point $I_{\psi=0} = 5.0 \times 10^{-7}$. $\delta = 0.002$, from the inner to the outer $\alpha_{yy} = -1000, -800, -600, -400, -200$ in sequence. The curve ends when the edge of the bucket is reached.

$G = (g-2)/2$ is the Pauli anomalous g-factor, G = 1.7928474 for protons, and γmc^2 is the energy of the particle.

In synchrotrons the dominant term in the square bracket is the first term, *i.e.*, the contribution due to the guiding dipole field dominates. Therefore the initial polarization is usually in the vertical direction. Note the spin precesses at a spin-tune of $G\gamma$, during the polarized beam acceleration, the spin-tune may sweep through many spin depolarizing resonances. There are two kinds of spin resonances, imperfection and intrinsic. Imperfection resonance stems from a distorted closed orbit, on which the horizontal magnetic field is not zero. Therefore particles receive a kick every revolution. The resonance happens when $G\gamma$ is an integer. Intrinsic resonances are driven by the horizontal magnetic field arising from the beam betatron motion. The

resonance condition is $G\gamma = kP + \nu_z$, where k is integer, P is the super-period number, ν_z is the vertical tune. The imperfection resonance can be overcome by a spin-flipping snake[21]. The Tune jump method can be used to avoid intrinsic spin resonance[20], however, the novel rf dipole method turned out to be more feasible. The idea is to generate a coherent dipole motion and induce spin flip to most particles in the beam thus preserving the polarization[2]. Unfortunately, the coherent dipole excitation produces two nearly overlapping spin-resonances, *i.e.* the intrinsic spin resonance, and the induced spin resonance. Since an rf quadrupole can also induce coherent quadrupole mode oscillation, it would be interesting to examine the capability of the rf quadrupole on the spin-resonance compensation.

To overcome spin resonance, we work with the nonlinear Mathieu instability shown in Fig. 3.2. As described in Ch. 3, the beam is moved slowly to avoid unnecessary emittance dilution. In region 2, the stable fixed point bifurcates into two stable fixed points. In this region, the unstable fixed point is located at $I_{\rm ufp} = 0$. Because all particles execute coherent betatron quadrupole-mode oscillations, the beam polarization can be maintained after passing through the spin resonance.

If we assume that the beam distribution around two stable fixed points of the Mathieu instability region is Gaussian, the spin flipping rate is given by the ensemble average of beam distribution with the Froissart-Stora formula, *i.e.*,

$$\frac{P_f}{P_i} = \frac{2}{1+\pi\kappa^2/\alpha} \exp\left\{ -\frac{I_{\rm sfp}}{\epsilon_0} \cdot \frac{\pi\kappa^2/\alpha}{1+\pi\kappa^2/\alpha} \right\} - 1, \tag{4.29}$$

where $I_{\rm sfp}$ is action at stable fixed point, κ is the spin resonance strength for a particle with rms action $\frac{1}{2}\epsilon_0$, and $\alpha = \frac{d(G\gamma)}{d\theta}$ is the acceleration rate.

Using the AGS parameter as our working example, the spin flipping rate is shown in Table 4.1, where we use the parameters: $\alpha_{yy} = -200\ \mathrm{m}^{-1}$, $C_1 = 0.01$, $\delta = -0.00626$ and $\epsilon_0 = 1.66\ \pi$-mm-mrad for the AGS beam to obtain $I_{\rm sfp} = 18.7$ mm-mrad. The polarized beam acceleration rate is $\alpha = 4.86 \times 10^{-5}$. We can also calculate the

polarization by carrying out an ensemble average of the beam distribution. These two results are compared in the third and the fourth column of Table 4.1. Note that the polarization based on a Gaussian distribution slightly overestimates the final polarization value.

Table 4.1: Polarization rate for AGS

$nP \pm \nu_z$	κ	$\mathrm{Pol_f}/\mathrm{Pol_i}$	
		Gaussian	Simulation
8.7	0.0061	-0.878	-0.765
27.3	0.0051	-0.796	-0.657
44.7	0.011	-0.981	-0.940

Chapter 5

RF Voltage Modulation

5.1 Voltage Modulation and Bunch Compression

The circulating beam in accelerators passes through the rf cavity each turn. The beam is focused by the rf cavity if $\phi_s = 0$. When the synchronous phase is not zero, the total beam also gains energy from the rf cavity. The RF voltage might not be stable. It is affected by rf noise, power supply ripple, wake fields, etc. If the perturbation happens to be on resonance with the longitudinal motion of the particle, then the particle will be lost. In other words, the average effect of the perturbation is trivial unless it is close to the harmonics of the longitudinal oscillation frequency.

The first harmonic oscillation can be externally exerted on the beam by rf phase modulation [23]. Rf phase modulation is equivalent to dipole mode perturbation when the modulation frequency is close to the longitudinal oscillation frequency. The arrival time of the bunch will oscillate at the modulation frequency. Due to the nonlinearity, this oscillation will normally decohere in seconds at the cost of emittance dilution. Recently interesting phenomenon has been found in Tevatron at Fermi Lab [24]. The bunch oscillates at longitudinal oscillation frequency for hours without deteriorating

the beam quality. This oscillation might be one reason which impedes the intensity-improving project [25]. Although these phenomena are thought to be well understood they can be complicated in practice.

Quadrupole mode oscillation in longitudinal phase space can be excited by modulating the RF voltage near twice the synchrotron frequency [26]. Early research was focused on the nonlinear properties and the confirmation of the Hamiltonian theory. However, when quadrupole mode oscillation is excited, the moments of the beam will oscillate, namely, the bunch length will oscillate while the emittance is preserved. This can be used to compress the bunch. Short proton bunches are needed in the generation of the secondary beam. The experiment of proton bunch compression with voltage modulation has been done at the AGS [27]. Unfortunately they didn't find a way to compress the bunch.

Short electron bunches are needed in both current and future projects, like the FEL project and the linear collider project [28, 29]. The gain length of the undulator in an FEL facility is reciprocal to $I^{1/3}$, where I is the peak current of the bunch. Therefore shorter bunches result in higher power gain. The Same consideration is found in the design of linear colliders. Higher frequency is preferred to obtain higher energy gain on unit length, which requires shorter injected bunches. Currently a bunch compressor downstream to the damping ring is the common solution.

The equilibrium bunch length in an electron storage ring is determined by the aspect ratio of the ellipse-like tori of the longitudinal Hamiltonian. The aspect ratio is related to the machine parameters, *i.e.*, the voltage and the harmonic number of the RF system, the phase slip factor, the synchronous phase and the energy of the electron. In some cases the phase slip factor can be reduced by adjusting the sextupoles in the ring [30], however, to maintain a stable operation, these parameters are usually fixed, consequently the output bunch length is also determined.

The bunch can be compressed in the storage rings through beam manipulations.

RF voltage and phase jump methods were explored at the IUCF proton storage ring [31]. The aspect ratio, $\frac{\sigma_\phi}{\sigma_\delta}$, is proportional to $\frac{1}{\sqrt{V_{rf}}}$. Therefore if the initial cavity voltage is V_1 and the final is V_2, and the emittance is preserved during this process, then the bunch is compressed by a factor of $(\frac{V_2}{V_1})^{1/4}$. For electron machines the synchronous phases have to be counted too. But usually the voltage of the RF system can not be raised much, hence the compressing ratio of this method is limited. The phase jump method moves the bunch to the unstable fixed point. The trajectories around the unstable point are hyperbolic, and the bunch expands in (ϕ, δ) phase space in $\pi/4$ and $5\pi/4$ direction and shrinks in the perpendicular direction. The compressed bunch can be accepted after a rotation of $\pi/4$. But the nonlinearity will distort the bunch when the particle is moved off the unstable fixed point, thus the emittance is not preserved in this process. Also this method is not good for electron storage rings because quantum fluctuations can cause serious emittance increase.

In this chapter we are going to discuss the beam dynamics under voltage modulation, then apply it to electron bunch compression. The difference between proton bunch compression and electron bunch compression will be also be addressed.

5.2 The Hamilton Dynamics with Voltage Modulation

The synchrotron motion in a storage ring with voltage modulation can be described by

$$\begin{cases} \phi_{n+1} &= \phi_n + 2\pi h\eta\delta_n \\ \delta_{n+1} &= \delta_n + f(\phi_{n+1}) - f(\phi_s) \end{cases}, \tag{5.1}$$

where $f(\phi_n) = \frac{eV_0}{\beta^2 E}(1+b\sin(\nu_m((\phi_n-\phi_s)/h+2n\pi)+\chi))\sin\phi_n$, ϕ_s is the synchronous phase, η is the phase slip factor, and V_0 and h are the voltage and harmonic number

of the RF system respectively. The parameters related to the particle are: β, the ratio of the particle speed to the speed of light, e, the unit charge, and E, the energy of the particle. The modulation parameters are: the fractional modulation strength b, the modulation tune ν_m, and the initial phase angle χ. Note the phase of the modulation signal is related to the phase of the particle. Since $(\phi_n - \phi_s)/h$ is much less than $2n\pi$ when n is large, this term can be ignored.

Eq. (5.1) can be derived from the following Hamiltonian

$$H = \frac{1}{2}h\eta\delta^2 + \frac{eV_0}{2\pi\beta^2 E}(1 + b\sin(\nu_m\theta + \chi))[\cos\phi - \cos\phi_s + (\phi - \phi_s)\sin\phi_s], \quad (5.2)$$

with orbital angle $\theta = 2n\pi$ as the time variable. Let $\Phi = \phi - \phi_s$ and expanding the Hamiltonian into a Taylor series, one obtains

$$H = \frac{1}{2}h\eta\delta^2 - \frac{eV_0\cos\phi_s}{2\pi\beta^2 E}(1 + b\sin(\nu_m\theta + \chi))\frac{1}{2}\Phi^2(1 - \frac{\tan\phi_s}{3}\Phi - \frac{\Phi^2}{12} + \dots). \quad (5.3)$$

Without loss of generality, we assume the phase slip factor $\eta > 0$, or $\cos\phi_s < 0$. Transforming to the action angle coordinates (J, ψ) with

$$\begin{cases} \Phi &= \sqrt{2h\eta J/\nu_s}\cos\psi \\ \delta &= -\sqrt{2\nu_s J/h\eta}\sin\psi \end{cases}, \quad (5.4)$$

where $\nu_s = \sqrt{-\frac{h\eta eV_0\cos\phi_s}{2\pi\beta^2 E}}$ is the tune for synchronous particle, one gets $H = H_0 + H_1$, where

$$H_0 = \nu_s J - \frac{\sqrt{2h\eta\nu_s}}{3}\tan\phi_s J^{3/2}\cos^3\psi - \frac{h\eta}{6}J^2\cos^4\psi + \dots, \quad (5.5)$$

and

$$H_1 = b\nu_s J\cos^2\psi\sin(\nu_m\theta + \chi)(1 - \frac{1}{3}\sqrt{\frac{2h\eta J}{\nu_s}}\tan\phi_s\cos\psi - \frac{1}{6}\frac{h\eta J}{\nu_s}\cos^2\psi + \dots). \quad (5.6)$$

Using the generating function

$$F_2(\psi, \tilde{I}) = \psi\tilde{I} + \frac{\sqrt{2h\eta}}{36\sqrt{\nu_s}}\tan\phi_s\tilde{I}^{3/2}\sin 3\psi + \frac{\sqrt{2h\eta}}{4\sqrt{\nu_s}}\tan\phi_s\tilde{I}^{3/2}\sin\psi \quad (5.7)$$

the unperturbed Hamiltonian H_0 is transformed to

$$H_0 = \nu_s \tilde{I} - \frac{h\eta}{6}\tilde{I}^2 \cos^4\psi - \frac{h\eta}{3}\tan^2\phi_s \tilde{I}^2 \cos^6\psi. \tag{5.8}$$

The average H_0 is

$$\langle H_0 \rangle = \nu_s \tilde{I} - \frac{h\eta}{16}(1 + \frac{5}{3}\tan^2\phi_s)\tilde{I}^2. \tag{5.9}$$

And the perturbation Hamiltonian H_1 at $\nu_m \approx 2\nu_s$ is given by

$$H_1 = -\frac{1}{4} b\nu_s \tilde{I} \sin(2\psi - \nu_m\theta - \chi). \tag{5.10}$$

Where $O(\tilde{I}^2)$ of H_0 and non-resonance terms of H_1 have been ignored.

Transforming the Hamiltonian $\langle H_0 \rangle + H_1$ into the resonance rotating frame with the generating function

$$F_2(\psi, I) = (\psi - \frac{\nu_m}{2}\theta - \frac{1}{2}\chi + \frac{\pi}{4})I, \tag{5.11}$$

the new Hamiltonian takes the following form

$$\bar{H} = \Delta I - \frac{1}{2}\alpha I^2 + CI\cos 2\Psi, \tag{5.12}$$

where (I, Ψ) are conjugate phase-space coordinates, the resonance proximity parameter Δ, nonlinear detuning parameter α, and the resonance strength C are given by

$$\Delta = \nu_s - \frac{\nu_m}{2}, \tag{5.13}$$

$$\alpha = \frac{h\eta}{8}(1 + \frac{5}{3}\tan^2\phi_s), \tag{5.14}$$

$$C = \frac{1}{4} b\nu_s. \tag{5.15}$$

The stable fixed points(SFP) are

$$I_{SFP} = \begin{cases} \frac{\Delta + C}{\alpha} & \text{if} \quad \nu_m < \nu_{\text{bif+}} \\ 0 & \text{if} \quad \nu_m < \nu_{\text{bif-}} \text{ or } \nu_m > \nu_{\text{bif+}} \end{cases}, \tag{5.16}$$

where $\nu_{\text{bif+}} = \nu_s(2 + \frac{1}{2}b)$, $\nu_{\text{bif-}} = \nu_s(2 - \frac{1}{2}b)$. The unstable fixed points(UFP) are given by

$$I_{UFP} = \begin{cases} \frac{\Delta - C}{\alpha} & \text{if} \quad \nu_m < \nu_{\text{bif-}} \\ 0 & \text{if} \quad \nu_{\text{bif+}} > \nu_m > \nu_{\text{bif-}} \end{cases} . \tag{5.17}$$

All the physics are the same as we have discussed in the previous chapters now that we have an identical form of the Hamiltonian. The only difference is, here the unperturbed Hamiltonian is on average, hence the particle should move around the torus of the Hamiltonian. Fig. 5.1 shows the tori of the Hamiltonian and the real traces of particles under different conditions.

5.3 Bunch Compression Parameters

We use the one stable fixed point side to compress the bunch, *i.e.*, make the modulation tune $\nu_m > \nu_{\text{bif+}}$. As we demonstrated in Chapter Three, the aspect ratio is a function of action I, or the Hamiltonian H. The aspect ratio of a particular torus is given by

$$r_b = \sqrt{\frac{-\Delta - C + \sqrt{(\Delta + C)^2 - 2\alpha\bar{H}}}{-\Delta + C + \sqrt{(\Delta - C)^2 - 2\alpha\bar{H}}}}. \tag{5.18}$$

The average aspect ratio is calculated by

$$\langle r_b \rangle = \sqrt{\frac{\langle 2I\cos^2\Psi \rangle}{\langle 2I\sin^2\Psi \rangle}}, \tag{5.19}$$

where, for example, $\langle 2I\cos^2\Psi \rangle = \int_0^{2\pi} d\Psi \int_0^{\infty} dI 2I\cos^2\Psi\rho(I,\Psi)$, and $\rho(I,\Psi)$ is the Boltzmann distribution. The analytic solution of $\langle r_b \rangle$ is difficult to obtain; however, it can be approximated by the aspect ratio of the torus which has area of $\pi\epsilon_0$, with ϵ_0 as the emittance of the beam.

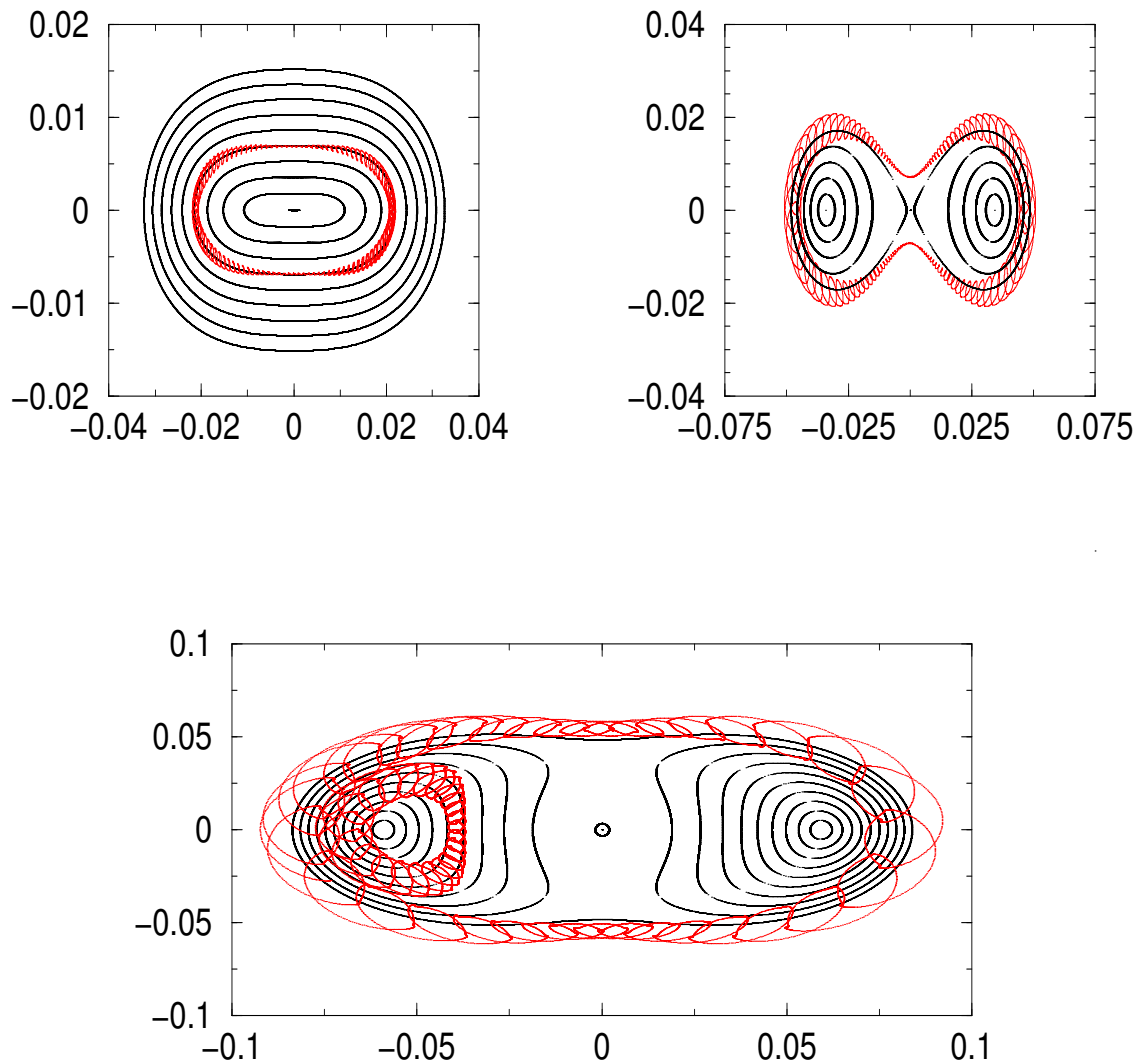

Figure 5.1: The tori of the voltage modulation Hamiltonian and the real trace of particles. The parameters are $\alpha = 0.07528$, $C = 4.41 \times 10^{-5}, b = 0.05$, Δ is different for each graph: up left: $\Delta = -1.005C$, up right: $\Delta = 0$, down: $\Delta = 2.0C$. Traces of two particles are plotted in the down graph.

The tori rotate at a tune of $\nu_m/2$ in the lab frame, therefore the bunch length

oscillates according to

$$\sigma_\phi^2 = \frac{h\eta}{2\nu_s}\frac{\epsilon_0}{\langle r_b\rangle}[\langle r_b\rangle^2 + 1 + (\langle r_b\rangle^2 - 1)\sin(\nu_m\theta + \chi)], \tag{5.20}$$

where $\theta = 2\pi n$ is the orbital angle starting from the first modulation turn. The modulation has to be turned on adiabatically to preserve the emittance. Assume the bunch is extracted N turns after the modulation, the initial phase which makes the bunch minimum on extraction is given by

$$\chi = \pi(\frac{3}{2} - 2N\nu_m). \tag{5.21}$$

Then the bunch is compressed by a factor of $\sqrt{\langle r_b\rangle}$. Fig. 5.2 is the plot of $\langle r_b\rangle$ as $\nu_m \to \nu_{\text{bif+}}$. Theoretically $\langle r_b\rangle$ goes to infinity; however, in particle simulation it saturates at a value of $4 \sim 8$ depending on the emittance. Note this compression ratio is independent of machine parameters, which means the bunch can only be compressed by $2 \sim 3$ times through this method. This is easy to understand because $\nu_{\text{bif+}}$ is the bifurcation point.

5.3.1 Bunch Compression in Electron Storage Rings

Damping and quantum fluctuation must be included for electron storage rings because the damping time is of the same order as the voltage modulation period. According to the Central Limit Theorem, the quantum fluctuation is just a Gaussian distributed noise. The deviation of the noise is related to the machine parameters. The damping and quantum fluctuation term can be included into mapping equations as follows

$$\begin{cases} \phi_{n+1} &= \phi_n + 2\pi h\eta\delta_n \\ \delta_{n+1} &= \delta_n + \frac{eV_0}{\beta^2 E}(1 + b\sin(\nu_m\theta + \chi))(\sin\phi_{n+1} - \sin\phi_s) - \frac{4\pi}{\omega_0\tau_E}\delta_n + \xi_n \end{cases}, \tag{5.22}$$

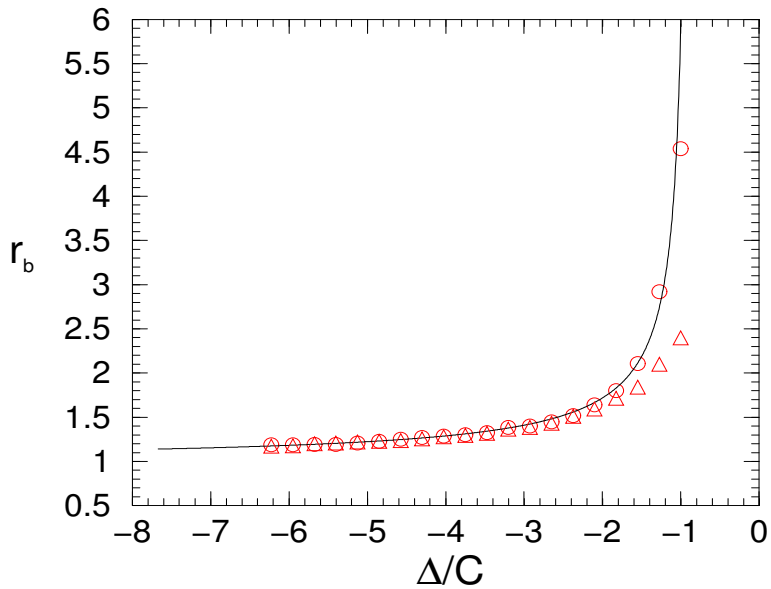

Figure 5.2: The aspect ratio changes as Δ goes to $-C$. The parameters used are: $b = 0.1$, $C = 8.82 \times 10^{-5}$, $\nu_s = 0.003529$, $\alpha = 0.07528256$, $\epsilon_0 = 5.0 \times 10^{-5}$. The circles and triangles are the aspect ratios obtained from particle simulation, and the curve is the aspect ratio of the torus with the area of $\pi\epsilon_0$. $\langle r_b \rangle$ saturates at 4.54 for this set of parameters. The triangles are for the simulation with quantum fluctuation and damping, but they are set to zero for those circles. The emittance is preserved provided $\nu_s > \nu_{bif+}$.

where τ_E is the longitudinal damping time and ξ_n is the quantum excitation term, which is generated by a Gaussian distribution noise with deviation [33]

$$\sigma_\xi = \frac{2}{\sqrt{f_0 \tau_E}} \sqrt{\frac{C_q \gamma^2 I_3}{2I_2 + I_4}} = \sqrt{C_\xi E^3 \gamma^2 I_3} \tag{5.23}$$

where $C_q = 3.83 \times 10^{-13} m$, $C_\xi = 1.079 \times 10^{-18} m^2/(GeV)^3$, f_0 is the revolution frequency, E is the energy in GeV, τ_E is the longitudinal damping time, γ is the

relativistic energy factor and I_n $(n = 2, 3, 4)$ are the radiation integrals along the machine.

Take the Next Linear Collider Main Damping Ring as an example. The related parameters are listed in table 5.1. Fig. 5.3 shows the damping process of NL-

Table 5.1: Parameters for Next Linear Collider Main Damping Ring [29]

C	E	ν_s	$\sigma_{\delta e}$	$\sigma_{\phi e}$	τ_E	U_{sr}	η	V_{RF}	f	σ_ξ
m	GeV		%	Radian	ms	kV/turn	$(\times 10^{-4})$	MV	MHz	$(\times 10^{-5})$
299.792	1.98	0.0035	0.091	0.054	2.6	777	2.95	1.07	714	3.56

CMDR. The bunch length, momentum spread and emittance decrease exponentially and reach equilibrium after 7ms. The equilibrium particle distribution is Gaussian, and the deviations are exactly the nominal values. The results indicate the quantum fluctuation term in Eq. 5.22 is correct. The left plot of Fig. 5.4 shows the bunch length oscillation while the modulation ramps up. The amplitude of the oscillation is damped compared to that without damping and quantum fluctuation. The right plot shows the emittance versus turn during the same process. The emittance increase is very small when damping and quantum fluctuation are set to zero, however, there is ten percent increase when they are included. Overall the voltage modulation offers a new method to compress the bunch. Proton bunch can be compressed by 2∼3 times without significant emittance increase. However, the electron bunch can only be compressed by 1∼2 times due to the radiation damping. There is also a slight emittance increase due to the quantum fluctuation. This method is not so effective in compressing the bunch.

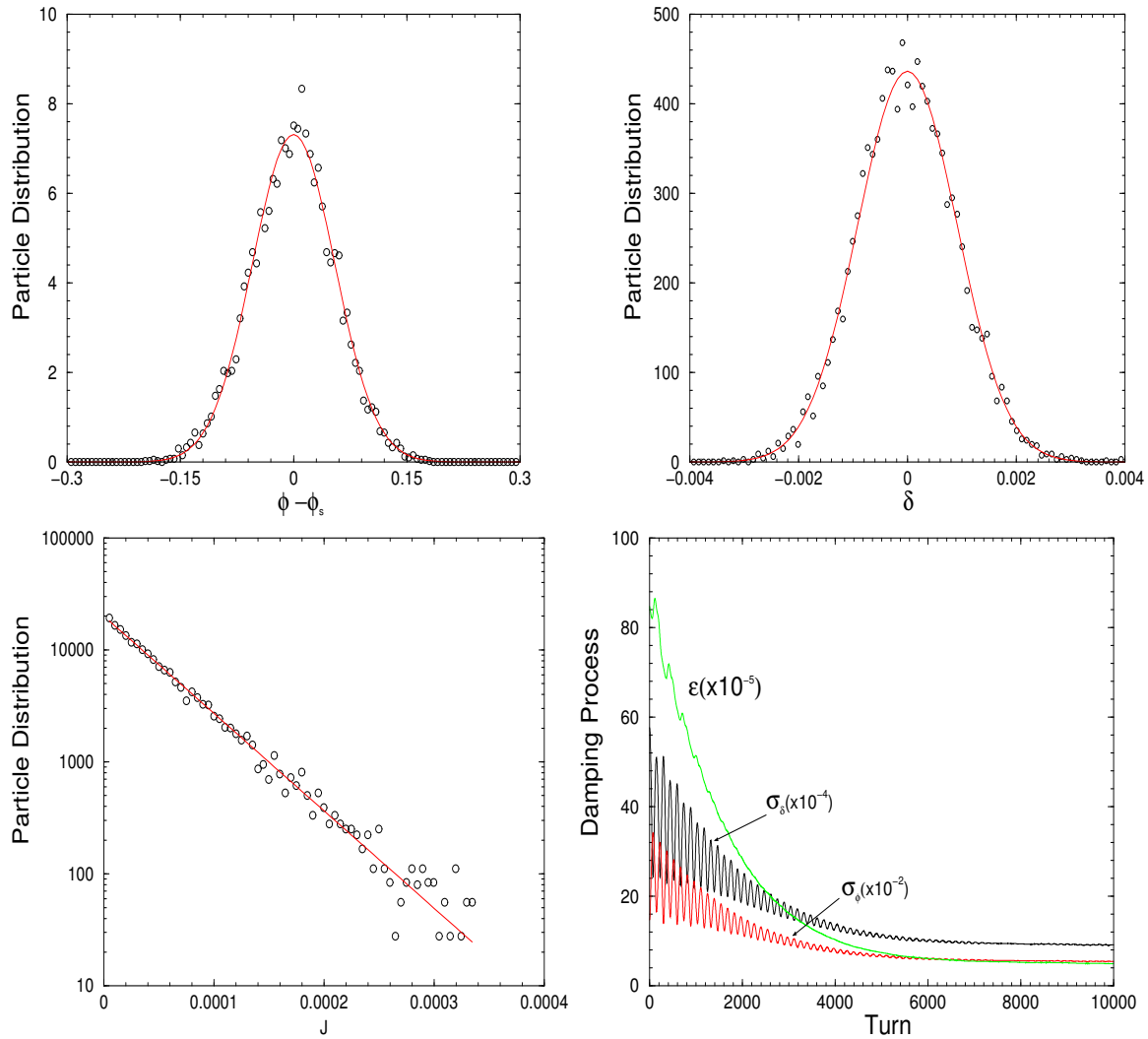

Figure 5.3: In all plots, circles are obtained from particle simulation, solid line is Gaussian distribution with the nominal deviation. Upper left: Particle distribution along $\phi - \phi_s$ direction,$\sigma_\phi = 0.053$ Radian. Upper right: Particle distribution along δ direction, $\sigma_\delta = 0.091\%$. Lower left: Particle distribution along the action J, the Gaussian distribution is given by $\rho(J) = \frac{1}{\epsilon_0} e^{-J/\epsilon_0}$. Lower right: The longitudinal damping process of NLCMDR in the first 10ms after injection. The injection parameters are $\sigma_\phi = 0.15$, $\sigma_\delta = 0.5\%$, the nominal equilibrium parameters are $\sigma_\phi = 0.053$ and $\sigma_\delta = 0.091\%$.

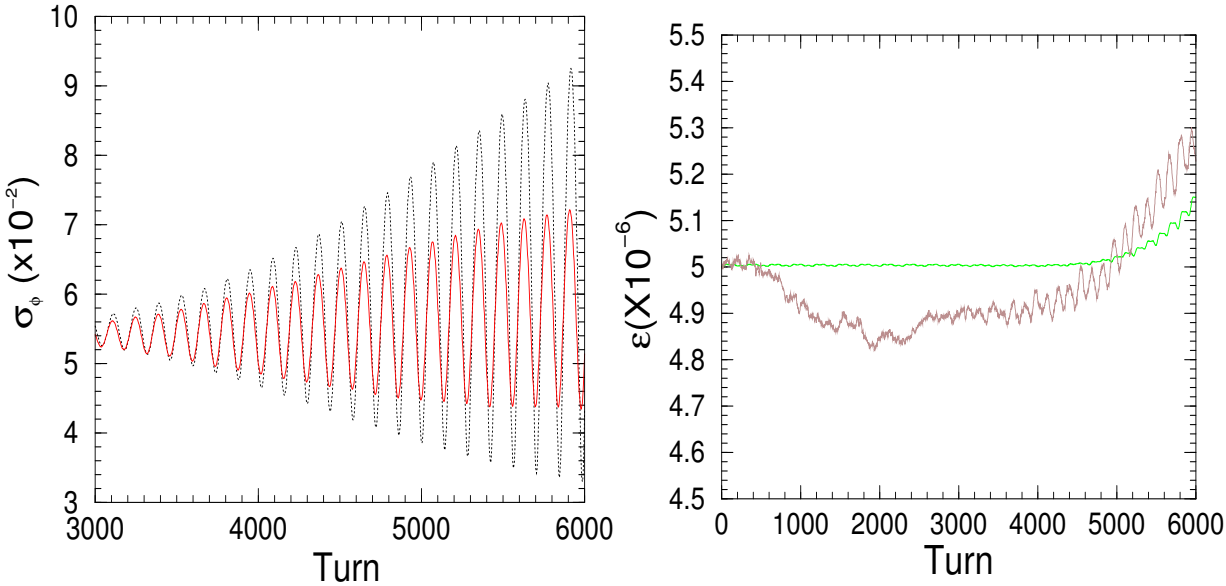

Figure 5.4: Bunch length and emittance changes while the voltage modulation strength ramps up. The strength increases adiabatically from turn 1,000 to turn 6,000. The solid line has damping and quantum fluctuation on and the dotted line doesn't. Parameters are $b = 0.05, \alpha = 0.07528$, $\Delta = -1.05 \times C$, $C = 4.41 \times 10^{-5}$. Left: Bunch length oscillation. At the minimum bunch length point, $\sigma_\phi = 0.0435, 0.0330$ and $\sigma_\delta = 1.21 \times 10^{-3}, 1.56 \times 10^{-3}$ respectively. Right: The change of emittance. In the presence of damping and quantum fluctuation, the equilibrium emittance is 4.82×10^{-5}. The emittance increases about ten percent when damping and quantum fluctuation are included, but very little when they are set to zero.

Chapter 6

Using Double RF Cavities to Compress the Bunch

6.1 Introduction

Using a second harmonic RF system to lengthen the bunches and improve the beam lifetime was first proposed by A. Hofmann and S. Myers in 1980 [34]. First we briefly review the method. Assume the combined voltage of two rf systems is

$$V(\phi) = V_0[\sin\phi + r\sin(m\phi + \phi_r)], \tag{6.1}$$

where r is the relative strength of the second rf system, m is the harmonic number and ϕ_r the initial relative phase angle. Let r and ϕ_r satisfy the following equations

$$\frac{dv(\phi)}{d\phi}|_{\phi=\phi_s} = 0, \quad \text{and } \frac{d^2v(\phi)}{d\phi^2}|_{\phi=\phi_s} = 0. \tag{6.2}$$

Therefore

$$r = \frac{\sqrt{m^2\cos^2\phi_s + \sin^2\phi_s}}{m^2}, \tag{6.3}$$

$$\phi_r = -m\phi_s - \arcsin\frac{\sin\phi_s}{m^2 r}. \tag{6.4}$$

Note ϕ_s must be re-calculated because the second rf system also contributes to the total voltage at phase ϕ_s.

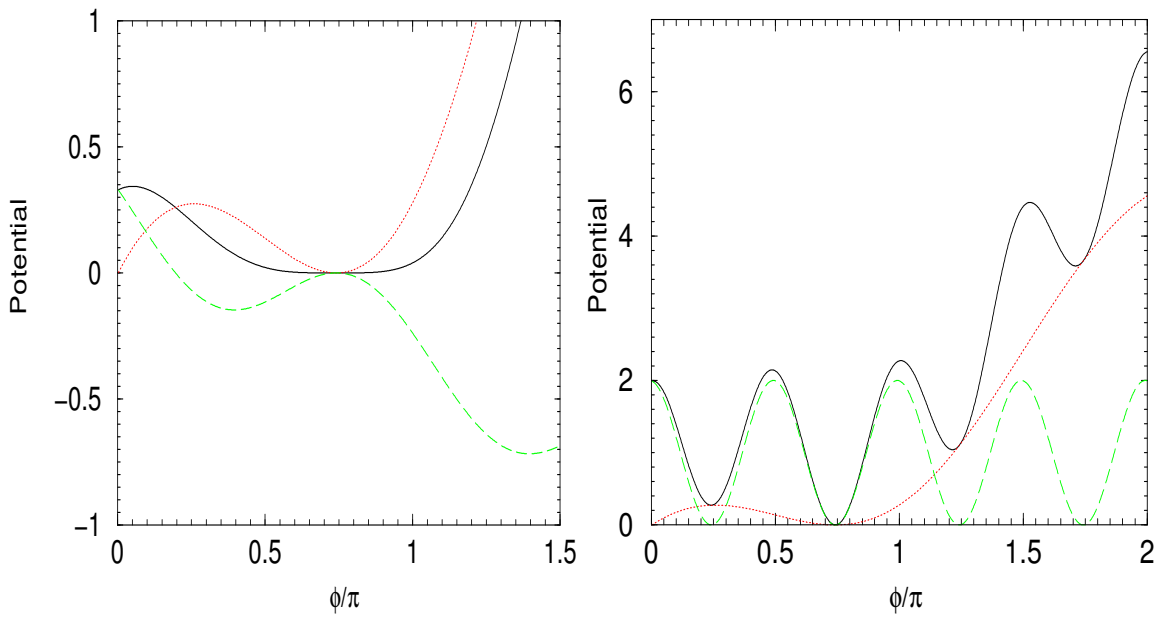

Figure 6.1: The potential change due to the second harmonic cavity. The dotted line is the original potential $V_o(\phi) = \cos\phi - \cos\phi_s + (\phi - \phi_s)\sin\phi_s$. The long dashed line is the potential due to the second rf system, $V_2(\phi) = \frac{r}{m}(\cos(m\phi+\phi_r) - \cos(m\phi_s+\phi_r)) + (\phi-\phi_s) r \sin(m\phi_s+\phi_r)$. The bold line is the combined potential $V_c(\phi) = V_o(\phi) + V_2(\phi)$. The left plot is for bunch lengthening, the parameters are $\phi_s = 2.3288$ Radian, $\phi_r = -5.1436$ Radian, $r = 0.38875$, $m = 2$. The right plot is for bunch compression, and $\phi_s = 2.3288$ Radian, $\phi_r = -m\phi_s - \pi$, $r = 4$, $m = 4$.

Fig. 6.1 has plots of the potentials for one and two rf systems. One can see that the bottom of the potential is flattened by the second rf voltage. We tested this idea by particle simulation and it works well. For the NLC the bunch length is increased

by about 4 times with the parameters listed in the caption of Fig. 6.1. Harmonic RF systems have recently been installed and commissioned on several light sources [35], but with various lifetime improvement reported.

Note if we change the phase of the second voltage, the bottom of the total potential is going to be narrower, which results in shorter bunches. This is the idea of this chapter.

6.2 Beam Dynamics with a Second RF System

In order to compress the bunch, one wishes to maximize $|\frac{dV(\phi)}{d\phi}|_{\phi_s}|$. This leads to $\phi_r = -m\phi_s - \pi$. Without loss of generality we have assumed the phase slip factor $\eta > 0$, or $\cos\phi_s < 0$. The potential of two RF system for bunch compression is also plotted in Fig. 6.1.

The synchrotron motion of particle in a storage ring with double RF system can be described by

$$\phi' = h\eta\delta, \delta' = \frac{eV_0}{2\pi\beta^2 E}(\sin\phi - \sin\phi_s + r\sin(m\phi - m\phi_s - \pi)), \tag{6.5}$$

where the prime indicates first derivative with respect to the orbital angle θ, h is the harmonic number of the main RF system, β the fractional speed of the speed of light, e the unit charge, and E the energy of the particle. Small oscillation around the synchronous phase is given by

$$A'' = \frac{h\eta eV_0\cos\phi_s}{2\pi\beta^2 E}(1 - \frac{mr}{\cos\phi_s})A, \tag{6.6}$$

where A represents either δ or $\phi - \phi_s$. Compared to the one RF system, here the restoring force is multiplied by a factor of $L^2 = 1 - \frac{mr}{\cos\phi_s}$, which could be much greater than 1. Hence the first effect of second RF system is increasing the focusing force. Note the sign of the second term can be changed by reversing the initial phase of the second RF system, therefore one can always stabilize the motion given $mr > 1$.

Equation (6.5) can be derived from the following Hamiltonian

$$H = \frac{1}{2}h\eta\delta^2 + \frac{eV_0}{2\pi\beta^2 E}[\cos\phi - \cos\phi_s + (\phi - \phi_s)\sin\phi_s + \frac{r}{m}(\cos(m\phi - m\phi_s - \pi) + 1)] \quad (6.7)$$

with θ as time variable.

Letting $\phi' = 0$ and $\delta' = 0$, one obtains the equations for the fixed points in (ϕ, δ) phase space

$$\delta = 0, \text{ and } \sin\phi - \sin\phi_s - r\sin m(\phi - \phi_s) = 0. \quad (6.8)$$

Note there are $2m$ pairs of $(\delta_{USF}, \phi_{USF})$ satisfy the above equations for $\phi \in [0, 2\pi]$, which correspond to m pairs of stable and unstable fixed points. We are only interested in the stable fixed point $[\phi_s, 0]$ and the unstable fixed point $[\phi_u, 0]$ with $\phi_u \in [\phi_s - \pi/m, \phi_s]$. The RF bucket is bounded by the torus passing through this unstable fixed point, or given by

$$\delta^2 + \frac{eV_0}{\pi\beta^2 E h\eta}\{\cos\phi - \cos\phi_u + (\phi - \phi_u)\sin\phi_s - \frac{r}{m}\big[\cos(m\phi - m\phi_s) - \cos(m\phi_u - m\phi_s)\big]\} = 0, \quad (6.9)$$

The bucket width and height can be obtained from Eq. (6.9) by letting $\delta = 0$ or $\phi = \phi_s$. The bucket height is

$$\hat{\delta} = \sqrt{\frac{eV_0}{\pi\beta^2 E h\eta}}\{\cos\phi_u - \cos\phi_s + (\phi_u - \phi_s)\sin\phi_s + \frac{r}{m}(1 - \cos m(\phi_u - \phi_s))\}^{1/2}, \quad (6.10)$$

The bucket is between $\phi_s - \pi/m$ and $\phi_s + \pi/m$, and the bucket width is approximately $2\pi/m$, which is much shorter compared to that of the original one RF system. The bucket height depends on both r and m, but in most cases the bucket height is raised by the second RF system. The bucket width and height as functions of r and m are plotted in Fig. 6.2. In case of $mr \gg 1$, the functions of two RF systems are separated: one mainly supplies acceleration, another offers focusing.

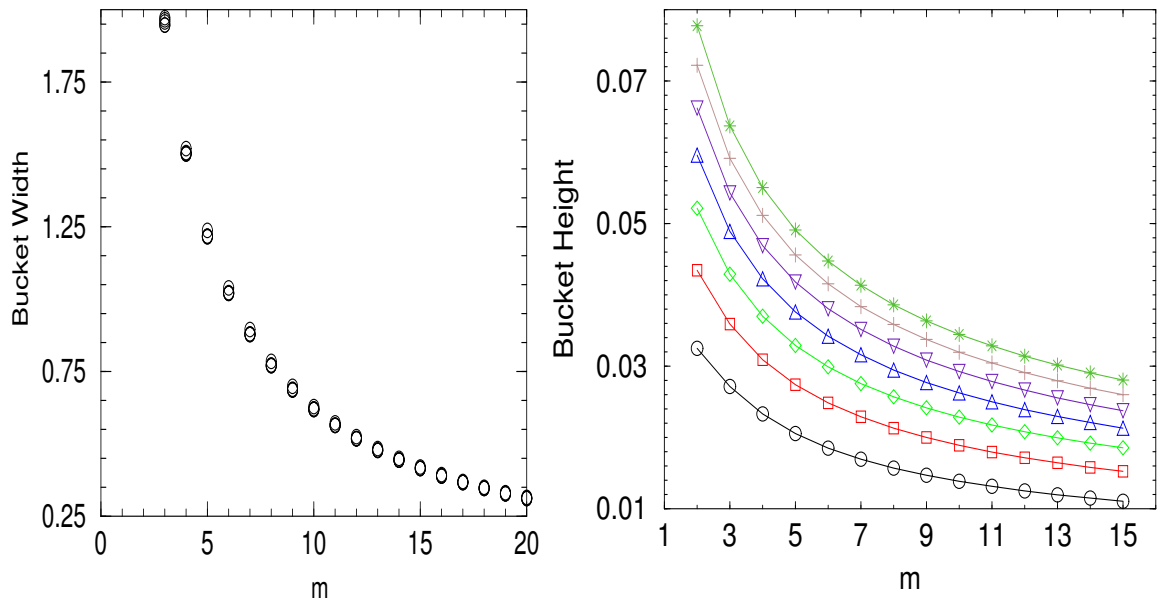

Figure 6.2: Left:Bucket width as a function of r and m. $r = 1, 2, 3, 4, 5$ are calculated but the value of width almost overlap for different r. Right: Bucket height for different r and m. From down to up, $r = 1, 2, 3, 4, 5, 6, 7$ respectively. The lines are plotted to guide the eyes.

To find out the detuning parameter and the tune, let $\Phi = \phi - \phi_s$, using a Taylor expansion of the Hamiltonian around the synchronous phase, one obtains

$$H = \frac{1}{2}h\eta\delta^2 + \frac{eV_0(mr - \cos\phi_s)}{2\pi\beta^2 E}\frac{1}{2}\Phi^2 + \frac{eV_0}{2\pi\beta^2 E}[\frac{\Phi^3}{6}\sin\phi_s + \frac{\Phi^4}{24}(\cos\phi_s - m^3 r) + \ldots \quad (6.11)$$

Transforming to the action angle phase space, *i.e.*, letting

$$\begin{cases} \Phi &= \sqrt{2h\eta J/Q_s}\cos\psi \\ \delta &= -\sqrt{2Q_s J/h\eta}\sin\psi \end{cases}, \quad (6.12)$$

where $Q_s = \sqrt{\frac{h\eta eV_0(mr - \cos\phi_s)}{2\pi\beta^2 E}}$ is the tune for the synchronous particle, one gets

$$H = Q_s J - \frac{\sqrt{2h\eta Q_s}}{3}\frac{\sin\phi_s}{mr - \cos\phi_s}J^{3/2}\cos^3\psi - \frac{h\eta}{6}\frac{m^3 r - \cos\phi_s}{mr - \cos\phi_s}J^2\cos^4\psi, \quad (6.13)$$

where the higher order terms of J^2 have been ignored.

With the generating function

$$\begin{aligned} F_2(\psi, I) &= \psi I + \frac{\sqrt{2h\eta}}{36\sqrt{Q_s}} \frac{\sin\phi_s}{\cos\phi_s - mr} I^{3/2} \sin 3\psi \\ &+ \frac{\sqrt{2h\eta}}{4\sqrt{Q_s}} \frac{\sin\phi_s}{\cos\phi_s - mr} I^{3/2} \sin\psi, \end{aligned} \tag{6.14}$$

the Hamiltonian again is transformed to (I, Ξ) phase space as

$$H = Q_s I - \frac{h\eta}{6} \frac{m^3 r - \cos\phi_s}{mr - \cos\phi_s} I^2 \cos^4 \Xi - \frac{h\eta}{3} (\frac{\sin\phi_s}{mr - \cos\phi_s})^2 I^2 \cos^6 \Xi. \tag{6.15}$$

Therefore the average Hamiltonian is

$$\langle H \rangle = Q_s I - \frac{1}{2} \alpha I^2, \tag{6.16}$$

with the detuning parameter

$$\alpha = \frac{h\eta}{8} [\frac{m^3 r - \cos\phi_s}{mr - \cos\phi_s} + \frac{5}{3} (\frac{\sin\phi_s}{mr - \cos\phi_s})^2]. \tag{6.17}$$

Consequently the tune for the non-synchronous particle is $Q_s - \alpha I$. The beam satisfies Boltzmann distribution [32], and can be well approximated by a Gaussian distribution when $\alpha I \ll Q_s$, and the aspect ratio of the torus is approximately $h\eta/Q_s$.

6.3 Bunch Compression in Electron Storage Rings

In electron storage rings, the equilibrium momentum spread is determined by the damping and quantum excitation, namely [33]

$$\sigma_{\delta e} = \frac{1}{2} \sqrt{f_0 \tau_E} \sigma_\xi, \tag{6.18}$$

Therefore, the equilibrium bunch length can be calculated by

$$\sigma_{\phi e} = \frac{h\eta}{Q_s} \sigma_{\delta e}. \tag{6.19}$$

Compared to the one RF system, both the bunch length and the emittance are reduced by a factor of L. Because $L = \sqrt{1 - \frac{mr}{\cos\phi_s}}$, the higher frequency RF system effectively compresses the bunch.

Actually using one RF system with higher harmonic number, we can also obtain shorter bunches. In the two-RF-system method, the beam loading happens only in the lower frequency RF system. The power input for the higher frequency RF cavities is to maintain the oscillation, and equals the energy dissiplation in the cavity only. This might simplify the microwave power supply in practice.

When the harmonic numbe m of the second RF system is very large, the focusing force is mainly from the second RF system. The first RF system is mainly used for acceleration. This implies the particles might be accelerated by the peak value of the RF voltage, namely, the synchronous phase can be set to $\pi/2$. For the convenience of comparison, the synchronous phase of NLCMDR is used in the following calculations.

6.4 Condition of Increasing Touschek Lifetime

The Touschek lifetime is proportional to $\sigma_x\sigma_z\sigma_\phi(\Delta_{RF})^3$ [36], where Δ_{RF} is the RF bucket height. In our case, only σ_ϕ and Δ_{RF} are changed. In order to increase the Touschek lifetime, the following condition must be satisfied

$$\frac{[\sigma_\phi(\Delta_{RF})^3]_{\text{Two RF systems}}}{[\sigma_\phi(\Delta_{RF})^3]_{\text{One RF system}}} > 1, \tag{6.20}$$

Substituting for σ_ϕ and Δ_{RF}, one obtains

$$\begin{aligned} T(r,m) &= \frac{\left[\cos\phi_u - \cos\phi_s + (\phi_u - \phi_s)\sin\phi_s + \frac{r}{m}(1 - \cos m(\phi_u - \phi_s))\right]^{3/2}}{\sqrt{1 - \frac{mr}{\cos\phi_s}}\left[(\pi - 2\phi_s)\sin\phi_s - 2\cos\phi_s\right]^{3/2}} \\ &> 1 \end{aligned} \tag{6.21}$$

Fig. 6.3 shows $T(r,m)$ for different r and m. Table 6.1 shows the minimum relative

strength needed to increase beam lifetime for different m. We used $\phi_s = 2.329$ Radian in the calculation.

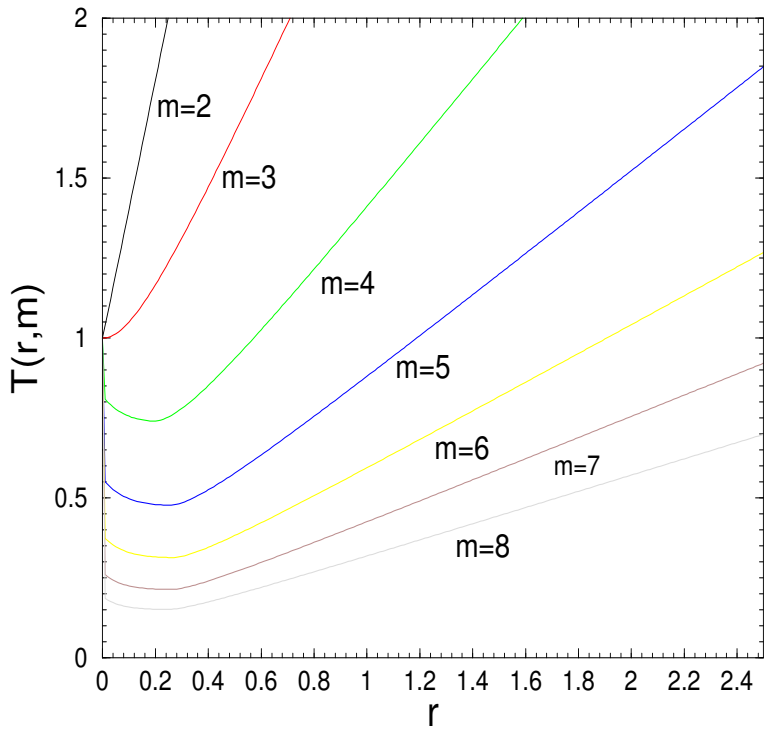

Figure 6.3: Lifetime increasing rate for different r and m. The only parameter $\phi_s = 2.329$ Radian.

Table 6.1: Minimum Relative Strength to Increase Beam Lifetime

m	2	3	4	5	6	7	8
r_{min}	0	0.0085	0.572	1.19	1.91	2.74	3.68

The minimum relative strength for $m = 2$ is very small for $1.70 < \phi_s < 2.70$ Radian.

6.5 Example and Particle Simulation

We again take the Next Linear Collider Main Damping Ring as an example. The momentum spread of of the injected beam is 1% full width, or $\sigma_{\delta i} < 0.2\%$ and the bunch length is less than 10mm, or $\sigma_{\phi i} < 0.150$ Radian for the current 714MHz RF system. There are three bunch trains in the ring and each shall be damped for 25 milli-seconds; however, only less than 3 milli-seconds is needed for longitudinal damping, which leaves sufficient time for longitudinal beam manipulation. The parameters of some possible two RF systems for NLCMDR are given in table 6.2. First we have to choose the bucket size to avoid particle loss at injection. The momentum spread of the injected beam is 1% full width, hence the bucket height must be greater than this number. Note even when $m = 8$ the bucket width is about 0.8 Radian, which is about $5\sigma_{\phi i}$, therefore the bucket width is not a limit.

We favor $m = 4$ since 2856MHz cavities are currently available. The relative strength can be $4 \sim 5$ to get a large compression parameter L and make the other parameters reasonable. We take $r = 4$ in our particle simulation. Note the detuning parameter α is increased by about 5 times, therefore we actually increase the effect of Landau Damping. The Touschek lifetime also increases to 4.45 times of the original value when beam reaches equilibrium. The tori of the Hamiltonians for one rf system and two rf systems are compared in Fig. 6.4.

In particle simulation, we use the mapping equations including damping and quantum fluctuation as follows

$$\begin{cases} \phi_{n+1} &= \phi_n + 2\pi h\eta\delta_n \\ \delta_{n+1} &= \delta_n + \frac{eV_0}{\beta^2 E}(\sin\phi_{n+1} - \sin\phi_s - r\sin(m\phi_{n+1} - m\phi_s)) - \frac{4\pi}{\omega_0\tau_E}\delta_n + \xi_n \end{cases} \tag{6.22}$$

where ξ_n has the same meaning as we have described in Eq. (5.22). 10,000 particles are initially distributed in (ϕ, δ) phase space in a Gaussian distribution. The coordinates are changed by the mapping equations every turn. Fig. 6.5 shows the damping

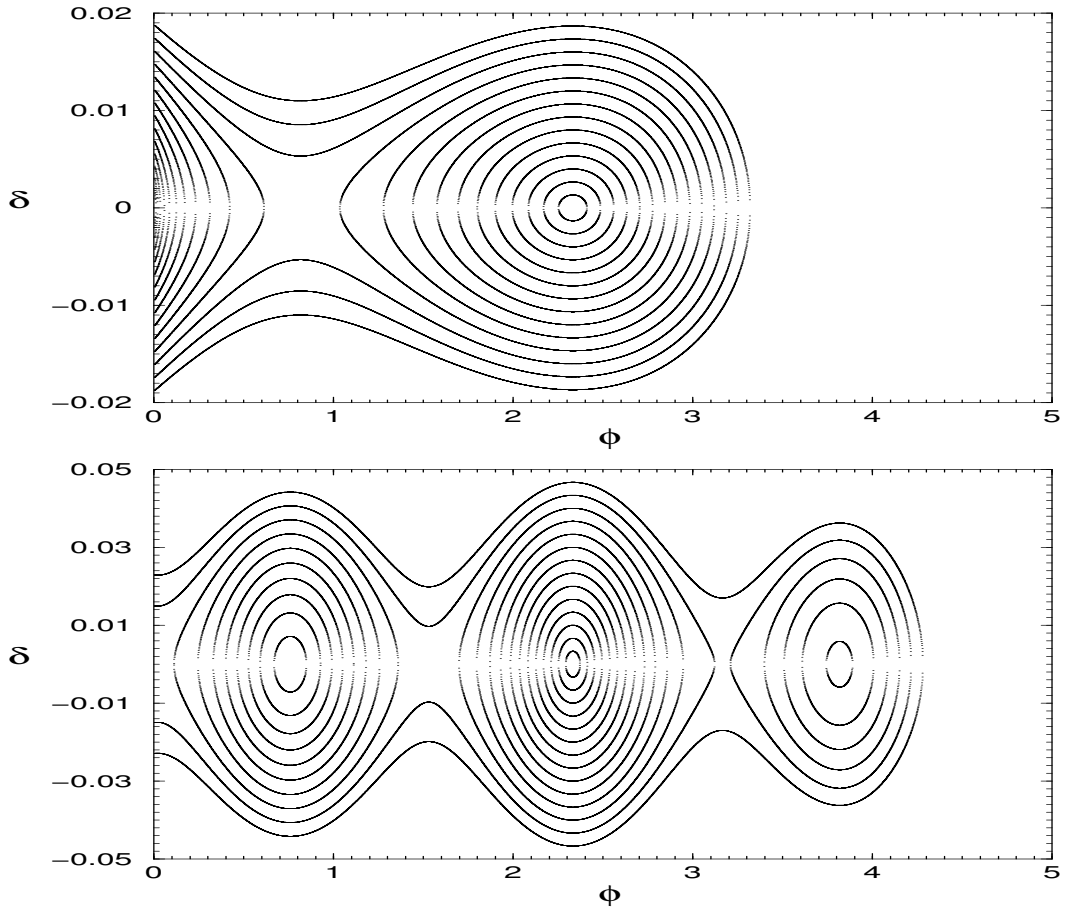

Figure 6.4: The tori for the longitudinal Hamiltonian of NLCMDR. Top: original Hamiltonian. Bottom: with a 4th harmonic rf system. Note the increase of the bucket height.

process of the momentum spread, bunch length and emittance in 25 milli-seconds. The equilibrium bunch length is 0.735 mm, which is about one fifth of the current design value (3.6 mm). The results are as expected.

Table 6.2: Parameters of Two RF Systems for NLCMDR

m	r	ϕ_u	Width	Height(%)	Q_s	α	L	T(r,m)
0	0	0.813	2.324	1.51	0.0035	0.074	1.0	1.00
2	5	0.762	2.837	6.62	0.0138	0.0987	3.94	21.4
3	3.5	1.260	1.961	4.60	0.0141	0.22	4.03	7.03
3	5	1.266	1.972	5.43	0.0167	0.224	4.78	9.748
4	3	1.521	1.501	3.70	0.0150	0.393	4.30	3.431
4	4	1.526	1.504	4.22	0.0172	0.398	4.93	4.450
4	5	1.530	1.506	4.69	0.0192	0.401	5.49	5.470
5	2	1.674	1.218	2.74	0.0138	0.607	3.94	1.523
5	3	1.683	1.215	3.29	0.0167	0.620	4.78	2.173
5	4	1.687	1.216	3.76	0.0192	0.626	5.49	2.825
6	2	1.784	1.022	2.49	0.0150	0.883	4.30	1.042
6	3	1.791	1.020	2.99	0.0182	0.899	5.21	1.494
7	2	1.864	0.881	2.29	0.0162	1.21	4.62	0.755
7	3	1.869	0.878	2.76	0.0197	1.23	5.62	1.087
8	3	1.927	0.771	2.57	0.0210	1.61	5.99	0.826

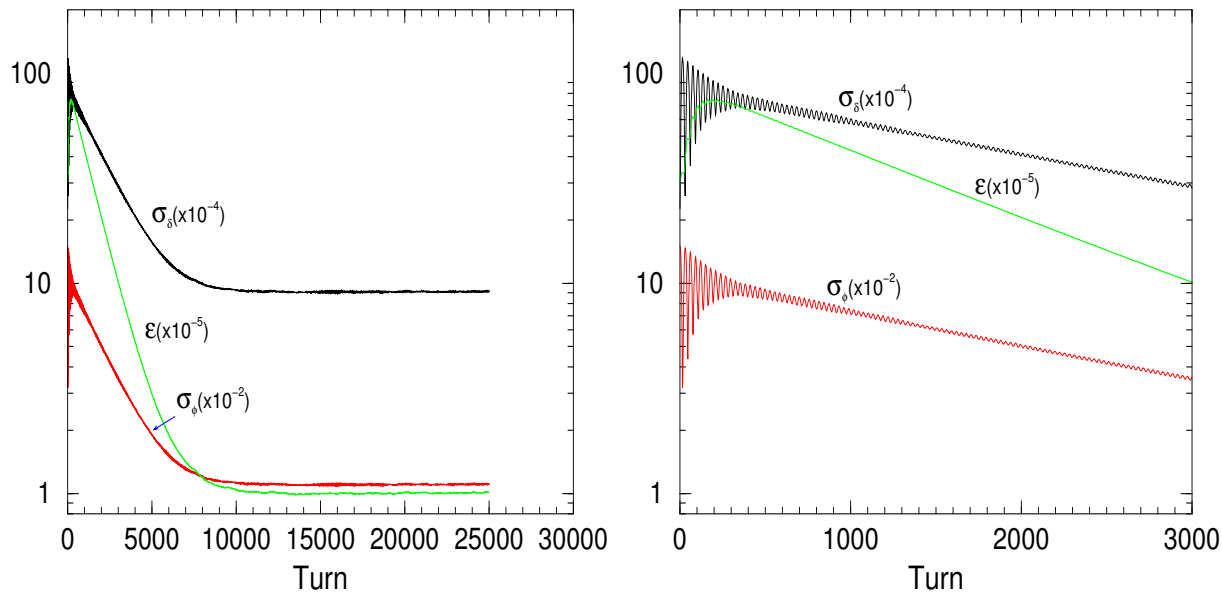

Figure 6.5: $r = 4, m = 4$ for the second RF system. Equilibrium parameters are $\sigma_{\delta e} = 0.091\%$, $\sigma_{\phi e} = 0.011$Radian, or $\sigma_{ze} = 0.735$mm, $\epsilon_e = 1.0 \times 10^{-5}$. Right plot details the first 3,000 turns. Note the quadrupole mode oscillation at the beginning due to mismatch.

Chapter 7

Conclusion

Quadrupole mode perturbation in both transverse and longitudinal directions has been studied in this dissertation.

In the transverse direction, the perturbation is realized by inserting an rf quadrupole in the ring accelerator. The original Hill's equation is changed

$$y'' + K(s)y = K_{rf}(s)\cos(\omega_{rf}t + \theta)\ y, \tag{7.1}$$

where $K_{rf}(s)$ is the strength parameter, and ω_{rf} is the working frequency of the rf quadrupole. We used the Hamiltonian method to solve this equation. In the resonance rotating frame, the Hamiltonian has the following form (Eq.3.8)

$$H(\psi, I) = \delta I + C_1 I \cos 2\psi, \tag{7.2}$$

where (I, ψ) are action-angle coordinates, δ is related to the frequency of the rf quadrupole and C_1 is the effective strength of the rf quadrupole. This Hamiltonian is time independent and the torus is elliptical. Particle simulation shows that the trace of one single particle does move around the torus of the Hamiltonian.

According to Vlasov equation, the particle system governed by the above Hamiltonian must satisfy Boltzmann distribution provided the initial distribution is Gaussian.

The Boltzmann distribution is given by

$$\rho_B(H) = \frac{1}{2\pi\epsilon_0} e^{-\frac{H}{\Omega\epsilon_0}}, \tag{7.3}$$

where Ω is the tune of the Hamiltonian, ϵ_0 is the initial emittance of the particle system. In case of the linear Hamiltonian, the Boltzmann distribution is [Eq.3.31]

$$\rho_B(J_y, \psi_y) = \frac{1}{2\pi\epsilon_0} e^{-\frac{\delta J_y + C_1 J_y \cos 2\psi_y}{\sqrt{\delta^2 - C_1^2}\epsilon_0}}. \tag{7.4}$$

The particle simulation results agree very well with this theoretical prediction.

The nonlinearity must be considered in a real machine. When a detuning term is included, the linear Hamiltonian becomes (Eq.3.10)

$$H = \delta I + C_1 I \cos 2\psi + \frac{1}{2}\alpha_{yy} I^2, \tag{7.5}$$

where α_{yy} is the detuning parameter. The torus of this nonlinear Hamiltonian is much more complicated. It has bifurcation and triplication point. The beam can be split into islands. The particle simulation still agree with the theory even in this complicated case.

All of this discussion is in the resonance rotating frame. If observed from the lab frame, the torus of the Hamiltonians rotates in phase space. This means the second moments of the system oscillate in the lab frame. In accelerator physics, it means the beam width oscillates with time. This oscillation signal can be detected by a Beam Position Monitor. For the linear Hamiltonian in Eq.7.2, the emittance of the beam can be deduced from the following formula (Eq.4.15)

$$\delta^2 = 4C_1^2\ \beta_x^2 \epsilon_0^2 \frac{1}{b_1^2} + C_1^2. \tag{7.6}$$

For the nonlinear Hamiltonian in Eq.(7.5), one can still use a phenomenological formula (Eq.4.16)

$$b_1 = \frac{2C_1\beta_x\epsilon_0}{\sqrt{(\delta + F\alpha_{xx}\epsilon_0)^2 - C_1^2}}. \tag{7.7}$$

The particle simulation again supports these results.

The other applications of the rf quadrupole include mismatch compensation and overcoming spin resonances. Particle simulation was also done to verify the theory.

In the longitudinal direction, voltage modulation can induce quadrupole mode oscillation. If the modulation frequency is close to twice of the synchrotron tune, one can obtain a similar Hamiltonian in the resonance rotating frame (Eq.5.12)

$$\bar{H} = \Delta I - \frac{1}{2}\alpha I^2 + CI\cos 2\Psi, \tag{7.8}$$

where Δ, α and C are parameters related to the modulation and the particular machine. All the physics is the same as that in the transverse direction since the Hamiltonian is identical. In the longitudinal direction, quadrupole mode oscillation means bunch length oscillation. If we extract the beam while the bunch oscillates to the minimum, then the bunch is compressed. Our simulation shows that the bunch can be compressed by about two times.

Finally the double rf system method was explored to compress the bunch. The Hamiltonian method is again a good approach to analyze this problem.

Appendix A

Canonical Transformations

We want to transform the independent phase space coordinates q_i, p_i, to a new set Q_i, P_i, with equations of transformation:

$$\begin{aligned} Q_i &= Q_i(q,p,t) \\ P_i &= P_i(q,p,t) \end{aligned} . \tag{A.1}$$

In the meantime, there exists some function $K(Q,P,t)$ such that the equations of motion in the new set are in the Hamiltonian form

$$\dot{Q}_i = \frac{\partial K}{\partial P_i}, \qquad \dot{P}_i = -\frac{\partial K}{\partial Q_i}. \tag{A.2}$$

Transformations for which Eqs.(A.2) are valid are said to be canonical. The function K plays the role of the Hamiltonian in the new coordinate set.

From Hamilton's principle [1] we know that

$$\delta \int_{t_1}^{t_2} (\sum p_i \dot{q}_i - H(q,p,t))dt = 0. \tag{A.3}$$

If the Q_i and P_i are to be canonical coordinates they must satisfy a modified Hamilton's principle of the form:

$$\delta \int_{t_1}^{t_2} (\sum P_i \dot{Q}_i - K(Q,P,t))dt = 0. \tag{A.4}$$

The simultaneous validity of Eqs.(A.3) and (A.4) require they differ at most by a total time derivative of an arbitrary function F. The integral between the two end points of such a difference term is then

$$\int_{t_1}^{t_2} \frac{dF}{dt} dt = F(t_2) - F(t_1). \tag{A.5}$$

The variation of this integral is automatically zero for any function F since the variation vanishes at the end points. The arbitrary function F is called the generating function of the transformation. F must be a function of both the old and new variables in order to change the transformation. In addition to the time t it may be a function of up to $4n$ variables, where n is the number of degrees. Only $2n$ of these are independent, because the two sets of coordinates are connected by the 2n transformation equations of (A.1). The generating function can therefore be written as a function of independent variables in one of the four forms:

$$F_1(q, Q, t), F_2(q, P, t), F_3(p, Q, t), F_4(p, P, t) \tag{A.6}$$

The circumstances of the problem will dictate which form is to be chosen. If the first form F_1 is a suitable choice then the integrands of Eqs.(A.3) and (A.4) can be connected by the relation:

$$\sum p_i \dot{q}_i - H = \sum P_i \dot{Q}_i - K + \frac{d}{dt} F_1(q, Q, t). \tag{A.7}$$

The total time derivative of F can be expanded as:

$$\frac{dF_1}{dt} = \frac{\partial F_1}{\partial Q_i} \frac{dQ_i}{dt} + \frac{\partial F_1}{\partial q_i} \frac{dq_i}{dt} + \frac{\partial F_1}{\partial t}, \tag{A.8}$$

therefore Eq. (A.7) becomes

$$\sum (p_i - \frac{\partial F_1}{\partial q_i}) \dot{q}_i - H = \sum (P_i - \frac{\partial F_1}{\partial Q_i}) \dot{Q}_i - K + \frac{\partial F_1}{\partial t}. \tag{A.9}$$

Since the old and new coordinates, q_i and Q_i are considered here as independent, Eq.(A.7) can hold identically only if the coefficients of the $\dot{q}_i$ and $\dot{Q}_i$ separately vanish:

$$p_i = \frac{\partial F_1}{\partial q_i}, P_i = -\frac{\partial F_1}{\partial Q_i}, \tag{A.10}$$

finally leaving:

$$K = H + \frac{\partial F_1}{\partial t}. \tag{A.11}$$

Therefore Eqs.(A.10) yields the transformation and Eq.(A.11) provides the connection between the new Hamiltonian K and the old one.

When the generating Function is of type F_2, the transition from q, Q to q, P can be accomplished by a Legendre transformation, since

$$\frac{\partial F_1}{\partial Q_i} = -P_i, \tag{A.12}$$

therefore F_2 can be defined in terms of F_1 according to the relation

$$F_2(q, P, t) = F_1(q, Q, t) + \sum_i P_i Q_i. \tag{A.13}$$

Substituting F_1 back into Eq.(A.7), one can find the relation

$$p_i = \frac{\partial F_2}{\partial q_i}, Q_i = \frac{\partial F_2}{\partial P_i}, \tag{A.14}$$

and

$$K = H + \frac{\partial F_2}{\partial t}. \tag{A.15}$$

Similarly define $F_3 = F_1 - \sum q_i p_i$ and $F_4 = F_1 + \sum P_i Q_i - \sum p_i q_i$, one can easily obtain

$$q_i = -\frac{\partial F_3}{\partial p_i}, P_i = -\frac{\partial F_3}{\partial Q_i}, K = H + \frac{\partial F_3}{\partial t}, \tag{A.16}$$

and

$$q_i = -\frac{\partial F_4}{\partial p_i}, Q_i = \frac{\partial F_4}{\partial P_i}, K = H + \frac{\partial F_4}{\partial t}. \tag{A.17}$$

Appendix B

Boltzmann Distribution for the Nonlinear Perturbed Hamiltonian

For the nonlinear Hamiltonian $H(J_y, \psi_y) = \delta J_y + J_y C_1 \cos 2\psi_y + \frac{1}{2}\alpha_{yy} J_y^2$, if we write the Boltzmann distribution as

$$\rho_B(J_y, \psi_y) = \frac{1}{N} e^{-\frac{\delta J_y + C_1 J_y \cos 2\psi_y + \frac{1}{2}\alpha_{yy} J_y^2}{E_t}}, \tag{B.1}$$

then in principle, we can solve the normalization constant and the thermal energy from the following two equations

$$\begin{cases} \int_0^\infty dJ_y \int_0^{2\pi} d\psi_y \rho_B(J_y, \psi_y) & = & 1 \\ \sqrt{\langle Y^2 \rangle \langle P_y^2 \rangle - \langle Y P_y \rangle^2} & = & \epsilon_0 \end{cases}. \tag{B.2}$$

Let's first calculate the normalization integral.

$$\begin{aligned}
I_{norm.} &= \int_0^\infty dJ_y \int_0^{2\pi} d\psi_y \rho_B(J_y, \psi_y) \\
&= \frac{1}{N}\int_0^\infty dJ_y \int_0^{2\pi} d\psi_y e^{-\frac{\delta J_y + \frac{1}{2}\alpha_{yy}J_y^2}{E_t} - \frac{C_1 J_y \cos 2\psi_y}{E_t}} \\
&= \frac{2\pi}{N}\int_0^\infty dJ_y I_0(\frac{C_1 J_y}{E_t}) e^{-\frac{\delta J_y + \frac{1}{2}\alpha_{yy}J_y^2}{E_t}} \\
&= \frac{2\pi}{N} I_0(C_1 \frac{\partial}{\partial \delta}) \int_0^\infty dJ_y e^{-\frac{\delta J_y + \frac{1}{2}\alpha_{yy}J_y^2}{E_t}} \\
&= \frac{\pi}{N}\sqrt{\frac{2\pi E_t}{\alpha_{yy}}} I_0(\xi \frac{\partial}{\partial u}) e^{u^2} erfc(u) \qquad \text{(B.3)}
\end{aligned}$$

where $\xi = \frac{C_1}{\sqrt{2E_t\alpha_{yy}}}$ and $u = \frac{\delta}{\sqrt{2E_t\alpha_{yy}}}$. $I_0(x)$ is the zeroth order Bessel function. In the case of $u \gg 1$, the complementary error function can be expanded in an asymptotic representation

$$erfc(u) = \frac{e^{-u^2}}{\sqrt{\pi}u}(1 - \frac{1}{2u^2} + \frac{1\cdot 3}{(2u^2)^2} - \frac{1\cdot 3\cdot 5}{(2u^2)^3} + \cdots), \qquad \text{(B.4)}$$

to obtain

$$\begin{aligned}
I_{norm.} &= \frac{\pi}{N}\sqrt{\frac{2E_t}{\alpha_{yy}}} I_0(\xi \frac{\partial}{\partial u})\frac{1}{u}(1 - \frac{1}{2u^2} + \frac{1\cdot 3}{(2u^2)^2} - \frac{1\cdot 3\cdot 5}{(2u^2)^3} + \cdots) \\
&= \frac{\pi}{N}\sqrt{\frac{2E_t}{\alpha_{yy}}}(1 + \frac{1}{2^2}\xi^2\frac{\partial^2}{\partial u^2} + \cdots)\frac{1}{u}(1 - \frac{1}{2u^2} + \frac{1\cdot 3}{(2u^2)^2} - \frac{1\cdot 3\cdot 5}{(2u^2)^3} + \cdots).
\end{aligned}$$

Note that

$$u^k \frac{\partial^k}{\partial u^k} u^{-n} = (-1)^k \frac{(n+k-1)!}{(n-1)!} u^{-n}, \qquad \text{(B.5)}$$

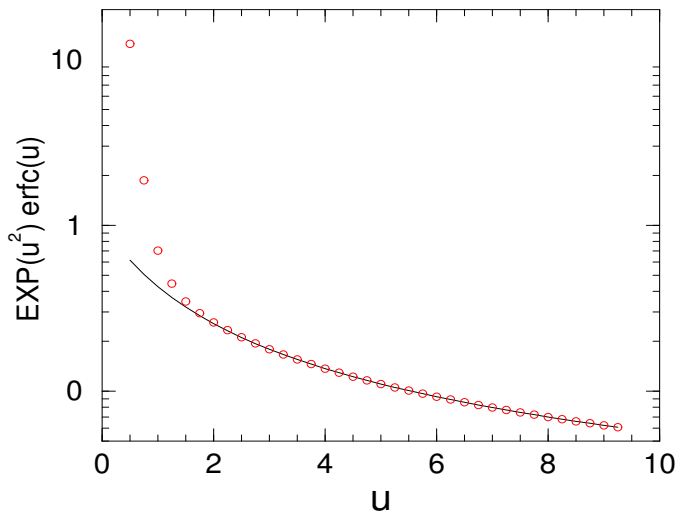

Figure B.1: Solid line is the value of $e^{u^2} erfc(u)$, the circles is the first two term approximation, i.e. calculated by $f(u) = \frac{1}{\sqrt{\pi}u}(1 - \frac{1}{2u^2} + \frac{1 \cdot 3}{(2u^2)^2})$. Therefore u must be greater than 2 to keep accuracy. More terms won't help.

where n, k are integers and $n, k \neq 0$, therefore

$$\begin{aligned}
\frac{N}{\pi}\sqrt{\frac{\alpha_{yy}}{2E_t}} \cdot I_{norm.} &= \frac{1}{u}(1 - \frac{1}{2u^2} + \frac{1 \cdot 3}{(2u^2)^2} - \frac{1 \cdot 3 \cdot 5}{(2u^2)^3} + \cdots) \\
&+ \frac{1}{2^2}(\frac{\xi}{u})^2 \frac{1}{u}(2! - 4 \cdot 3 \cdot \frac{1}{2u^2} + 6 \cdot 5 \cdot \frac{1 \cdot 3}{(2u^2)^2} - 8 \cdot 7 \cdot \frac{1 \cdot 3 \cdot 5}{(2u^2)^3} + \cdots) \\
&+ \frac{1}{2^2 \cdot 4^2}(\frac{\xi}{u})^4 \frac{1}{u}(4! - \frac{6!}{2!}\frac{1}{2u^2} + \frac{8!}{4!}\frac{1 \cdot 3}{(2u^2)^2} - \frac{10!}{6!} \cdot \frac{1 \cdot 3 \cdot 5}{(2u^2)^3} + \cdots) \\
&\vdots \\
&= \frac{1}{\sqrt{u^2 - \xi^2}} - \frac{1}{2u^2}\frac{1}{2!}\frac{\partial^2}{\partial \xi^2}\frac{\xi^2}{\sqrt{u^2 - \xi^2}} \\
&+ \frac{1 \cdot 3}{(2u^2)^2}\frac{1}{4!}\frac{\partial^4}{\partial \xi^4}\frac{\xi^4}{\sqrt{u^2 - \xi^2}} - \frac{1 \cdot 3 \cdot 5}{(2u^2)^3}\frac{1}{6!}\frac{\partial^6}{\partial \xi^6}\frac{\xi^6}{\sqrt{u^2 - \xi^2}} + \cdots \qquad \text{(B.6)}
\end{aligned}$$

where $\mid u/\xi \mid = \mid \delta/C_1 \mid < 1$ is required in our derivation and the following identity has

been used

$$\frac{1}{\sqrt{1+t^2}} = \sum_{n=0}^{\infty} P_n(0) t^n, \tag{B.7}$$

with P_n as the nth Legendre function.

Define

$$\begin{aligned} G(u,\xi) &= I_0(\xi\frac{\partial}{\partial u})\sqrt{\pi}e^{u^2} erfc(u) \\ &= I_0(\xi\frac{\partial}{\partial u})(\frac{1}{u} - \frac{1}{2u^3} + e^{u^2}\int_u^{\infty} dx \frac{3e^{-x^2}}{2x^4}) \\ &= \frac{1}{\sqrt{u^2-\xi^2}} - \frac{1}{4}\frac{2u^2+\xi^2}{(u^2-\xi^2)^{5/2}} + I_0(\xi\frac{\partial}{\partial u})e^{u^2}\int_u^{\infty} dx \frac{3e^{-x^2}}{2x^4}, \end{aligned} \tag{B.8}$$

therefore

$$I_{norm.} = \frac{2\pi}{N}\sqrt{\frac{E_t}{2\alpha_{yy}}} G(u,\xi) = 1. \tag{B.9}$$

For the second equation in 3.26, notice that

$$\begin{aligned} \langle J_y \rangle &= \int_0^{\infty} dJ_y \int_0^{2\pi} d\psi_y J_y \rho_B(J_y,\psi_y) \\ &= -E_t \frac{\partial}{\partial \delta}\int_0^{\infty} dJ_y \int_0^{2\pi} d\psi_y \rho_B(J_y,\psi_y) \\ &= -\frac{2\pi}{N}\frac{E_t}{2\alpha_{yy}}\frac{\partial}{\partial u} G(u,\xi) \end{aligned} \tag{B.10}$$

and

$$\begin{aligned} \langle J_y \cos 2\psi_y \rangle &= \int_0^{\infty} dJ_y \int_0^{2\pi} d\psi_y J_y \cos 2\psi_y \rho_B(J_y,\psi_y) \\ &= -E_t \frac{\partial}{\partial C_1}\int_0^{\infty} dJ_y \int_0^{2\pi} d\psi_y \rho_B(J_y,\psi_y) \\ &= -\frac{2\pi}{N}\frac{E_t}{2\alpha_{yy}}\frac{\partial}{\partial \xi} G(u,\xi). \end{aligned} \tag{B.11}$$

Note $\langle J_y \cos 2\psi_y \rangle = \langle Y^2 \rangle - \langle P^2 \rangle$ is negative when $\alpha_{yy} > 0$. From above two equations, one arrives at

$$\begin{aligned} \langle Y^2 \rangle &= \langle J_y \rangle + \langle J_y \cos 2\psi_y \rangle \\ &= -\frac{2\pi}{N}\frac{E_t}{2\alpha_{yy}}(\frac{\partial}{\partial u} + \frac{\partial}{\partial \xi})G(u,\xi), \end{aligned} \tag{B.12}$$

and

$$\begin{aligned} \langle P_y^2 \rangle &= \langle J_y \rangle - \langle J_y \cos 2\psi_y \rangle \\ &= -\frac{2\pi}{N}\frac{E_t}{2\alpha_{yy}}(\frac{\partial}{\partial u} - \frac{\partial}{\partial \xi})G(u,\xi), \end{aligned} \tag{B.13}$$

Therefore

$$\langle Y^2 \rangle \langle P_y^2 \rangle = (\frac{2\pi}{N}\frac{E_t}{2\alpha_{yy}})^2 (G_u^2(u,\xi) - G_\xi^2(u,\xi)), \tag{B.14}$$

and $\langle Y P_y \rangle$ is zero due to the symmetry, hence

$$(\frac{2\pi}{N}\frac{E_t}{2\alpha_{yy}})^2 (G_u^2(u,\xi) - G_\xi^2(u,\xi)) = \epsilon_0^2. \tag{B.15}$$

Substituting N from Eq. (B.9), one gets

$$G_u^2(u,\xi) - G_\xi^2(u,\xi) = \frac{4\alpha_{yy}^2 \epsilon_0^2}{\delta^2} u^2 G^2(u,\xi) \tag{B.16}$$

Therefore one can solve for u from Eq. (B.16) and then calculate N from Eq.. (B.9). Keeping $G(u,\xi)$ to the first order of $\frac{1}{u}$, one obtains $E_t = \sqrt{\delta^2 - C_1^2}\epsilon_0$ and $N = 2\pi\epsilon_0$, which agree with Eq. (3.31). Keeping to the third term gives

$$G(u,\xi) \approx \frac{1}{\sqrt{u^2-\xi^2}} - \frac{1}{4}\frac{2u^2+\xi^2}{(u^2-\xi^2)^{5/2}} + \frac{3}{32}\frac{8u^4+24u^2\xi^2+3\xi^4}{(u^2-\xi^2)^{9/2}}, \tag{B.17}$$

$$G_u(u,\xi) \approx -\frac{u}{(u^2-\xi^2)^{3/2}}\left[1 - \frac{\frac{3}{2}u^2+\frac{9}{4}\xi^2}{(u^2-\xi^2)^2} + \frac{15}{32}\frac{8u^4+40u^2\xi^2+15\xi^4}{(u^2-\xi^2)^4}\right], \tag{B.18}$$

$$G_\xi(u,\xi) \approx \frac{\xi}{(u^2-\xi^2)^{3/2}}\left[1 - \frac{6u^2+\frac{3}{2}\xi^2}{2(u^2-\xi^2)^2} + \frac{45}{32}\frac{8u^4+12u^2\xi^2+\xi^4}{(u^2-\xi^2)^4}\right]. \tag{B.19}$$

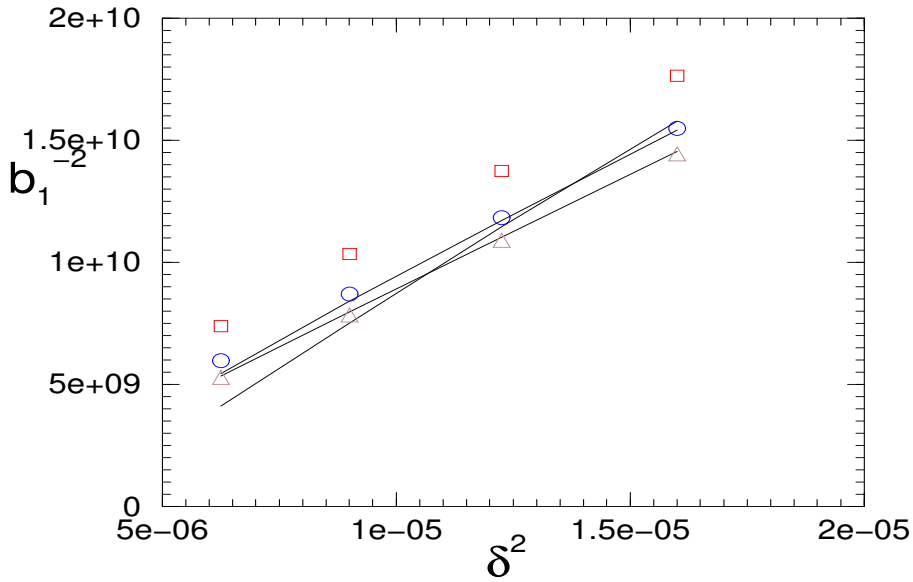

Figure B.2: The comparison of the results of b_1. The parameters used are $C_1 = 1.e-3$, $\alpha_{yy} = 50(\triangle), 100(\bigcirc), 200(\square)$. The solid lines are the result from equation (B.20) and the symbols are from the simulation. Note the third solid line is supposed to fit the squares.

For the above functions to be convergent, the necessary conditions are $u > 2$ and $u^2(1-v^2) > 1$.

Define the quadrupole mode transfer function b_1 as following

$$\begin{aligned} b_1 &= |2\beta_y \langle J_y \cos 2\psi_y \rangle| \\ &\approx \frac{\beta_y \delta}{\alpha_{yy} u^2} \frac{v}{1-v^2} \frac{1 - \frac{1}{2u^2}\frac{6+\frac{3}{2}v^2}{(1-v^2)^2} + \frac{45}{32}\frac{1}{u^4}\frac{8+12v^2+v^4}{(1-v^2)^4}}{1 - \frac{1}{4u^2}\frac{2+v^2}{(1-v^2)^2} + \frac{3}{32}\frac{1}{u^4}\frac{8+24v^2+3v^4}{(1-v^2)^4}}. \end{aligned} \tag{B.20}$$

Therefore in principle one can calculate b_1 once δ, C_1 and α_{yy} are given. Note $G(u, \xi)$ is a complicated function, the value oscillates term by term. As a result, this approximation is good only when α is small. For a certain C_1 one would prefer larger

δ to get Eq. (B.20) closer to the real result, however, the perturbation effect is small while δ is relatively large. Fig. B.2 shows the comparison between the simulation and the calculation. For $\alpha < 100$ the calculation result agrees well with the simulation, however, when α is large, the result is not good. Further discussion can be found in Chapter Four about the quadrupole transfer function. There a phenomenological formula is used to solve this mathematical problem.

Appendix C

Signals from Beam Position Monitor

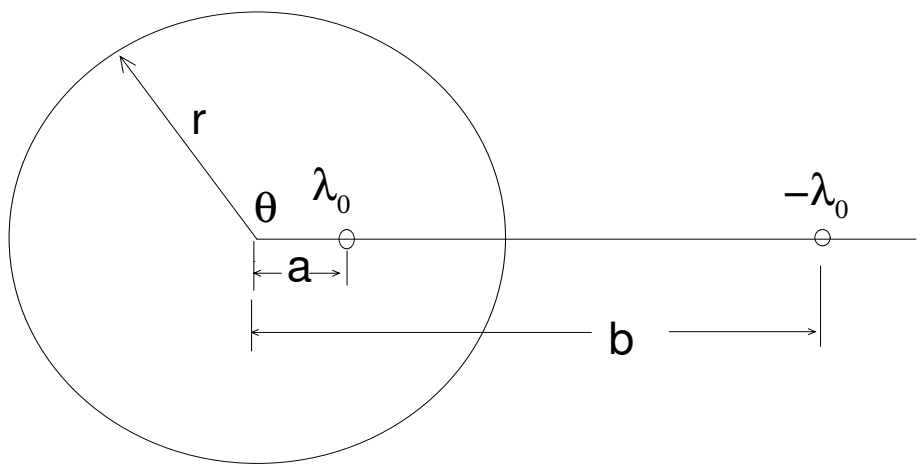

Figure C.1: Charge density on the surface of a cylinder.

As is sketched in Fig. C.1, consider a line charge inside an infinitely long circular conducting cylinder with radius r. If the line charge density is λ_0, and it is off center by distance a, then the image charge $-\lambda_0$ is located at distance $b = r^2/a$ from the

center. The electric potential for the two line charges is given by

$$\Phi(\vec{r}) = \frac{\lambda_0}{2\pi\epsilon_0}\ln|\vec{r}-\vec{a}| - \frac{\lambda_0}{2\pi\epsilon_0}\ln|\vec{r}-\vec{b}|, \tag{C.1}$$

where ϵ_0 is the permittivity of vacuum. The charge density on the inside surface of the cylinder can be calculated by

$$\begin{aligned}\sigma(r,\theta) &= \epsilon_0 E_r = -\epsilon_0 \bigtriangledown \Phi(\vec{r}) \\ &= -\frac{\lambda_0}{2\pi r}\frac{r^2-a^2}{r^2+a^2-2ra\cos\theta}\end{aligned} \tag{C.2}$$

Note

$$\frac{r^2-a^2}{r^2+a^2-2ra\cos\theta} = Re(\frac{1+\frac{a}{r}e^{i\theta}}{1-\frac{a}{r}e^{i\theta}}) = 1+2\sum_{n=1}^{\infty}(\frac{a}{r})^n\cos n\theta, \tag{C.3}$$

therefore

$$\sigma(r,\theta) = -\frac{\lambda_0}{2\pi r}[1+2\sum_{n=1}^{\infty}(\frac{a}{r})^n\cos n\theta]. \tag{C.4}$$

In reality the beam is not a line charge, and its transverse dimension is comparable to the radius of the beam pipe, therefore one has to integrate over the current distribution of the beam to get the charge density on the Beam Position Monitor. Suppose the beam has a current distribution $I\rho(a,\theta_a)$, where I is the total current of the beam, $\rho(a,\theta_a)$ is the normalized beam distribution, then the total image charge density on the inside surface is given by

$$\sigma_b(r,\theta) = -\frac{I}{2\pi r}\int da\int d\theta_a\rho(a,\theta_a)[1+2\sum_{n=1}^{\infty}(\frac{a}{r})^n\cos n(\theta-\theta_a)] \tag{C.5}$$

Usually the Beam Position Monitor consists of two or four round metal strips, and they are installed symmetrically around the beam pipe center. Suppose the open angle of one strip is from θ_0 to $\theta_0+\Delta\theta$, then the total charge on this strip is given by

$$\begin{aligned}q(\theta_0) &= \int_{\theta_0}^{\theta_0+\Delta\theta} d\theta\sigma_b(r,\theta) \\ &= -\frac{I}{2\pi r}\int da\int d\theta_a\rho(a,\theta_a)[\Delta\theta+\sum_{n=1}^{\infty}\frac{4}{n}(\frac{a}{r})^n\cos n(\theta_0-\theta_a+\Delta\theta/2)\sin n\Delta\theta/2].\end{aligned}$$

Adding up all four signals from a four-strip BPM, one gets

$$q(\theta_0) + q(\theta_0 + \pi/2) + q(\theta_0 + \pi) + q(\theta_0 + 3\pi/2) = -\frac{2I}{\pi r}[\Delta\theta$$
$$+ \int da \int d\theta_a \rho(a, \theta_a) \sum_{n=1}^{\infty} \frac{1}{n}(\frac{a}{r})^{4n} \cos 4n(\theta_0 - \theta_a + \Delta\theta/2) \sin 2n\Delta\theta]. \quad \text{(C.6)}$$

Usually a/r is small, therefore the first term is the dominant term and it is proportional to the current of the beam.

Substracting two opposite strip signals gives

$$q(\theta_0) - q(\theta_0 + \pi) = -\frac{I}{2\pi r} \int da \int d\theta_a \rho(a, \theta_a)$$
$$\times \sum_{n=1}^{\infty} \frac{8}{2n-1}(\frac{a}{r})^{2n-1} \cos(2n-1)(\theta_0 - \theta_a + \Delta\theta/2) \sin(2n-1)\Delta\theta/2, \quad \text{(C.7)}$$

Keeping only the dominant term, one obtains

$$\begin{aligned} & q(\theta_0) - q(\theta_0 + \pi) \\ & \approx -\frac{4I}{\pi r^2} \sin \Delta\theta/2 \int da \int d\theta_a \rho(a, \theta_a) a \cos(\theta_0 - \theta_a + \Delta\theta/2) \\ & = -\frac{4I}{\pi r^2} \sin \Delta\theta/2 \Big[\langle x \rangle \cos(\theta_0 + \Delta\theta/2) + \langle z \rangle \sin(\theta_0 + \Delta\theta/2)\Big] \\ & = \begin{cases} -\frac{4I}{\pi r^2} \sin \frac{\Delta\theta}{2} \langle x \rangle & \text{if } \theta_0 + \Delta\theta/2 = 0 \\ -\frac{4I}{\pi r^2} \sin \frac{\Delta\theta}{2} \langle z \rangle & \text{if } \theta_0 + \Delta\theta/2 = \pi/2 \end{cases}, \end{aligned} \quad \text{(C.8)}$$

where $\langle x \rangle = \int da \int d\theta_a \rho(a, \theta_a) a \cos\theta_a$ is the horizontal average position and $\langle z \rangle$ the vertical average position. Note the result is related to the open angle by $\sin \Delta\theta/2$, hence large $\Delta\theta$ results in better sensitivity. For two-strip BPM, $\Delta\theta$ can be up to π, therefore it can be more sensitive than four-strip BPM does in detecting the position of the beam.

Combining the four signals as

$$q(\theta_0) + q(\theta_0 + \pi) - q(\theta_0 + \pi/2) - q(\theta_0 + 3\pi/2) = -\frac{2I}{\pi r} \int da \int d\theta_a \rho(a, \theta_a)$$
$$\times \sum_{n=1}^{\infty} \frac{2}{2n-1}(\frac{a}{r})^{4n-2} \cos(4n-2)(\theta_0 - \theta_a + \Delta\theta/2) \sin(2n-1)\Delta\theta. \quad \text{(C.9)}$$

Again keeping only the first term, one gets

$$\begin{aligned} & q(\theta_0) + q(\theta_0 + \pi) - q(\theta_0 + \pi/2) - q(\theta_0 + 3\pi/2) \\ \approx & \; -\frac{4I}{\pi r^3} \int da \int d\theta_a \rho(a, \theta_a) a^2 \cos(2\theta_0 - 2\theta_a + \Delta\theta) \sin \Delta\theta. \end{aligned} \tag{C.10}$$

Letting $\theta_0 + \Delta\theta/2 = 0$, one obtains

$$q(\theta_0) + q(\theta_0 + \pi) - q(\theta_0 + \pi/2) - q(\theta_0 + 3\pi/2) \approx -\frac{4I}{\pi r^3} \sin \Delta\theta (\langle x^2 \rangle - \langle z^2 \rangle), \tag{C.11}$$

where $\langle x^2 \rangle = \int da \int d\theta_a \rho(a, \theta_a) a^2 cos\theta_a$. Therefore one gets the information of the moments of the beam, and then the emittance can be deduced from this result.

Due to the circuit connection, the real signal from the BPM is the combination of the original and the retarded reflection signal, which makes the data processing complicated. Refer to [37] for details.

Bibliography

[1] Herbert Goldstein, Classical Mechanics, Addison-Wesley Press, Inc. Cambridge 42, Mass., p241,1951(QA805 .G6)

[2] M. Bai, et al.,Phys. Rev. E, 56,6002(1997); M. Bai et al., Phys. Rev. lett. 80,4673(1998).

[3] J.Scott,et.al, 'Landau Damping with two-dimensional betatron tune spread', CERN SL-96-71 AP(1996).

[4] I.M.Kapchinskij, V.A.Teplyakov, Prib. Tekh. Eksp., 1970,(4),P19.

[5] R.D.Kohaupt, 'Single Beam Instabilities in DORIS', IEEE Trans. Nucl. Sci., NS-22, pp. 1456-1457, 1975; Y.H.Chin and K.Yokoya, 'Landau Damping of a Multi-Bunch Instability due to Bunch-to Bunch Tune Spread', DESY, Report No. 86-097, August 1986.

[6] S.Sakanaka et al., 'Construction of an RF Quadrupole Magnet for Suppressing Transverse Coupled-Bunch Instabilities', Proc. of Part. Acce. Conf. 1991,p1836,1991.

[7] V.V.Danilov, Phys. Rev. ST Accel. Beams 1, 041301(1998).

[8] T.Endo et al., in Proc. of APAC,Tsukuba, 1998,p.468; K. Sato et al., in Proc. of EPAC, Sotckholm, 1998,p.1330.

[9] T. Uesugi, Phys. Rev. ST Accel. Beams 5, 044201(2002).

[10] L.L.Gol'din,"Investigation of a beam of charged particles by means of pick-up electrodes",Instruments and Experimental Techniques, pp. 780-784, 1966.

[11] R. H. Miller et al., Proc. 12th Int. Conf. On High Energy Accelerators, (Fermilab, 1983), p.602(1983).

[12] Private communication with Andreas Jansson.

[13] S.J. Russell et al (LANL) 'Characterization of Beam Position Montiors for Measurement of Second Moment',Proc. Particle Accelerator Conference, Dallas, TX, 1995.

[14] S.J.Russell, Rev. of Sci. Inst. 70,2,p1362(1999).

[15] F.M. Bieniosek et al.,'Measurement and Reduction of Quadrupole Injection Oscillations in the Ferminlab Antiproton Accumulator', Proc. Particle Accelerator Conference, Dallas, TX, 1995;

[16] A.Jason et al., 'A Non-invasive Single-Bunch Matching and Emittance Monitor for the CERN PS Based on Quadrupole Pick-ups.', PAC'01, Chicago, 2001.

[17] M. Ellison *et al.*, Phys. Rev. E**50**, 4051 (1994).

[18] L.H.Thomas, Phil.Mag. 3,1(1927);

[19] V. Bargmann, L. Michel, and V.L. Telegdi, Phys. Rev. Lett. 2, 435(1959);

[20] F.Z. Khiari, *et al.*, Phys. Rev. **D39** 45 (1989).

[21] S.Y. Lee, *Spin Dynamics and Snakes in Synchrotrons*, (World Scientific Pub. Co., Singapore, 1997)

[22] See, e.g., S. Y. Lee, *p.51,Accelerator Physics*(World Scientific, Singapore,1998).

[23] M. Ellison et al., Phys. Rev. Lett. 70, 591(1993); M. Syphers et al., Phys. Rev. lett. 71, 719(1993); H. Huang et al., Phys. Rev. E48, 4678(1993); Y. Wang et al., Phys. Rev. E49, 1610(1994).

[24] V.Balbekov, 'Tevatron Longitudinal Instability', FNAL internal report, Oct.4, 2002.

[25] Valeri Lebedev,'Tevatron Task Force', P17, AAC, Feb.4-6,2003;

[26] J.D. Fox and P. Corredoura, in the *Proc. European Part. Accel. Conf.*, p. 1079 (Springer-Verlag, Heidelberg, 1992); D. Li et al., Phys. Rev. E**48**, 1638 (1993); D.D. Caussyn et al., in the *Proc. Part. Acc. Conf.*, p. 29 (IEEE, Piscataway, NJ, 1993); D. Li et al., Nucl. Instru. Methods A**364**, 205 (1995).

[27] M. Bai, et al., Phys.Rev.ST Accel.Beams 3,064001(2000).

[28] J.Rossbach, in *Proceedings of XVIII International Linear Accelerator Conference*, LINAC-96, web address: http://linac96.web.cern.ch/Linac96/Proceedings/Tuesday/TU103/Paper.pdf

[29] 2001 Report on the Next Linear Collider, FERMILAB-Conf-01-075-E, LBNL-47935, SLAC-R-571, UCRL-ID-144077.

[30] M.Abo-Bakr, et al., Phys. Rev. Lett. 88, 254801(2002), M.Abo-Bakr, et al., Phys. Rev. Lett. 90, 094801(2003).

[31] K.M.Fung, et al., Phys.Rev.ST Accel.Beams 3,100101(2000).

[32] W. Guo, S.Y. Lee, Phys. Rev. E 65, 066505(2002).

[33] S.Y.Lee, Accelerator Physics,*World Scientific*, p422.

[34] A. Hofmann and S. Myers, in *Proceedings of the 11th International Conference on High Energy Accelerators*, 1980.

[35] M. Georgsson, A. Andersson, and M. Eriksson, Nucl. Ins. Meth. A 416,465(1998); J. M. Byrd, S. De Santis, M. Georgsson, G. Stover, J. D. Fox, and D. Teytelman, Nucl. Ins. Meth. A 455,271(2000); M. Georgsson, D. Kramer,W. Anders, and J. M. Byrd, Nucl. Ins. Meth. A 469,373(2001);.

[36] J. Le Duff, in *Proceedings of the CERN Accelerator School, Second Advanced Accelerator Physics Course*, Berlin, 1987, Edited by S. turner(CERN, Geneva, 1989); CERN Report 89-01, p119.

[37] M.Wendt et. al,'BPM Read-out Electornics Based on the Broadband AM/PM Nomalization Scheme', DIPAC 2001, ESRF, Grenoble.

Curriculum Vitae

Weiming Guo

IUCF, 2401 Milo B. Sampson Lane
Bloomington, IN 47405
Tel: 812-855-5190(Office)
Email: *weguo@indiana.edu*
WWW: *http://php.indiana.edu/~weguo/*

Education

Degree	Major	Institution
Ph.D. (8/03)	Accelerator Physics	Indiana University, Bloomington
M. S. (6/96)	Accelerator Physics	Institute of Modern Physics, China
B. S. (6/93)	Physics	Nankai University, China

Professional Experience

US Particle Accelerator School, Santa Barbara, CA (Teaching Assistant, 6/03)

Indiana University Cyclotron Facility(Research Associate, 8/99 - present)

- **Dissertation:** Quadrupole Mode perturbation in Storage Rings.

Institute of High Energy Physics, China(Research Assistant, 7/96 - 8/99)

- **Project:** Linac Design for Proton Therapy.

Institute of Modern Physics, China(Research Associate, 7/93 - 7/96)

- **Thesis:** Current Calculation of an Isochronous Cyclotron.

US Particle Accelerator School

USPAS 2003 at Baton Rouge, Fourth Generation Light Sources and FEL

Joint Accelerator School 2003 at Long Beach,
Linac issues, Coherent Synchrotron Radiation

USPAS 2002 at Yale University, Computational electromagnetism

USPAS 2002 at Long Beach, Plasma Physics

USPAS 2001 at University of Colorado,
1. RF and Microwave Techniques for Accelerators,
2. Beam Control and Manipulation.

USPAS 2001 at Rice University, Lie Algebra in Accelerator Physics

USPAS 2000 at Stony Brook, Accelerator Physics

Publication List

1. Yu Qingchang and Weiming Guo, "The Focusing Properties of an Injector RFQ" High Energy Physics and Nuclear Physics(in Chinese), vol.23(3)1999.

2. Weiming Guo and Yu Qingchang, "The Design Study of a 714MHz RFQ as Injector of a Proton Therapy Linac", High Energy Physics and Nuclear Physics(in Chinese), vol.24(3)2000.

3. Weiming Guo and S.Y.Lee, "The Quadrupole Mode Transfer Function and the Nonlinear Mathieu Instability", Phys. Rev. E 65, 066505(2002).

4. Weiming Guo and S.Y.Lee, "Bunch Compression in Electron Storage Rings", to be submitted.